The interaction of solids with intense, time-dependent electromagnetic fields produces rich nonequilibrium phenomena on femtosecond and sub-cycle time scales. This thesis focuses on two spectroscopic probes: high-harmonic generation and time- and angle-resolved photoemission spectroscopy. For the latter, a robust interference effect between inter- and intraband contributions is observed. An analytical explanation supports a systematic numerical study of this interference process beyond standard semiclassical approaches. Recent experiments have studied the time-resolved buildup of Floquet replicas in the surface states of Bi_2Se_3, showing sidebands even with few-cycle pulses. This replica formation is explained semi-analytically and numerically using the instantaneous Floquet formalism. This thesis examines both effects — interference in high-harmonic generation and Floquet sideband formation — through the lens of adiabatic dynamics and nonadiabatic transitions.

Universität Regensburg
UNIVERSITÄTSBIBLIOTHEK

ISBN 978-3-88246-549-5

Coherent suppression of high harmonics and Floquet-Bloch sidebands in lightwave-driven Dirac systems

Wolfgang Hogger

Wolfgang Hogger

Coherent suppression of high harmonics and Floquet-Bloch sidebands in lightwave-driven Dirac systems

UR Publishing Services

Coherent suppression of high harmonics and Floquet-Bloch sidebands in lightwave-driven Dirac systems



Dissertation zur Erlangung des Doktorgrades der Naturwissenschaften (Dr. rer. nat.) der Fakultät für Physik

der Universität Regensburg

vorgelegt von

Wolfgang Hogger aus

Freilassing

im Jahr 2025

Erstgutachter (Betreuer): Apl. Prof. Dr. Juan-Diego Urbina
Zweitgutachter: Apl. Prof. Dr. Andrea Donarini

Tag der Prüfung: 15. April 2026

Bibliografische Information der Deutschen Nationalbibliothek

Die Deutsche Nationalbibliothek verzeichnet diese Publikation in der Deutschen Nationalbibliografie. Detaillierte bibliografische Daten sind im Internet unter http://dnb.dnb.de abrufbar.

ISBN (Print): 978-3-88246-549-5
ISBN (PDF): 978-3-88246-550-1

DOI: 10.5283/epub.79669
Link zur Online-Version: https://epub.uni-regensburg.de/79669

Satz und Layout: Wolfgang Hogger
Titelbild: Wolfgang Hogger
Umschlaggestaltung: Peter Brünsteiner
Herstellung: Universitätsbibliothek Regensburg

Erscheinungsort: Regensburg, 2026
Druck und Bindung: Digital Print Group o. Schimek GmbH, Nürnberg



Dieses Werk ist unter der Creative Commons-Lizenz Namensnennung 4.0 International (CC BY 4.0) veröffentlicht: http://creativecommons.org/licenses/by/4.0/ Ausgenommen sind Abbildungen und alle gesondert gekennzeichneten Inhalte, die eigenen Lizenzbedingungen unterliegen können.

Was sich überhaupt sagen lässt, lässt sich klar sagen; und wovon man nicht reden kann, darüber muss man schweigen.

– Ludwig Josef Johann Wittgenstein [1]

Abstract

The interaction of solids with intense, time-dependent electromagnetic fields gives rise to rich nonequilibrium phenomena on femtosecond and sub-cycle time scales. Understanding how electronic states evolve under such driving, and how this evolution is encoded in experimentally accessible observables, is a central challenge in light-driven condensed-matter physics. This thesis investigates how strong laser fields drive solids into transient nonequilibrium states and how these states manifest in complementary spectroscopic probes, namely high-harmonic generation (HHG) and time- and angle-resolved photoemission spectroscopy (trARPES).

The first part focuses on HHG from driven two-band systems. In materials with small or vanishing band gaps, strong interference between interband and intraband contributions plays a decisive role in HHG and limits the applicability of conventional semi-classical models. In this small-gap regime, a robust interference phenomenon, termed *coherent suppression*, is identified in the HHG spectra of light-driven massive Dirac systems. An analytical description supported by numerical simulations shows that destructive interference between current contributions leads to a pronounced suppression of the total harmonic yield. The effect is shown to be generic, robust against changes in band dispersion, and lifted by dephasing, resulting in characteristic re-entrant harmonics.

The second part addresses the time-resolved formation of dressed electronic states in driven solids. Using an extension of Floquet theory based on the instantaneous Floquet t–t' formalism, the dynamical build-up of Floquet replicas during finite laser pulses is analyzed for a realistic model of Bi_2Se_3. The evolution of replica occupations is shown to be governed by adiabatic dressing and nonadiabatic Landau–Zener transitions, yielding a semi-analytical description in excellent agreement with numerical calculations.

List of publications

1. Wolfgang Hogger, Alexander Riedel, Debadrito Roy, Angelika Knothe, Cosimo Gorini, Juan-Diego Urbina, and Klaus Richter. "Coherent suppression and dephasing-induced reentrance of high harmonics in gapped Dirac materials." In: *Phys. Rev. B* 113.4 (Jan. 2026)

2. Yuriko Baba, Vanessa Junk, Wolfgang Hogger, Francisco Domínguez-Adame, Rafael A Molina, and Klaus Richter. "Radiation-induced dynamical formation of Floquet-Bloch bands in Dirac Hamiltonians." In: *New J. Phys.* 27.4 (Apr. 2025)

List of co-mentored research projects

1. **Mario Ebner**, "Carrier dynamics in Dirac systems induced by strong light pulses", Master's thesis (2022)

2. **Alexander Riedel**, "Magnetic field effects on light-driven topological insulator surface states", Master's thesis (2023)

3. **Debadrito Roy**, "Dephasing effects in massive Dirac systems", Research project as part of an internship (2024)

4. **Andreas Bittner**, "Quantum Transport on Curved Surfaces", Master's thesis (2026)

Contents

Contents **ix**

Notation and units **xiii**

1 Introduction **1**

2 Theoretical description of time dynamics in light-driven systems **7**
2.1 Adiabatic and nonadiabatic dynamics 8
2.2 The Semiconductor Bloch equations 15
2.3 The current density and Larmor's formula 18
2.4 Nondimensionalization of SBE 21
2.5 Effective two-band models 23
2.6 The three step model 25
2.7 Floquet theory 32

3 Coherent suppression of high harmonics **39**
3.1 Two theoretical toy models 40
3.2 Coherent suppression and the suppression ratio 45
3.3 Contributions throughout the Brillouin zone 51
3.4 Physical mechanism of coherent suppression 56
3.5 Re-entrant high harmonics 64
3.6 Conclusions and outlook 68

4 Floquet-Bloch sidebands with finite driving pulses **71**
4.1 A model for topological instulator surface states 72
4.2 Floquet sidebands in topological insulators 74
4.3 Adiabaticity in Floquet sidebands 78
4.4 Conclusions and outlook 81

5 Conclusion **83**

Appendix **87**

A Model comparison for ZnO **89**

B A second suppression ratio **93**

C Description of open-source code **95**
C.1 Modular nature 95
C.2 Parallelization 96
C.3 ODE construction 97
C.4 Convergence testing 98

D On numerical noise **99**

Data Availability **101**

Bibliography **103**

Acknowledgments **121**

Changes in the Published Version **125**

List of Figures

1.1 Schematic for coherent suppression 5
1.2 Schematic of Floquet side bands 6

2.1 Schematic of avoided crossing 11
2.2 Transition regimes for a two-level system 14
2.3 Schematic of SBE dynamics 17
2.4 The Lewenstein model illustrated 28
2.5 Driving field for Semiconductor example 29
2.6 Semiconductor emission spectrum 30
2.7 Time-resolved HHG from a Semiconductor 31

3.1 HHG spectrum showing coherent suppression 39
3.2 Time-resolved electric field 41
3.3 Bandstructure of massive Dirac model 43
3.4 Bandstructure of bilayer graphene toy model 44
3.5 Example HHG spectra for massive Dirac model 47
3.6 Suppression ratio of massive Dirac model 48
3.7 Example HHG spectra for bilayer graphene model 50
3.8 HHG spectra for massive Dirac model in 1D 53
3.9 HHG spectra for bilayer graphene model in 1D 54
3.10 Time-resolved HHG from sliced massive Dirac model 56
3.11 Avoided crossing sketch 57
3.12 Comparison of asymptotic expansion to numerics 60
3.13 Comparison of intensity approximation to numerics 63
3.14 Dephasing sweep for massive Dirac model (1D) 65
3.15 Dephasing sweep for massive Dirac model (2D) 66
3.16 Dephasing dependence of individual harmonics 67
3.17 Dephasing sweep for massive Dirac model, long pulse 68

4.1 Band structure of TI model 73
4.2 Instantaneous Floquet expansion for TI 76
4.3 Instantaneous Floquet expansion conduction band only . . . 77
4.4 Adiabatic correction Floquet TI 79
4.5 Diabatic transition Floquet TI 80

A.1 Energy and dipole of ZnO model 90

B.1 Another suppression ratio for the massive Dirac model . . . 93

C.1 Structure of the simulation object. 96
C.2 Computational flow of Damysos.jl 97

D.1 Demonstration of the numerical noise level 99

List of Tables

2.1 Exemplary values for re-scaling 22

4.1 Numerical parameters for BiSe model 72

A.1 ZnO model coefficients 91

Notation and units

We use Hartree atomic units, where $\hbar = e = 4\pi\epsilon_0 = m_e = 1$ a.u., for all equations containing physical quantities. Sometimes we give values in the SI system for easier comparison to experiment. Many formulas also contain dimensionless quantities, which are defined in the first chapter. The next list describes several symbols that will be later used within the body of the document, both dimensionless and unitful.

$\hat{\mathscr{H}}$	Hamilton operator
$\hat{\varrho}$	Density matrix
Ω	Angular frequency
$\varepsilon_n(\boldsymbol{k})$	Band dispersion for band n
$\boldsymbol{A}(t)$	Vector potential
$\boldsymbol{E}(t)$	Electric field
$\boldsymbol{J}$	Current density
$\boldsymbol{k}$	Crystal momentum (Bloch wave vector)
l_c	Characteristic length scale
T_2	Dephasing time
t_c	Characteristic time scale
$\epsilon_n(\boldsymbol{\kappa})$	Band dispersion for band n (dimensionless)
$\hat{H}$	Hamilton operator (dimensionless)
ω	Angular frequency (dimensionless)
τ	Time (dimensionless)
τ_2	Dephasing time (dimensionless)
$\boldsymbol{a}(\tau)$	Vector potential (dimensionless)
$\boldsymbol{F}(\tau)$	Electric field (dimensionless)
$\boldsymbol{j}$	Current density (dimensionless)
$\boldsymbol{\kappa}$	Crystal momentum (dimensionless)

1 Introduction

Attosecond physics focuses on the observation and control of electronic motion on its natural time scale [4]. The emergence of attosecond science was tightly linked to advances in ultrafast laser technology: femtosecond lasers made it possible to coherently drive matter on optical-cycle time scales, while strong-field nonlinear optics enabled the generation of radiation far beyond the photon energies of the driving field.

A major milestone in this development was recognized by the 2023 Nobel Prize in Physics, awarded for experimental methods enabling the generation of attosecond pulses of light and their application to the study of electron dynamics in matter [5]. Central to these methods is high-harmonic generation (HHG), which remains one of the primary tabletop sources of coherent extreme-ultraviolet (XUV) and soft-x-ray radiation with attosecond temporal structure. Over the past two decades, HHG has evolved from a nonlinear optical phenomenon into a versatile tool for ultrafast spectroscopy and a key pillar of modern attosecond science [6, 7].

The first experimental observation of HHG with infrared photons exhibited a characteristic structure: an initial rapid decay, followed by a broad *plateau* of nearly constant intensity and a sharp cutoff [8]. Although not the first demonstration of HHG, it was the first to clearly reveal the plateau structure. The existence of this characteristic structure is crucial for attosecond science, as it provides the bandwidth required to synthesize ultrashort light bursts when the harmonics are coherently superposed; accordingly, several proposals soon followed [9–11].

The first theoretical explanation of the HHG process relied on numerical solutions of the time-dependent Schrödinger equation and also discussed phase matching necessary to create short light bursts [12]. Soon thereafter, the classical three-step model was proposed [13], providing a beautiful and intuitive explanation of the mechanism behind the HHG plateau: an electron is first released by tunnel ionization near a maximum of the electric field, subsequently accelerated in the continuum by the oscillating laser field, and finally driven back to the parent ion, where recombination leads to the emission of a high-energy photon. Although simplified, this picture explains key features of HHG, including the plateau structure, the scaling of the cutoff with laser intensity aw well as wavelength, and the intrinsic sub-cycle timing of the emission process. A semi-classical

version of the three-step model [14] further solidified the picture and provided quantitatively robust results. Importantly, both variants showed that high-harmonic emission occurs in bursts localized within a fraction of an optical cycle, resulting in a train of attosecond pulses for multi-cycle driving fields.

For many applications, isolated attosecond pulses are required instead of pulse trains. This is achieved by restricting efficient harmonic emission to a single half-cycle of the driving field, using few-cycle pulses with stabilized carrier-envelope phase and various temporal gating techniques [15, 16]. The generation of isolated attosecond pulses is inseparably linked to attosecond metrology. Techniques such as attosecond streaking and interferometric methods based on two-photon transitions allow the reconstruction of spectral phases and emission times, thereby providing calibrated access to both the attosecond light field and ultrafast photoemission dynamics [17, 18].

While early attosecond experiments were primarily focused on gas-phase systems, the scope of HHG has expanded significantly in recent years. In parallel, high-harmonic generation in solids has emerged as a complementary and conceptually distinct platform [19–22]. In crystalline materials, the periodic lattice and multi-band structure fundamentally modify the strong-field response. As a result, solid-state HHG is increasingly viewed not only as a compact source of high-frequency radiation, but also as a form of ultrafast spectroscopy. It has been suggested that HHG from solids can provide time-resolved information on a range of material properties, including electron dynamics [23–25], Berry curvature [26], symmetries [27–30], and correlations [31, 32].

Although these spectroscopic applications of solid-state HHG are appealing due to their all-optical, table-top nature, great care must be taken when comparing theory to experiment. For example, [33] showed that probing topology can be highly nontrivial, and that bulk effects such as the band structure often dominate HHG spectra. Among other signatures, probing the topology of a two-dimensional topological insulator (TI) via helicity flip, as predicted by the driven Haldane model [34–36], turned out to be unreliable when using more refined models based on state-of-the-art time-dependent spin density functional theory.

These challenges stem at least partly from the fact that the microscopic mechanism of HHG in solids is not yet fully understood. Following the success of the three-step model in atomic HHG, a generalization to the

solid-state context has been proposed [37–40]. However, several modifications and variants soon followed to explain discrepancies between numerical simulations and the semi-classical model [41–44]. Materials with a small or vanishing band gap violate core assumptions of the three-step model, which therefore cannot readily reproduce the HHG spectra reported in the literature [45, 46]. Often, emission spectra from such materials feature strong interference between interband and intraband contributions, which is a key aspect studied in the first part of this thesis. Specifically, we investigate the *coherent suppression* of high harmonics taking place in regime inaccessible to the three-step model. We present an alternative analytical approach tailored to this regime that additionally explains the aforementioned suppression.

While high-harmonic generation probes ultrafast electron dynamics through emitted radiation, angle-resolved photoemission spectroscopy (ARPES) provides a more direct view of electronic structure by measuring the energy and crystal momentum of photoemitted electrons. By exploiting energy and momentum conservation in the photoemission process, ARPES enables the reconstruction of electronic band dispersions, Fermi surfaces, and quasiparticle renormalization. As a result ARPES has become a central experimental tool in condensed-matter physics [47].

The modern interpretation of ARPES is commonly formulated in terms of the single-particle spectral function, which provides a unified description of band structure, many-body interactions, and finite quasiparticle lifetimes. Early systematic developments of ARPES, supported by synchrotron radiation sources with tunable photon energy and polarization, established its ability to directly map electronic dispersions in metals, semiconductors, and low-dimensional materials, and to access interaction effects beyond simple band theory [47–50]. These advances laid the foundation for the widespread application of ARPES to correlated and topological materials.

Conventional ARPES is intrinsically a time-averaged probe and therefore insensitive to nonequilibrium dynamics. This limitation was overcome with the development of time- and angle-resolved photoemission spectroscopy (trARPES), enabled by ultrafast laser technology [51]. In a pump-probe configuration, an ultrashort pump pulse drives the system out of equilibrium, while a time-delayed probe pulse photoemits electrons whose energy-momentum distribution reflects the transient electronic state at the moment of photoemission. Early trARPES experiments demonstrated direct access to ultrafast quasiparticle dynamics, relaxation processes, and

transient population changes on femtosecond time scales [52, 53].

The temporal resolution of trARPES has since been pushed into the few-femtosecond regime, allowing the observation of light-induced modifications of band structure during the action of the driving field. A landmark experiment demonstrated that ultrashort pulses enable access to electronic dynamics on time scales comparable to the optical cycle, thereby establishing the basis for attosecond-resolved photoemission and streaking techniques [54]. These developments opened the door to studying coherent light-matter coupling and the real-time evolution of dressed electronic states.

Of particular relevance to light-driven condensed-matter physics is the application of trARPES to periodically or quasi-periodically driven systems. In this context, photoemission experiments have directly revealed the emergence of Floquet-Bloch sidebands and transient replica bands in solids exposed to strong mid-infrared or near-infrared driving fields [55]. Subsequent work clarified the role of coherent photo-dressing and distinguished Floquet-Bloch states from Volkov-type final-state effects, highlighting the importance of finite pulse duration, probe timing, and matrix-element effects in realistic experiments [56].

From a broader perspective, trARPES and HHG provide complementary information about nonequilibrium electronic systems. While trARPES offers momentum-resolved snapshots of transient band structures and electronic populations, HHG probes the coherent current and polarization response integrated over the Brillouin zone. Together, these techniques form a powerful toolbox for investigating light-driven quantum materials, including transient band renormalization, photo-induced gaps, and the dynamical formation of Floquet-like electronic states.

In this context, this thesis investigates how intense, time-dependent electromagnetic fields drive solids into transient nonequilibrium states, and how these states manifest in complementary observables such as high-harmonic emission and time-resolved photoemission. The two main parts of this work address this question from the perspectives of HHG and time-resolved photoemission, respectively.

The remainder of this thesis is organized as follows. Chapter 2 introduces the core concepts and theoretical tools used in this work to describe solid-state materials driven by strong, time-dependent external fields. It presents the overarching concept of adiabatic and nonadiabatic dynamics through the use of a simple two-level system as an example and briefly

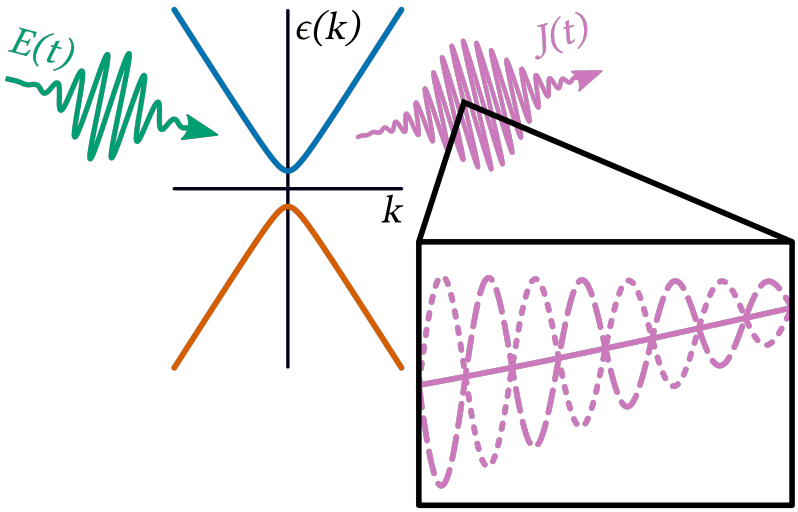


Figure 1.1: Conceptual sketch of coherent suppression (Chapter 2): driving a massive Dirac system with strong electric fields (green) gives rise to an induced current (purple). Fast oscillations of the inter- and intraband contributions (dashed and dotted) cancel via destructive interference to give a smooth total current, visible as suppressed harmonics of high order in the emission spectrum.

introduces the well-established Semiconductor Bloch equations (SBE) as the primary theoretical framework for simulating strong-field physics in solids [57–61]. Additionally, the calculation of HHG spectra via Larmor's formula, a useful general scaling of the SBE, and convenient formulas for two-band systems are presented. The semi-classical three-step model in the solid-state context, along with an example, and Floquet theory with its connection to trARPES are discussed.

Chapter 3 is concerned with a robust interference phenomenon of inter- and intraband contributions that appears in the HHG spectra of light-driven massive Dirac systems; we dubbed it "coherent suppression" in our recent publication [2]. This effect is illustrated conceptually in Figure 1.1: upon driving the solid-state system, an induced current is generated due to the out-of-equilibrium state. The inter- and intraband parts of this current feature fast oscillations that cancel each other, resulting in a much smoother total current, which is reflected in a suppressed total HHG intensity relative to the inter- and intraband spectra. While previous studies have reported the effect in massive Dirac systems [45, 46], we provide the first explanation backed by an analytical treatment as well as extensive numerical exploration of parameter space. Moreover, we use a model for bilayer graphene (BLG) to show that coherent suppression is robust with respect to band-dispersion shape and that including dephasing lifts the suppression. The resulting "re-entrant" harmonics have a characteristic

scaling with dephasing time, which may allow experimental distinction from semi-classically generated harmonics.

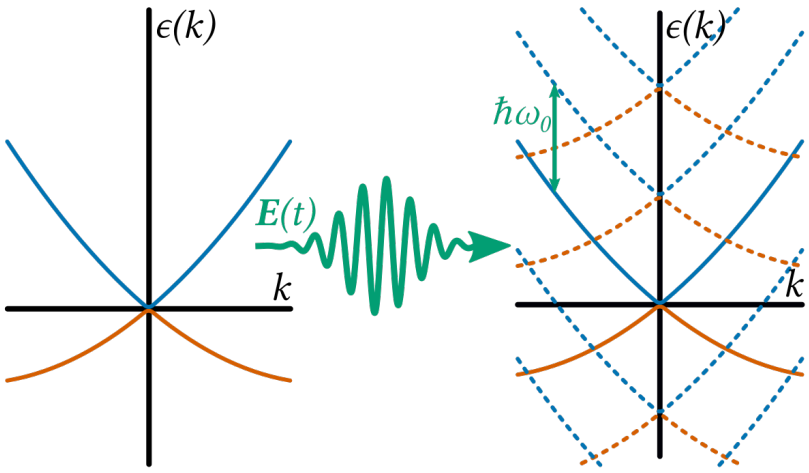


Figure 1.2: Sketch of the transient build-up of Floquet sidebands: a prototypical TI (Bi_2Se_3) is driven by a strong, few-cycle THz laser pulse. The original dispersion (left) is superseded by a Floquet quasi-energy spectrum of replicas shifted by integer multiples of the driving photon energy.

In Chapter 4 we expand upon several aspects of our recent collaboration, published in [3]. This work is motivated by recent experiments [56, 62] employing trARPES to observe the dynamical build-up of Floquet replicas in a TI driven by short laser pulses, as sketched in Figure 1.2. It uses an extension of Floquet theory—the t–t' method, or instantaneous Floquet formalism—for nonperiodic systems to understand how the replicas evolve in time. We extend [3] by employing a realistic initial state, reflecting a Fermi level above the Dirac point in Bi_2Se_3. Furthermore, we demonstrate how the t–t' method allows a description of replica occupations in terms of adiabatic corrections and Landau-Zener transitions, yielding a semi-analytical treatment with excellent quantitative agreement.

Theoretical description of time dynamics in light-driven systems

2

In this chapter, we lay the foundation for the remainder of the thesis by introducing the theoretical methods used to simulate solids driven by coherent electromagnetic radiation. We first introduce the concept of adiabaticity, which plays a central and unifying role throughout this work. We then discuss the semiconductor Bloch equations (SBE), which describe the time evolution of the density matrix in the Bloch basis under the action of a classical electromagnetic field as a system of coupled differential equations. Following pioneering work in the 1980s [57, 58], the SBE have become standard textbook material [59–61], and they continue to form the basis of many recent studies [34, 37, 39, 41, 42, 45, 63–69].

Section 2.1 provides a brief review of adiabatic and nonadiabatic dynamics in the context of light-driven systems.

In Section 2.2, we derive the specific form of the SBE used throughout this work. More general and detailed derivations can be found in recent literature [45, 70, 71] as well as in the textbooks cited above.

Section 2.3 introduces the expressions for the central observables considered in this thesis: the induced current density and the corresponding emission intensity obtained from Larmor's formula. In addition, we present the decomposition of the current into interband and intraband contributions, which plays a key role in Chapter 3.

2.1 Adiabatic and nonadiabatic dynamics 8
2.2 The Semiconductor Bloch equations 15
2.3 The current density and Larmor's formula 18
2.4 Nondimensionalization of SBE . . . 21
2.5 Effective two-band models 23
2.6 The three step model 25
2.7 Floquet theory . . 32

In Section 2.4, we discuss the nondimensionalization of the SBE through the introduction of characteristic length and time scales. Besides simplifying numerical implementations, this procedure is used in Chapter 3 to identify dimensionless parameters that characterize the dynamics of specific models.

In Section 2.5, we derive analytical expressions for general two-band models, which are useful both for improving computational efficiency and for the analytical considerations carried out in Chapter 3.

Section 2.6 discusses one of the most widely used approximations for high-harmonic generation in solids and atoms—the three-step model (also referred to as the Lewenstein or recollision model; see [14, 37, 39, 41–43, 71, 72]). This model is important for the discussion in Chapter 3.

Finally, Section 2.7 introduces Floquet theory [73, 74] and its extension to nonperiodic driving in the form of the instantaneous Floquet formalism [75–80]. This approach is employed in Chapter 4 to analyze Floquet sidebands in topological insulator surface states.

2.1 Adiabatic and nonadiabatic dynamics

Adiabaticity is a simple yet fundamental concept in natural sciences, where a system supports two (or more) sets of variables operating on different time scales, i.e. one set changes much more slowly than the other one. One of the most famous incarnations is the *Born-Oppenheimer approximation* [81, 82], which treats the positions of nuclei as (parametrically) fixed when calculating electronic wave functions. More formally, the adiabatic theorem can be stated as follows: consider a system with its Hamiltonian depending on a set of parameters $\boldsymbol{R}(t) = (R_1(t), R_2(t), \dots)$. The *instantaneous eigenstates* of this Hamilton operator,

$$\hat{\mathscr{H}}(\boldsymbol{R})\,|n(\boldsymbol{R})\rangle = e_n(\boldsymbol{R})\,|n(\boldsymbol{R})\rangle \ , \tag{2.1}$$

form a basis of the system's Hilbert space at each time t. Therefore we can use a superposition of these states,

$$|\psi(t)\rangle = \sum_n c_n(t) \mathrm{e}^{\mathrm{i}\Phi_n(t,t_0)}\,|n(\boldsymbol{R}(t))\rangle \equiv \sum_n c_n(t) \mathrm{e}^{\mathrm{i}\Phi_n(t,t_0)}\,|n(t)\rangle \ , \tag{2.2}$$

including the *dynamical phase*,

$$\Phi_n(t,t_0) = -\int_{t_0}^{t} e_n(s)\,\mathrm{d}s \ , \tag{2.3}$$

as Ansatz for the time-dependent Schrödinger equation (TDSE),

$$\mathrm{i}\frac{\mathrm{d}}{\mathrm{d}t}\,|\psi(t)\rangle = \hat{\mathscr{H}}(\boldsymbol{R}(t))\,|\psi(t)\rangle \ . \tag{2.4}$$

The TDSE is then fully equivalent to a set of coupled differential equations,

$$\mathrm{i}\frac{\mathrm{d}c_n}{\mathrm{d}t} = -\sum_m c_m(t)\,\frac{\mathrm{d}\boldsymbol{R}}{\mathrm{d}t}\cdot\langle n(\boldsymbol{R})|\,\mathrm{i}\frac{\partial}{\partial\boldsymbol{R}}\,|m(\boldsymbol{R})\rangle\,\exp\!\left(-\mathrm{i}\int_{t_0}^{t}\mathrm{d}s\,[e_m(s)-e_n(s)]\right). \tag{2.5}$$

Given an initial state of the system,

$$|\psi(t_0)\rangle = \sum_n c_n(t_0)\,|n(t_0)\rangle \ , \tag{2.6}$$

the *adiabatic theorem of quantum mechanics* [82, 83] states that for slowly changing Hamiltonians $\hat{\mathscr{H}}(\boldsymbol{R}(t))$ the system evolves according to

$$|\psi(t)\rangle \approx \sum_n c_n(t)\,|n(t)\rangle = \sum_n c_n(t_0)\mathrm{e}^{\mathrm{i}\Phi_n(t,t_0)+\mathrm{i}\Theta_n(t,t_0)}\,|n(t)\rangle \tag{2.7}$$

with the geometric (Berry) phase [84],

$$\Theta_n(t,t_0) = \int_{t_0}^{t}\langle n(s)|\,\mathrm{i}\frac{\mathrm{d}}{\mathrm{d}s}\,|n(s)\rangle\,\mathrm{d}s = \int_{\boldsymbol{R}(t)}^{\boldsymbol{R}(t_0)}\langle n(\boldsymbol{R})|\,\mathrm{i}\frac{\partial}{\partial\boldsymbol{R}}\,|n(\boldsymbol{R})\rangle\cdot\mathrm{d}\boldsymbol{R} \ . \tag{2.8}$$

It is well-known, that unless $\boldsymbol{R}$ forms a closed loop in parameter space it can be gauged out by a transformation of the form $|n(\boldsymbol{R})\rangle \to \mathrm{e}^{\mathrm{i}\alpha(\boldsymbol{R})}\,|n(\boldsymbol{R})\rangle$ and does not influence observables. The Berry phase, the Berry connection,

$$\mathscr{A}_\mu^{(n)}(\boldsymbol{R}) = \langle n(\boldsymbol{R})|\,\mathrm{i}\frac{\partial}{\partial R_\mu}\,|n(\boldsymbol{R})\rangle \ , \tag{2.9}$$

and the Berry curvature,

$$\Omega_{\mu\nu}^{(n)}(\boldsymbol{R}) = \frac{\partial}{\partial R_\mu}\mathscr{A}_\nu^{(n)}(\boldsymbol{R}) - \frac{\partial}{\partial R_\nu}\mathscr{A}_\mu^{(n)}(\boldsymbol{R}) \ , \tag{2.10}$$

are related to the Chern theorem and have arguably sparked a new field in condensed matter physics honored in 2016's Nobel prize [85]. Additionally, the Berry phase concept was successfully applied to explain the intrinsic anomalous Hall effect (see [86–89]) and it was instrumental in developing the modern theory of polarization [89–91]. However, in this thesis we deal exclusively with situations where the geometric phase can be ignored.

A useful extension to the adiabatic theorem is *adiabatic perturbation theory*. We restrict the initial state of the system to an instantaneous eigenstate, $|\psi(t_0)\rangle = |m(t_0)\rangle$, to simplify notation. Furthermore, we assume that a small dimensionless constant λ can be found such that a scaled TDSE,

$$\mathrm{i}\lambda\frac{\mathrm{d}}{\mathrm{d}\tau}|\psi(\tau t_c)\rangle = \hat{H}(\tau t_c)\,|\psi(\tau t_c)\rangle \ , \tag{2.11}$$

is equivalent to Equation 2.4 with some time scale t_c. Finding such a λ means identifying a slow time scale and can sometimes require additional approximations or be outright impossible. In Section 2.4 we give more details on how to find such a re-scaling of certain differential equations using the example of the SBE. Adiabatic perturbation theory for Equation 2.5 then amounts to seeking an asymptotic* series [89, 95],

$$c_n(t) \sim c_n^{(0)}(t) + \lambda c_n^{(1)}(t) + \cdots \ , \tag{2.12}$$

which corresponds with the adiabatic theorem at leading order, i.e. it is

$$c_n^{(0)}(t) = \delta_{mn} \ . \tag{2.13}$$

The first correction in λ reduces to an integral,

$$\begin{aligned} c_m^{(1)}(t) &\overset{m\neq n}{=} \int_{t_0}^{t} \mathrm{d}s\,\langle n(s)|\,\mathrm{i}\frac{\mathrm{d}}{\mathrm{d}s}\,|n(s)\rangle \exp\!\left(-\mathrm{i}\int_{t_0}^{t}\mathrm{d}s\,[e_m(s)-e_n(s)]\right) \\ &\approx \frac{\langle n(t)|\,\mathrm{i}\frac{\mathrm{d}}{\mathrm{d}t}\,|n(t)\rangle}{e_m(t)-e_n(t)} \exp\!\left(-\mathrm{i}\int_{t_0}^{t}\mathrm{d}s\,[e_m(s)-e_n(s)]\right), \end{aligned} \tag{2.14}$$

which is approximated by partial integration† in the second line. The contribution shown in Equation 2.14 is precisely what leads to the famous *anomalous velocity* responsible for the intrinsic anomalous Hall effect, see [86, 87, 89].

* For introduction into asymptotic analysis as well as definitions, see e.g. [92–94].

† Exploiting Equation 2.11 allows the standard asymptotic technique of partial integration, see [96]. Alternatively, one assumes the exponential to be oscillating "fast enough".

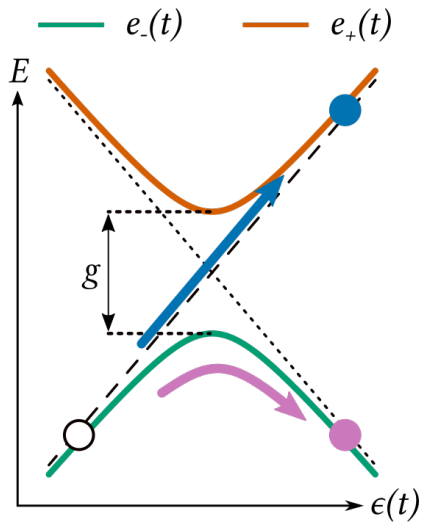


Figure 2.1: Schematic of the energies and qualitative dynamics in a driven two-level system like the one in Equation 2.15. Upper (orange line) and lower (green line) instantaneous eigenergies $e_\pm$ given by Equation 2.16 are shown as a function of the driving $\epsilon(t)$. The dashed and dotted lines show the diabatic energies $\pm\epsilon(t)$. Blue (purple) arrow depicts the diabatic (adiabatic) transition as the state is driven through the avoided crossing.

Next, we consider a simple example to review some basic concepts useful for the rest of this thesis: a two-level system with the Hamiltonian,

$$\hat{\mathscr{H}}_{\mathrm{TL}}(t) = \frac{1}{2}[\epsilon(t)\hat{\sigma}_z + g\,\hat{\sigma}_x]\,, \quad \epsilon(t) = \epsilon_0 \cos(2\pi t/T_0)\,, \tag{2.15}$$

with e driving period T_0 and the energies ϵ_0 and g. The instantaneous eigenstates of Equation 2.15 solve

$$\hat{\mathscr{H}}_{\mathrm{TL}}(t)\,|\varphi(t)_\pm\rangle = e_\pm(t)\,|\varphi(t)_\pm\rangle \quad \text{with} \quad e_\pm(t) = \pm\sqrt{g^2 + \epsilon(t)^2}/2\,. \tag{2.16}$$

The diabatic states, on the other hand, follow the driving energy according to

$$\hat{\mathscr{H}}_{\mathrm{TL}}(t)\,|\psi_{\uparrow\downarrow}(t)\rangle = \pm\epsilon(t)\,|\psi_{\uparrow\downarrow}(t)\rangle \tag{2.17}$$

and are the eigenstates of $\hat{\mathscr{H}}_{\mathrm{TL}}(t)$ for $g = 0$. The TDSE with the Hamiltonian above can be brought into the form of Equation 2.11 by identifying

$$t_c = T_0 \quad \text{and} \quad \lambda = \frac{1}{\epsilon_0 T_0} \tag{2.18}$$

and using $\frac{\partial}{\partial t} = \frac{\partial \tau}{\partial t}\frac{\partial}{\partial \tau} = \frac{\partial}{\partial \tau}/T_0$. For the system defined in Equation 2.15 one can identify $\boldsymbol{R}(t) = (\epsilon(t))$ as the single varying parameter.

A schematic of these energies is shown in Figure 2.1, which illustrates their well-known *avoided crossing* behavior. The diabatic energies $\pm\epsilon(t)$ *cross*, whereas the adiabatic energies $e_{\pm}(t)$ *avoid* each other. Far away from the crossing, diabatic and adiabatic states and their energies approach each other, although $|\psi_{\uparrow\downarrow}\rangle$ switch their energetic order.

In Figure 2.2 we show the time dependence of the instantaneous eigenergies (upper panels) and of the upper eigenstate's occupation $|c_+(t)|^2 = |\langle\varphi_+(t)|\psi(t)\rangle|^2$ (lower panels) for four different parameter sets (T_0, ϵ_0, and g). Initially, the system is prepared in the $|\varphi_-\rangle$ state. In the data shown one can identify qualitatively distinct regimes, as it was discussed e.g. in [97, 98].

Figure 2.2, panel (b) corresponds to the *diabatic regime* (blue arrow in Figure 2.1), i.e. the system follows not the instantaneous eigenstate but the diabatic states $|\psi_{\uparrow\downarrow}\rangle$. Figure 2.2, panel (c) on the other hand the system stays almost exclusively in the instantaneous eigenstate it was initially prepared in with a very small correction approximated very well by the expression given in Equation 2.14 (yellow dashed line). This adiabatic behavior corresponds to the purple arrow in Figure 2.1. Yet another regime is visible in panel (a) of Figure 2.2, where the evolution is approximately adiabatic at all times but during passing the avoided crossings, where abrupt transitions with probability P occur. The yellow dashed lines in panels (a) and (b) of Figure 2.2 mark the transition probability according to the Landau-Zener formula, which is discussed in more detail further below.

Finally, panel (d) of Figure 2.2 shows the Rabi regime where the driving frequency is at or near resonance. Mathematically this regime corresponds to small detuning $\delta\omega = \frac{2\pi}{T_0} - g \ll \omega$ and weak coupling $\epsilon_0 \ll g$. It is amenable to the rotating wave approximation, which yields the Rabi oscillations (yellow dashed lines in panel (d) of Figure 2.2) with frequency $\Omega_R = \sqrt{g^2 + \delta\omega^2}/4$ given by the formula

$$P_R(t) = \frac{g^2}{g^2 + \delta\omega^2} \sin(\Omega_R t)^2 \,. \tag{2.19}$$

Note that Rabi-like oscillations can also occur for stronger driving in the Stückelberg regime under certain conditions, see [99–101].

Next take note of the following fact: surprisingly, for all data shown in panels (a)-(c) of Figure 2.2 the adiabatic parameter is $\lambda = 0.005$, so

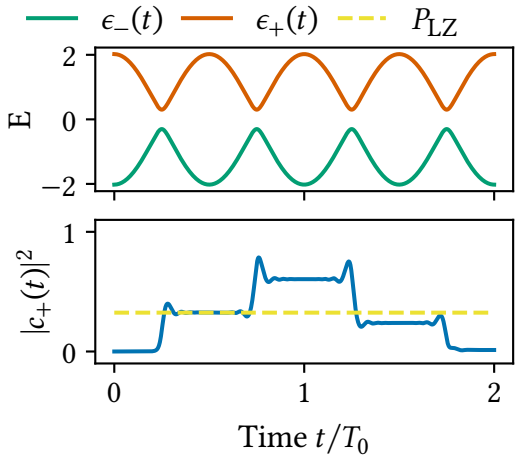
one might expect them all to behave adiabatically, i.e. to qualitatively look like Figure 2.2, panel (c). What went wrong? The solution lies in the denominator of the pre-exponential factor in Equation 2.14, which diverges if two energies coincide and thus makes $c_m^{(1)}$ a bad approximation. In the sense of asymptotics, the approximation is *not uniform* in the other parameters governing the system. One can identify the nonadiabatic nature of the crossing visually in Figure 2.2 by how narrow the crossing is in the upper panels.

The problem of these *nonadiabatic transitions* around points where energies almost touch with respect to some slowly varying parameter appears in many areas of physics and chemistry, see [102]. Probably the most important solution to this problem leads to the Landau-Zener formula [103–106],

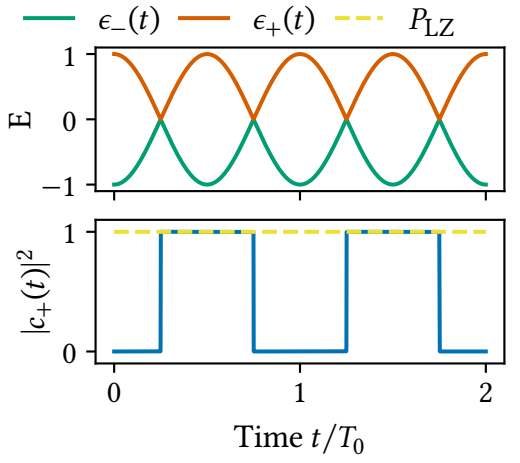
$$P_{LZ} = \mathrm{e}^{-\frac{\Delta^2}{4v}}\,, \tag{2.20}$$

with the band gap Δ and the velocity of change in the Hamiltonian v. For the model in Equation 2.15 $\Delta = g$ and $v = 2\pi\epsilon_0/T_0$. Replacing $\epsilon(t) \to vt$ in Equation 2.15 results in the model originally considered by Landau, which can be solved exactly or approximately with semi-classical or Laplace transform methods. Generically, one can apply the strategy of linearizing any Hamiltonian around the avoided crossing(s) and then patching the aforementioned exact solutions together with adiabatic approximation, which is valid in between transitions. This is often called the "transfer-matrix" approach or the "adiabatic impulse model"; see [101, 107] for reviews of the different solution methods and easy-to-apply general formulas. Hence, the behavior shown in panel (a) of Figure 2.2 is also named "adiabatic impulsive LZS regime"; Stückelberg primarily studied the situation where $P_{LZ} \approx 1/2$ (see [106]).

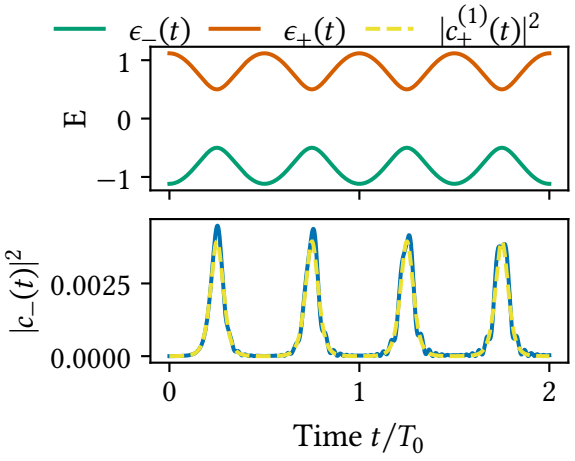
In Chapters 3 and 4 we encounter the concept of avoided crossings and nonadiabatic transitions again and use it to explain the physics underlying HHG as well as Floquet sideband generation.



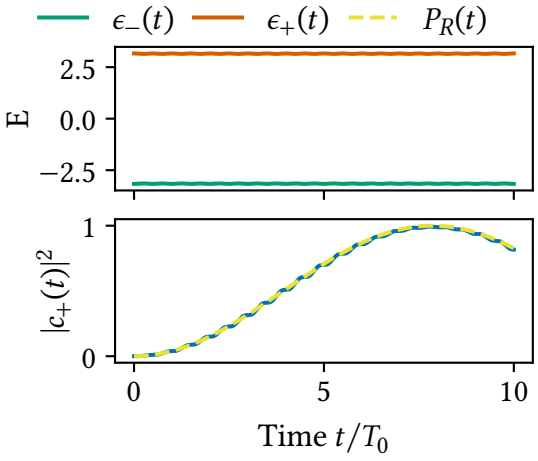
(a) Stückelberg regime: $\epsilon_0 = 4$ a.u., $g = 0.6$ a.u., and $T_0 = 50$ a.u.. Tunneling probability $P_{\mathrm{LZ}} = \mathrm{e}^{-g^2 T_0/4(2\pi)\epsilon_0}$ marked by dashed line for comparison to numerics (solid blue line).



(b) Diabatic regime: $\epsilon_0 = 2$ a.u., $g = 0.001$ a.u., and $T_0 = 100$ a.u.. Tunneling probability $P_{\mathrm{LZ}} = \mathrm{e}^{-g^2 T_0/4(2\pi)\epsilon_0}$ marked by dashed line for comparison to numerics (solid blue line).



(c) Adiabatic regime: $\epsilon_0 = 1$ a.u., $g = 0.6$ a.u., and $T_0 = 100$ a.u.. Dashed line shows how the correction given in Equation 2.14 approaches the numerical result (solid blue line).



(d) Rabi regime: $\epsilon_0 = 0.8$ a.u., $g = 2\pi$ a.u., and $T_0 = 1$ a.u.. Dashed line shows Rabi oscillations given by Equation 2.19 compared to the numerical result (solid blue line).

Figure 2.2: Illustration of different transition regimes from the two-level system given in Equation 2.15. The upper panels of a-d show the time-dependent adiabatic energies $\epsilon_\pm$ (orange and green lines) and lower panels show the upper eigenstate's occupation $|c_+(t)|^2$ (blue line). For all data shown above, the system is initially in the lower energy eigenstate $|\varphi_-\rangle$. The adiatabic parameter is $\lambda = 0.005$ (cf. Equation 2.18) for (a)-(c) and $\lambda = 1.25$ for (d). Panel (a) shows well-separated Landau-Zener transitions take place and occupations between avoided crossings are approximately constant, i.e. adiabatic. In panel (b) the state remains in one diabatic state, which translates to rapid transitions in the adiabatic picture (blue path in Figure 2.1). In the data shown in panel (c) the driving is slow enough such that almost no transitions occur (purple path in (a)), only perturbative contributions are visible. Panel (d) demonstrates Rabi oscillations at resonance $g = 2\pi/T_0$.

2.2 The Semiconductor Bloch equations

In this section we present the Semiconductor Bloch equations [57] (SBE). They can be derived in a variety of different ways. Modern derivations often focus on the treatment of many-body effects via Hartree-Fock [45, 59, 70] or the quantum cluster expansion [61, 108, 109]. Especially clear, thorough introduction and derivation of the SBE can be found in [45, 59, 60, 70]. We work with effective models and at the effective[‡] single particle level only throughout this thesis, therefore a simple approach for this special case is presented here. Consider free Fermions in a periodic lattice described by a Hamiltonian,

$$\hat{\mathscr{H}}_0 = \frac{\hat{\boldsymbol{p}}^2}{2m} + V(\hat{\boldsymbol{r}}) \,, \tag{2.21}$$

with $V(\boldsymbol{r}+\boldsymbol{R}) = V(\boldsymbol{r})$ for any lattice vector $\boldsymbol{R}$. According to Bloch theorem[§] the solutions are of the form $\psi_{n\boldsymbol{k}}(\boldsymbol{r}) = \mathrm{e}^{\mathrm{i}\boldsymbol{k}\boldsymbol{r}} u_{n\boldsymbol{k}}(\boldsymbol{r})$. The lattice periodic parts $u_{n\boldsymbol{k}}(\boldsymbol{r}) = \langle \boldsymbol{r}|n\boldsymbol{k}\rangle$ are themselves solutions of the eigenvalue equation,

$$\hat{h}_0(\boldsymbol{k})\, u_{n\boldsymbol{k}}(\boldsymbol{r}) = \left[\frac{1}{2m}\left(-\mathrm{i}\nabla + \boldsymbol{k}\right)^2 + V(\boldsymbol{r})\right] u_{n\boldsymbol{k}}(\boldsymbol{r}) = \varepsilon_n(\boldsymbol{k})\, u_{n\boldsymbol{k}}(\boldsymbol{r}) \tag{2.22}$$

with boundary conditions $u_{n\boldsymbol{k}}(\boldsymbol{r}) = u_{n\boldsymbol{k}}(\boldsymbol{r}+\boldsymbol{R})$ and $\boldsymbol{k}$ being any wavevector in the first Brillouin zone. The kets $|n\boldsymbol{k}\rangle$ thus denote the periodic parts as elements of L^2 over the unit cell, with inner product $\langle m\boldsymbol{k}|n\boldsymbol{k}\rangle = \int_{\mathrm{u.c.}} \mathrm{d}^3 r\; u^*_{m\boldsymbol{k}}(\boldsymbol{r})\, u_{n\boldsymbol{k}}(\boldsymbol{r}) = \delta_{mn}$. We employ the dipole approximation [59, 61]: the electric field,

$$\boldsymbol{E}(\boldsymbol{r}, t) = \boldsymbol{E}(\boldsymbol{r}_0, t) + \mathcal{O}(|\boldsymbol{r} - \boldsymbol{r}_0|) \approx \boldsymbol{E}(t) \,, \tag{2.23}$$

is expanded in space including only leading order. This expansion is generally valid if the crystal unit cell is much smaller than the electric fields wavelength ($\approx 300\,\mu\mathrm{m}$ at 1 THz). As noted in [59], the spatial dependence does not vanish completely but just varies on a macroscopic length scale, which can be included in the SBE (cf. [65]). The resulting coupled Maxwell-Bloch equations (SBE + Maxwell) can describe how electromagnetic fields propagate through a bulk medium and interact with the induced fields.

[‡] By "effective" single particle approach we refer to the fact that the SBE as used here are the lowest order term in the quantum cluster expansion [61, 108, 109]. As such it contains Pauli blocking, which is often considered a many-body effect.

[§] Any textbook on solid state physics explains these basics of periodic lattices (e.g. [110]).

These phenomena are sometimes called *macroscopic propagation effects*[¶] in the literature [59, 65]. Choosing the velocity gauge[‖] for the field,

$$\boldsymbol{A}(t) = -\int^{t} \boldsymbol{E}(s)\,\mathrm{d}s \ , \tag{2.24}$$

keeps the Hamiltonian,

$$\hat{\mathscr{H}}(t) = \frac{1}{2m}[\hat{\boldsymbol{p}} - \boldsymbol{A}(t)]^2 + V(\hat{\boldsymbol{r}}) \ , \tag{2.25}$$

translation-invariant upon inclusion of the driving field. Note that we use atomic units above and throughout this work unless stated otherwise. A possible basis for representing the equations of motion are the co-moving (or Houston) states [45, 71, 111, 112] $u^H_{n\boldsymbol{k}}(\boldsymbol{r}) = \langle \boldsymbol{r}|n\boldsymbol{k}_t\rangle$, which are the Bloch states evaluated at the shifted (kinetic) crystal momentum $\boldsymbol{k}_t = \boldsymbol{k} - \boldsymbol{A}(t)$. The Houston states are therefore the instantaneous eigenstates of $\hat{h}_0(\boldsymbol{k}_t)$

$$\hat{h}_0(\boldsymbol{k}_t) u^H_{n\boldsymbol{k}}(\boldsymbol{r}) = \varepsilon_n(\boldsymbol{k}_t)\, u^H_{n\boldsymbol{k}}(\boldsymbol{r}) \ . \tag{2.26}$$

In the language of adiabatic evolution introduced in Section 2.1 this momentum represents the set of parameters, $\boldsymbol{R}(t) = \boldsymbol{k}_t$, and the BZ is the parameter space (with the topology of a torus). The time dynamics of the density matrix obeys the Louville-van-Neumann equation $\frac{\mathrm{d}}{\mathrm{d}t}\hat{\varrho} = -\mathrm{i}\big[\hat{\mathscr{H}}(t), \hat{\varrho}(t)\big]$. In the basis of Houston states one finds the equations of motion,

$$[\mathrm{i}\,\partial_t - \varepsilon_{mn}(\boldsymbol{k}_t)]\,\varrho_{mn}(\boldsymbol{k},t) = \boldsymbol{E}(t)\cdot\sum_{r=1}^{N}[\varrho_{mr}(\boldsymbol{k},t)\boldsymbol{D}_{rn}(\boldsymbol{k}_t) - \boldsymbol{D}_{mr}(\boldsymbol{k}_t)\varrho_{rn}(\boldsymbol{k},t)], \tag{2.27}$$

for the density matrix elements $\varrho_{mn}(\boldsymbol{k},t) = \langle m\boldsymbol{k}_t|\,\hat{\varrho}(t)\,|n\boldsymbol{k}_t\rangle$, where we sum over all N bands of the system. Hereby we introduce the band dispersion differences,

$$\varepsilon_{mn}(\boldsymbol{k}) = \varepsilon_m(\boldsymbol{k}) - \varepsilon_n(\boldsymbol{k}) \ , \tag{2.28}$$

and the dipole matrix elements,

$$\boldsymbol{D}_{mn}(\boldsymbol{k}) = \langle m\boldsymbol{k}|\,\hat{\boldsymbol{r}}\,|n\boldsymbol{k}\rangle = \langle m\boldsymbol{k}|\,\mathrm{i}\frac{\partial}{\partial\boldsymbol{k}}\,|n\boldsymbol{k}\rangle \ . \tag{2.29}$$

[¶] Other authors use this term referring to the propagation of the induced fields in the vacuum after leaving the bulk (see [71]).

[‖] Sometimes this is also called Coulomb gauge $\nabla\cdot\boldsymbol{A} = 0$.

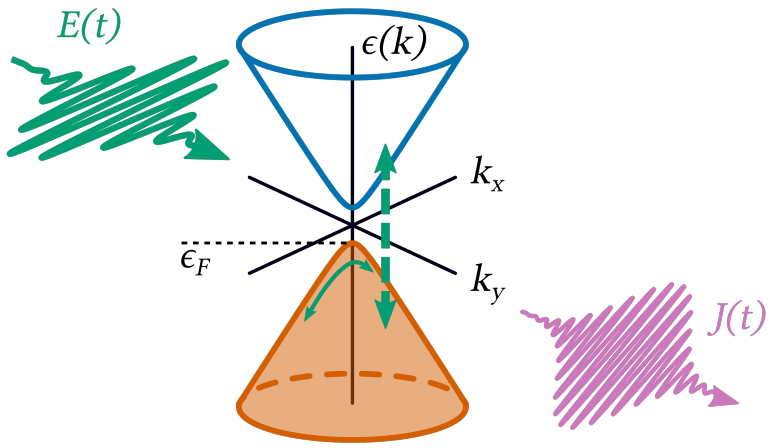


Figure 2.3: A schematic depiction of charge carrier dynamics in the SBE: conduction (blue) and valence (orange) bands are filled up to the Fermi level ε_{F}. The electric field $\boldsymbol{E}(t)$ drives intraband motion (solid green) and interband transitions (dashed green). The resulting non-equilibrium occupations and coherences result in a current $\boldsymbol{J}(t)$ (purple).

For detailed derivations of Equation 2.29, we refer the reader, for example, to Refs. [59, 70, 113]. We briefly recall the physical interpretation of the density-matrix elements ϱ_{mn} in the context of Equation 2.27. The diagonal elements $\varrho_{nn}(\boldsymbol{k}, t)$ represent the occupation probability of charge carriers with crystal momentum $\boldsymbol{k}_t = \boldsymbol{k} - \boldsymbol{A}(t)$ in band n. The off-diagonal elements $\varrho_{mn}(\boldsymbol{k}, t)$ with $m \neq n$ describe coherent superpositions of bands m and n and encode the relative phase between these components; they are therefore referred to as coherences.

Figure 2.3 schematically illustrates the time evolution generated by the SBE. As a consequence of the minimal coupling in Equation 2.25, the kinematic momentum $\boldsymbol{k}_t$ is driven by the external field according to Bloch's acceleration theorem, $\partial_t \boldsymbol{k}_t = -\boldsymbol{E}(t)$. As a result, the $\boldsymbol{k}$ modes evolve within their respective bands, a process commonly referred to as *intraband* motion in the literature [70]. In addition, the electric field couples to the dipole matrix elements $\boldsymbol{D}_{mn}$, thereby mediating transitions between different bands, known as *interband transitions*.

Equation 2.27 is derived for noninteracting Fermions and consequently neglects various many-body effects. It is known that electron-electron or electron-phonon interaction lead to renormalization of band dispersions and dipoles among other higher order correlation effects [59, 61]. We follow previous studies [21, 24, 34, 37, 39, 41, 42, 45, 63, 64, 114–116] by introducing a dephasing mechanism on a phenomenological level in order to be consistent with experimental results and as a generic model

for decoherence. This phenomenological treatment is fairly "agnostic" with respect to the actual mechanism(s) governing the decoherence. For example, such a description can mimic propagation effects [65, 117], but it is also expected to describe other many-body interaction effects [45, 70]. However, the microscopic origin and most relevant channels of dephasing are still under discussion and an active area of research [65, 66, 118–120]. Including dephasing leads to the SBE in the form used throughout this work,

$$\left[\mathrm{i}\,\partial_t + \frac{\mathrm{i}(1-\delta_{mn})}{T_2} - \varepsilon_{mn}(\boldsymbol{k}_t)\right]\varrho_{mn}(\boldsymbol{k},t) = \boldsymbol{E}(t)\cdot\boldsymbol{X}_{mn}(\boldsymbol{k},t)\,,$$
$$\boldsymbol{X}_{mn}(\boldsymbol{k},t) = \boldsymbol{E}(t)\cdot\sum_{r=1}^{N}\left[\varrho_{mr}(\boldsymbol{k},t)\boldsymbol{D}_{rn}(\boldsymbol{k}_t) - \boldsymbol{D}_{mr}(\boldsymbol{k}_t)\varrho_{rn}(\boldsymbol{k},t)\right]\,, \tag{2.30}$$

where T_2 is the characteristic *dephasing time* of the system.

Throughout this work, the initial state of the SBE is given by the ground state of the unperturbed system, i.e. with vanishing external field $\boldsymbol{A} = 0$, $\boldsymbol{E} = 0$. According to Fermi-Dirac statistics, this state is given by

$$\rho^{\mathrm{in}}_{mn}(\boldsymbol{\kappa}) = \frac{\delta_{mn}}{\mathrm{e}^{\beta[\varepsilon_n(\boldsymbol{k})-\varepsilon_{\mathrm{F}}]}+1} \xrightarrow{T\to 0} \begin{cases}\delta_{mn}, & \text{if } \varepsilon_n(\boldsymbol{k}) \le \varepsilon_{\mathrm{F}}\\ 0, & \text{otherwise}\,,\end{cases} \tag{2.31}$$

for Fermi-level ε_{F} and temperature $T = 1/k_{\mathrm{B}}\beta$.[**]

2.3 The current density and Larmor's formula

One of the most important observables in the context of high-harmonic generation (HHG) and transport is the induced current density $\boldsymbol{J}(t)$ of the system. It can be calculated from the solutions of the SBE,

$$\boldsymbol{J}(t) = \sum_{m,n=1}^{N}\int_{BZ(t)} \varrho_{mn}(\boldsymbol{k},t)\boldsymbol{J}_{nm}(\boldsymbol{k}_t)\,\mathrm{d}\boldsymbol{k}\,, \tag{2.32}$$

where we introduced the current matrix elements,

$$\boldsymbol{J}_{mn}(\boldsymbol{k}) = \langle m\boldsymbol{k}|\,\frac{\partial\hat{\mathscr{H}}_0}{\partial\boldsymbol{k}}\,|n\boldsymbol{k}\rangle\,, \tag{2.33}$$

[**] Boltzmann's constant is given by $k_{\mathrm{B}} = 3.166811563\times10^{-6}$ a.u. in hartree atomic units.

in the Bloch basis. The integral is performed over the moving Brioullin zone (BZ),

$$BZ(t) = \left\{ \boldsymbol{k} \,\middle|\, \boldsymbol{k} - \boldsymbol{A}(t) \in BZ \right\}, \tag{2.34}$$

which is a result of the chosen co-moving basis [37, 45, 67, 70]. It is possible to shift the integral such that the current matrix-elements become constant in time. In fact this corresponds to a shift from the co-moving basis with a velocity gauge Hamiltonian to a static Bloch basis with length gauge i.e.

$$\begin{aligned} \boldsymbol{J}(t) &= \sum_{m,n=1}^{N} \int_{BZ} \varrho_{mn}(\boldsymbol{k} + \boldsymbol{A}(t), t) \boldsymbol{J}_{nm}(\boldsymbol{k}) \, \mathrm{d}\boldsymbol{k} \\ &= \sum_{m,n=1}^{N} \int_{BZ} \varrho^{D}_{mn}(\boldsymbol{k}, t) \boldsymbol{J}_{nm}(\boldsymbol{k}) \, \mathrm{d}\boldsymbol{k} \ , \end{aligned} \tag{2.35}$$

which was shown in [45]. Hence, the two basis sets are connected by a time-dependent shift in $\boldsymbol{k}$-space: $\varrho^{D}_{mn}(\boldsymbol{k}, t) = \varrho_{mn}(\boldsymbol{k} + \boldsymbol{A}(t), t)$. There is a different but equivalent definition for the current density via the microscopic polarization; we simply note here that $\frac{\mathrm{d}}{\mathrm{d}t}\boldsymbol{P}(t) = \boldsymbol{J}(t)$ [45, 59, 70].

There exists a natural but ultimately arbitrary decomposition of the current density that arises from the choice of Bloch states as a basis,

$$\boldsymbol{J}(t) = \boldsymbol{J}_{\mathrm{intra}}(t) + \boldsymbol{J}_{\mathrm{inter}}(t) \, , \tag{2.36}$$

which nevertheless admits a simple physical interpretation. The *intraband* current,

$$\boldsymbol{J}_{\mathrm{intra}}(t) = \int_{BZ(t)} \boldsymbol{J}_{\mathrm{intra}}(\boldsymbol{k}, t) \, \mathrm{d}\boldsymbol{k} = \sum_{n=1}^{N} \int_{BZ(t)} \varrho_{nn}(\boldsymbol{k}, t) \boldsymbol{J}_{nn}(\boldsymbol{k}_t) \, \mathrm{d}\boldsymbol{k} \tag{2.37}$$

$$= \sum_{n=1}^{N} \int_{BZ(t)} \varrho_{nn}(\boldsymbol{k}, t) \left. \frac{\partial \varepsilon_n}{\partial \boldsymbol{k}} \right|_{\boldsymbol{k}_t} \mathrm{d}\boldsymbol{k} \ , \tag{2.38}$$

describes the contribution arising from charge carriers moving with the group velocities $\frac{\partial \varepsilon_n}{\partial \boldsymbol{k}}$ of their respective band dispersions.

By contrast, the *interband* current,

$$\boldsymbol{J}_{\text{inter}}(t) = \int_{BZ(t)} \boldsymbol{J}_{\text{inter}}(\boldsymbol{k}, t)\, \mathrm{d}\boldsymbol{k} = \sum_{\substack{m,n=1 \\ m\neq n}}^{N} \int_{BZ(t)} \varrho_{mn}(\boldsymbol{k}, t) \boldsymbol{J}_{nm}(\boldsymbol{k}_t)\, \mathrm{d}\boldsymbol{k} \tag{2.39}$$

$$= \mathrm{i} \sum_{\substack{m,n=1 \\ m\neq n}}^{N} \int_{BZ(t)} \varrho_{mn}(\boldsymbol{k}, t)\, \varepsilon_{nm}(\boldsymbol{k}_t)\, \boldsymbol{d}_{nm}(\boldsymbol{k}_t)\, \mathrm{d}\boldsymbol{k} \ , \tag{2.40}$$

can be interpreted as arising from dipole moments associated with coherent electron–hole superpositions.

A remark regarding this decomposition is in order. The intraband and interband currents are not physical observables individually, as their definition depends on the chosen basis. For example, Ref. [45] shows that the interband current contains anomalous velocity contributions as well as a so-called "dephasing current", while Ref. [71] additionally identifies a "mixture current" originating from a generalized derivative [121]. The relative roles of interband and intraband contributions in high-harmonic generation have therefore been discussed extensively in the literature [21, 37, 39, 41, 42, 45, 46, 63, 71, 122, 123]. We attribute this diversity primarily to the strong dependence of the balance between these contributions on the specific physical system under consideration, including both material properties and driving-field parameters. Their relative magnitude and phase play a central role in Chapter 3 in the context of HHG.

The induced currents introduced in Equation 2.32 resulting from accelerated charge carriers give rise to electromagnetic fields themselves, which is the physical origin of HHG. The spectral intensity of the emitted radiation is calculated via Larmor's formula [45, 124],

$$\mathscr{I}(\Omega) = \frac{\Omega^2}{3c^3} |\boldsymbol{J}(\Omega)|^2 = \frac{1}{3c^3} \left|\dot{\boldsymbol{J}}(\Omega)\right| , \tag{2.41}$$

expressed in terms of the speed of light c in vacuum, the Fourier transform of the current density,

$$\boldsymbol{J}(\Omega) = \frac{1}{\sqrt{2\pi}} \int_{-\infty}^{\infty} \boldsymbol{J}(t) \mathrm{e}^{-\mathrm{i}\Omega t}\, \mathrm{d}t \ , \tag{2.42}$$

and its time derivative,

$$\dot{\boldsymbol{J}}(\Omega) = \frac{1}{\sqrt{2\pi}} \int_{-\infty}^{\infty} \frac{\mathrm{d}\boldsymbol{J}}{\mathrm{d}t} \mathrm{e}^{-\mathrm{i}\Omega t}\, \mathrm{d}t = \mathrm{i}\Omega\, \boldsymbol{J}(\Omega)\,. \tag{2.43}$$

We denote spectral emission intensity polarized along a unit-vector $\boldsymbol{n}$,

$$\mathscr{I}_{\boldsymbol{n}}(\Omega) = \frac{\Omega^2}{3c^3} |\boldsymbol{J}(\Omega) \cdot \boldsymbol{n}|^2\,, \tag{2.44}$$

with $\mathscr{I}_{\parallel}$ ($\mathscr{I}_{\perp}$) for emission parallel (perpendicular) to a linearly-polarized driving field.

2.4 Nondimensionalization of SBE

Instead of working with Equation 2.30, which contains quantities with units, it can be advantageous to "non-dimensionalize" [125] the system of differential equations. On the one hand this allows identification of dimensionless numbers characterizing the system. On the other hand one can often use the freedom of choice for characteristic scales to avoid very large or very small numbers, which are unsuited for numerical computations.

We follow the generic recipe for nondimensionalization: the dependent variables are the density matrix elements ϱ_{mn} and the independent variable is the time t and the wavevector $\boldsymbol{k}$. Therefore we introduce the dimensionless variables,

$$\tau = \frac{t}{t_c}, \quad \boldsymbol{\kappa} = l_c\, \boldsymbol{k}, \quad \rho_{mn}(\boldsymbol{\kappa}, \tau) = \varrho_{mn}(\boldsymbol{k}, t), \tag{2.45}$$

with characteristic time scale t_c and length scale l_c to be determined. Transforming the derivative via $\frac{\partial}{\partial t} = \frac{1}{t_c}\frac{\partial}{\partial \tau}$ leads to a dimensionless form of the SBEs,

$$\begin{aligned} \left[\mathrm{i}\,\partial_\tau + \frac{\mathrm{i}(1-\delta_{mn})}{\tau_2} + \epsilon_{mn}(\boldsymbol{\kappa}_\tau)\right] \rho_{mn}(\boldsymbol{\kappa}, \tau) &= \boldsymbol{F}(\tau) \cdot \boldsymbol{Y}_{mn}(\boldsymbol{\kappa}, \tau)\,, \\ \boldsymbol{Y}(\boldsymbol{\kappa}, \tau) = \boldsymbol{F}(\tau) \cdot \sum_{r=1}^{N} &[\rho_{mr}(\boldsymbol{\kappa}, \tau)\boldsymbol{d}_{rn}(\boldsymbol{\kappa}_\tau) - \boldsymbol{d}_{mr}(\boldsymbol{\kappa}_\tau)\rho_{rn}(\boldsymbol{\kappa}, \tau)]\,, \end{aligned} \tag{2.46}$$

where we introduced[††]

$$\tau_2 = T_2/t_c, \quad \epsilon_{mn}(\boldsymbol{\kappa}) = t_c\,\varepsilon_{mn}(\boldsymbol{k}), \quad \boldsymbol{d}_{mn}(\boldsymbol{\kappa}) = \boldsymbol{D}_{mn}(\boldsymbol{k})/l_c \tag{2.47}$$

$$\boldsymbol{F}(\tau) = l_c\,t_c\,\boldsymbol{E}(t) \quad \text{and} \quad \boldsymbol{a}(\tau) = l_c\,\boldsymbol{A}(t)\,. \tag{2.48}$$

Inspecting Section 2.4 and recalling the Liouville-van-Neumann equations allows identifying a scaled Hamiltonian,

$$\hat{H}(\tau) = \hat{\mathscr{H}}(\tau t_c)/t_c\,, \tag{2.49}$$

which can also be seen from applying the same re-scaling procedure to the TDSE. In order to identify dimensionless numbers characterizing a system, one has to specify more details about the system like the Hamiltonian or driving field. In Table 2.1 we show an exemplary set of quantities in atomic units, SI units, and as dimensionless quantities according to the scaling defined above.

Table 2.1: Various physical quantities and their values in atomic units, SI units, and of their corresponding dimensionless partners according to the scaling introduced in Equations 2.45 and 2.47. Here we set $t_c = 1$ fs and $l_c = 1$ Å.

Quantity	Atomic units	SI	Scaled quantity	Scaled value
ε_{cv}	0.024	0.66 eV	ϵ_{cv}	1.0
$\lvert\boldsymbol{E}\rvert$	0.013	66 MV cm^{-1}	$\lvert\boldsymbol{F}\rvert$	1.0
$\lvert\boldsymbol{D}_{cv}\rvert$	0.53	4.5×10^{-21} C nm	$\lvert\boldsymbol{d}_{cv}\rvert$	1.0
$\lvert\boldsymbol{k}\rvert$	0.53	1.0 Å^{-1}	$\lvert\boldsymbol{\kappa}\rvert$	1.0
$\Omega/2\pi$	0.0024	100 THz	$\omega/2\pi$	0.1

The nondimensionalization can also be applied to the observables of a system, such that we find the dimensionless current density,

$$\boldsymbol{j}(\tau) = \frac{t_c}{l_c^{1-d}}\boldsymbol{J}(\tau t_c) = \int_{BZ(\tau)} \rho_{mn}(\boldsymbol{\kappa},\tau)\,\boldsymbol{j}_{nm}(\boldsymbol{\kappa}_\tau)\,\mathrm{d}\boldsymbol{\kappa} \tag{2.50}$$

with the current matrix elements $\boldsymbol{j}_{mn}(\boldsymbol{\kappa}) = \langle m\boldsymbol{\kappa}|\,\frac{\partial\hat{H}}{\partial\boldsymbol{\kappa}}\,|n\boldsymbol{\kappa}\rangle$. Similarly, we introduce its dimensionless Fourier transform,

$$\boldsymbol{j}(\omega) = \frac{t_c^2}{l_c^{1-d}}\boldsymbol{J}(\omega/t_c) = \mathscr{F}[\boldsymbol{j}(\tau)](\omega) = \frac{1}{\sqrt{2\pi}}\int_{-\infty}^{\infty}\boldsymbol{j}(\tau)\mathrm{e}^{-\mathrm{i}\omega\tau}\,\mathrm{d}\tau\,, \tag{2.51}$$

[††] Note that the definitions ensure $\dot{\boldsymbol{a}}(\tau) = -\boldsymbol{F}(\tau) \Leftrightarrow \dot{\boldsymbol{A}}(t) = -\boldsymbol{E}(t)$.

in terms of the scaled angular frequency $\omega = \Omega\, t_c$. The same notation is used for the intra- and interband contributions,

$$\boldsymbol{j}_{\text{intra}}(\tau) = \frac{t_c}{l_c^{1-d}} \boldsymbol{J}_{\text{intra}}(\tau t_c) = \sum_{n=1}^{N} \int_{BZ(\tau)} \rho_{nn}(\boldsymbol{\kappa}, \tau)\, \boldsymbol{j}_{nn}(\boldsymbol{\kappa}_\tau)\, \mathrm{d}\boldsymbol{\kappa} \quad \text{and} \tag{2.52}$$

$$\boldsymbol{j}_{\text{inter}}(\tau) = \frac{t_c}{l_c^{1-d}} \boldsymbol{J}_{\text{inter}}(\tau t_c) = \sum_{\substack{m,n=1 \\ m \neq n}}^{N} \int_{BZ(\tau)} \rho_{nn}(\boldsymbol{\kappa}, \tau)\, \boldsymbol{j}_{nn}(\boldsymbol{\kappa}_\tau)\, \mathrm{d}\boldsymbol{\kappa}\ , \tag{2.53}$$

to the total current density throughout this thesis. We define the dimensionless spectral emission intensity,

$$I(\omega) = \frac{\mathcal{I}(\omega/t_c)}{I_0} = \omega^2 |\boldsymbol{j}(\omega)|^2 = \omega^2 |\mathcal{F}[\boldsymbol{j}(\tau)](\omega)|^2 = \left| \mathcal{F}\left[\frac{\mathrm{d}\boldsymbol{j}}{\mathrm{d}\boldsymbol{t}} \right](\omega) \right|^2 , \tag{2.54}$$

through the characteristic intensity $I_0 = \frac{1}{3c^3\, t_c^2 l_c^{2-2d}}$.

2.5 Effective two-band models

A common strategy in condensed matter physics is the use of effective models formulated in $\boldsymbol{k}$ space, where a real material is approximated within a restricted region of the Brillouin zone or over a limited energy range. For example, the conduction and valence bands of graphene can be described by a Hamiltonian that is linear in $\boldsymbol{\kappa}$ in the vicinity of the K and K' points of the Brillouin zone [126]. Similarly, topological insulators of the Bi_2Se_3 family can be approximated by closely related low-energy Hamiltonians [127]. Such effective descriptions also have practical numerical implications, including the introduction of a cutoff in $\boldsymbol{\kappa}$ space or an "artificial Brillouin zone", as discussed in detail in [70].

In this work we investigate such effective models with two bands. These are described by a Hamiltonian of generic form,

$$\hat{H}(\boldsymbol{\kappa}) = \boldsymbol{h}(\boldsymbol{\kappa}) \cdot \boldsymbol{\sigma}\,, \tag{2.55}$$

with some real functions $\boldsymbol{h}(\boldsymbol{\kappa}) = \left(h_x(\boldsymbol{\kappa}), h_y(\boldsymbol{\kappa}), h_z(\boldsymbol{\kappa})\right)^T$ and the "vector" of Pauli matrices $\boldsymbol{\sigma} = \left(\sigma_x, \sigma_y, \sigma_z\right)^T$. The form of Hamiltonians in Equation 2.55 enables considerable simplification of matrix elements such as the dipoles.

Starting with the current matrix elements we use the Hellman-Feynman theorem to simplify the diagonals and the chain rule for the off-diagonals. This leads to the rather compact form,

$$\boldsymbol{j}_{mn}(\boldsymbol{\kappa}) = \langle\psi_m(\boldsymbol{\kappa})| \frac{\partial \hat{H}}{\partial \boldsymbol{\kappa}} |\psi_n(\boldsymbol{\kappa})\rangle = \begin{pmatrix} \frac{\partial \epsilon_c}{\partial \boldsymbol{\kappa}} & \sum_i \boldsymbol{e}_i \left[\frac{\partial \boldsymbol{h}}{\partial \kappa_i} \cdot \boldsymbol{\sigma}_{cv}(\boldsymbol{\kappa})\right] \\ \sum_i \boldsymbol{e}_i \left[\frac{\partial \boldsymbol{h}}{\partial \kappa_i} \cdot \boldsymbol{\sigma}_{vc}(\boldsymbol{\kappa})\right] & \frac{\partial \epsilon_v}{\partial \boldsymbol{\kappa}} \end{pmatrix}, \tag{2.56}$$

in terms of the Pauli matrix elements,

$$\boldsymbol{\sigma}_{mn}(\boldsymbol{\kappa}) = \langle\psi_m(\boldsymbol{\kappa})| \boldsymbol{\sigma} |\psi_n(\boldsymbol{\kappa})\rangle \ , \tag{2.57}$$

and unit vectors $\boldsymbol{e}_i$. In order to calculate $\boldsymbol{\sigma}_{mn}$ we need to specify the eigenstates, which can be chosen as

$$\langle\alpha|\psi_c(\boldsymbol{\kappa})\rangle = \frac{1}{\sqrt{h(\boldsymbol{\kappa})[h(\boldsymbol{\kappa}) + h_z(\boldsymbol{\kappa})]}} \begin{pmatrix} h(\boldsymbol{\kappa}) + h_z(\boldsymbol{\kappa}) \\ h_x(\boldsymbol{\kappa}) + \mathrm{i}\, h_y(\boldsymbol{\kappa}) \end{pmatrix} \tag{2.58a}$$

$$\langle\alpha|\psi_v(\boldsymbol{\kappa})\rangle = \frac{1}{\sqrt{h(\boldsymbol{\kappa})[h(\boldsymbol{\kappa}) + h_z(\boldsymbol{\kappa})]}} \begin{pmatrix} -h_x(\boldsymbol{\kappa}) + \mathrm{i}\, h_y(\boldsymbol{\kappa}) \\ h(\boldsymbol{\kappa}) + h_z(\boldsymbol{\kappa}) \end{pmatrix} \tag{2.58b}$$

with $h(\boldsymbol{\kappa}) = \|\boldsymbol{h}(\boldsymbol{\kappa})\|$ and eigenenergies $\epsilon_c(\boldsymbol{\kappa}) = h(\boldsymbol{\kappa})$ and $\epsilon_v(\boldsymbol{\kappa}) = -h(\boldsymbol{\kappa})$. Equation 2.58 fixes the *adiabatic gauge*[‡‡] of the states, which is also employed in our numerical simulations (see Appendix C). A quick calculation for Equation 2.57 with the basis defined in Equation 2.58 yields

$$\boldsymbol{\sigma}_{cv}(\boldsymbol{\kappa}) = \boldsymbol{\sigma}^*_{vc}(\boldsymbol{\kappa}) = \left(\frac{1}{h_x + \mathrm{i}\, h_y}\left[\mathrm{i}\, h_y + \frac{h_x h_y}{h}\right], \ \frac{1}{h_x + \mathrm{i}\, h_y}\left[-\mathrm{i}\, h_x + \frac{h_y h_z}{h}\right], \ \frac{-h_x + \mathrm{i}\, h_y}{h}\right)^T, \tag{2.59}$$

where we suppressed the $\boldsymbol{\kappa}$-dependence on the right-hand side. Using Equation 2.58, the dipoles can be brought into the form,

$$\boldsymbol{d}_{mn}(\boldsymbol{\kappa}) = \begin{pmatrix} \frac{1}{2h(h+h_z)}\left[\frac{\partial h_x}{\partial \boldsymbol{\kappa}} h_y - h_x \frac{\partial h_y}{\partial \boldsymbol{\kappa}}\right] & \frac{-\mathrm{i}}{\epsilon_{cv}} \boldsymbol{j}_{cv} \\ \frac{-\mathrm{i}}{\epsilon_{vc}} \boldsymbol{j}_{vc} & -\frac{1}{2h(h+h_z)}\left[\frac{\partial h_x}{\partial \boldsymbol{\kappa}} h_y - h_x \frac{\partial h_y}{\partial \boldsymbol{\kappa}}\right] \end{pmatrix}. \tag{2.60}$$

[‡‡] All states connected via the transformation $|\psi_n(\boldsymbol{\kappa})\rangle \to \mathrm{e}^{\mathrm{i}\varphi(\boldsymbol{\kappa})} |\psi_n(\boldsymbol{\kappa})\rangle$ with $\varphi(\boldsymbol{\kappa}) \in \mathbb{R}$ are also valid (normalized) eigenstates, which is usually called gauge freedom. This should not be confused with the electromagnetic gauge, see [41] for a pedagogical introduction.

2.6 The three step model

There are several useful analytical approximations for the SBE in various different context. For example, perturbation theory in the field strength is established as an important tool for calculating the optical response of semiconductors [121, 128–131] and can also be applied to transition metal dichalcogenides [132, 133] or DC remnants in Dirac models [69, 70]. Another approximation, which is frequently used in the context of HHG, is the three-step model (or Lewenstein model or semi-classical recollision model). It was originally found as a beautiful explanation for atomic HHG [14, 72], experimentally verified in various scenarios [6, 15, 17, 18, 134], and later adapted to the solid-state context [37, 39]. There exist various extensions of the model including "imperfect recollisions" [41, 42, 71] and a mixed position-reciprocal space model [43].

We start by introducing the three-step model in the most frequently discussed fashion, applying it to Section 2.4. For simplicity, a two-band effective model is considered in the following, but the generalization to multiple bands is straightforward within the approximations presented here. Additionally, one assumes a Fermi level in the band gap[§§], i.e. an initially filled valence band and empty conduction band (see Equation 2.31). Using the fact that $\rho_{cv} = \rho_{vc}^*$, the SBE for a two-band model can be reduced to two coupled equations,

$$\frac{\partial w}{\partial \tau} = -\mathrm{i}\boldsymbol{F}(\tau)\cdot\left[\rho_{cv}(\boldsymbol{\kappa},\tau)\,\boldsymbol{d}_{vc}(\boldsymbol{\kappa}_\tau) - \text{c.c.}\right] \tag{2.61}$$

$$\begin{aligned}\frac{\partial \rho_{cv}}{\partial \tau} = &-\left[\frac{1}{\tau_2} + \mathrm{i}\epsilon_{cv}(\boldsymbol{\kappa}_\tau)\right]\rho_{cv}(\boldsymbol{\kappa},\tau) + \\ &- \mathrm{i}\boldsymbol{F}(\tau)\cdot\left[\boldsymbol{d}_{cv}(\boldsymbol{\kappa}_\tau)w(\boldsymbol{\kappa},\tau) + \rho_{cv}(\boldsymbol{\kappa},\tau)[\boldsymbol{d}_{vv}(\boldsymbol{\kappa}_\tau) - \boldsymbol{d}_{cc}(\boldsymbol{\kappa}_\tau)]\right],\end{aligned} \tag{2.62}$$

with the population imbalance $w(\boldsymbol{\kappa},\tau) = [\rho_{cc}(\boldsymbol{\kappa},\tau) - \rho_{vv}(\boldsymbol{\kappa},\tau)]/2$. One convenient route to the three-step model is to define an auxiliary function,

$$u(\boldsymbol{\kappa},\tau) = \rho_{cv}(\boldsymbol{\kappa},\tau)\mathrm{e}^{-\mathrm{i}\phi_d(\boldsymbol{\kappa},\tau,\tau_0)-\mathrm{i}\phi_g(\boldsymbol{\kappa},\tau,\tau_0)+\frac{\tau-\tau_0}{\tau_2}}, \tag{2.63}$$

which contains the dynamical phase [82],

$$\phi_d(\boldsymbol{\kappa},\tau_f,\tau_i) = \int_{\tau_i}^{\tau_f}\mathrm{d}\tau\,\epsilon_{cv}(\boldsymbol{\kappa}_\tau), \tag{2.64}$$

[§§] In the case of a gapless system we assume a Fermi level located at the band crossing.

and the geometric (Berry) phase [84],

$$\phi_g(\boldsymbol{\kappa}, \tau_f, \tau_i) = \int_{\tau_i}^{\tau_f} \mathrm{d}\tau \boldsymbol{F}(\tau) \cdot [\boldsymbol{d}_{cc}(\boldsymbol{\kappa}_\tau) - \boldsymbol{d}_{vv}(\boldsymbol{\kappa}_\tau)] \,. \tag{2.65}$$

These definitions simplify the equations of motion,

$$\frac{\partial w}{\partial \tau} = -\mathrm{i}\boldsymbol{F}(\tau) \cdot \left[u(\boldsymbol{\kappa}_\tau, \tau)\, \boldsymbol{d}_{vc}(\boldsymbol{\kappa}_\tau) \mathrm{e}^{\mathrm{i}\phi_d(\boldsymbol{\kappa},\tau,\tau_0)+\mathrm{i}\phi_g(\boldsymbol{\kappa},\tau,\tau_0)-\frac{\tau-\tau_0}{\tau_2}} - \mathrm{c.c.} \right] \tag{2.66}$$

$$\frac{\partial u}{\partial \tau} = -\mathrm{i}\boldsymbol{F}(\tau) \cdot \boldsymbol{d}_{cv}(\boldsymbol{\kappa}_\tau) w(\boldsymbol{\kappa}, \tau)\, \mathrm{e}^{-\mathrm{i}\phi_d(\boldsymbol{\kappa},\tau,\tau_0)-\mathrm{i}\phi_g(\boldsymbol{\kappa},\tau,\tau_0)+\frac{\tau-\tau_0}{\tau_2}} \,, \tag{2.67}$$

such that they can be decoupled by integrating one and plugging it into the other. One can use this integral form to build a Dyson/Neumann series in the dimensionless driving field $\boldsymbol{F}$,

$$\begin{aligned} w(\boldsymbol{\kappa}, \tau) = w_i + \Bigg\{ \int_{\tau_i}^{\tau_f} \mathrm{d}\tau_1\, g(\tau_1) \mathrm{e}^{\mathrm{i}S(\tau_1,\tau_i)} \times \\ \times \left[u_i + \int_{\tau_i}^{\tau_1} \mathrm{d}\tau_2\, h(\tau_2) \mathrm{e}^{-\mathrm{i}S(\tau_2,\tau_i)} \{ w_i + \ldots \} \right] + \mathrm{c.c.} \Bigg\} \end{aligned} \tag{2.68}$$

$$\begin{aligned} u(\boldsymbol{\kappa}, \tau) = u_i + \int_{\tau_i}^{\tau_f} \mathrm{d}\tau_1\, h(\tau_1) \mathrm{e}^{-\mathrm{i}S(\tau_1,\tau_i)} \Bigg\{ w_i + \\ + \left[\int_{\tau_i}^{\tau_1} \mathrm{d}\tau_2\, g(\tau_2) \mathrm{e}^{\mathrm{i}S(\tau_2,\tau_i)} \{ u_i + \ldots \} + \mathrm{c.c.} \right] \Bigg\} \,, \end{aligned} \tag{2.69}$$

where we suppressed the $\boldsymbol{\kappa}$-dependence in the abbreviations

$$w_i \equiv w(\boldsymbol{\kappa}, \tau_i) \,, \quad u_i \equiv u(\boldsymbol{\kappa}, \tau_i) \,, \tag{2.70a}$$

$$S(\tau_f, \tau_i) \equiv S(\boldsymbol{\kappa}, \tau_f, \tau_i) = \phi_d(\boldsymbol{\kappa}, \tau_f, \tau_i) + \phi_g(\boldsymbol{\kappa}, \tau_f, \tau_i) + \mathrm{i}\frac{\tau_f - \tau_i}{\tau_2} \,, \tag{2.70b}$$

$$h(\tau) \equiv h(\boldsymbol{\kappa}, \tau) = -\mathrm{i}\boldsymbol{F}(\tau) \cdot \boldsymbol{d}_{cv}(\boldsymbol{\kappa}_\tau) \,, \tag{2.70c}$$

$$\text{and} \quad g(\tau) \equiv g(\boldsymbol{\kappa}, \tau) = -\mathrm{i}\boldsymbol{F}(\tau) \cdot \boldsymbol{d}_{vc}(\boldsymbol{\kappa}_\tau) \,. \tag{2.70d}$$

The central assumption in [37] and following works [39, 41, 42, 71] is a low valence band depletion[¶¶],

$$w(\boldsymbol{\kappa}, \tau) \approx -1/2 \,, \tag{2.71}$$

which is equivalent to truncating Equation 2.68 at the first non-vanishing

[¶¶] Sometimes called Keldysh approximation [37].

order*** in $\boldsymbol{F}$. This assumption is fairly restrictive and one can easily imagine a situation where it is not justified: for systems with a small band gap the transition probability is large in the vicinity where the bands approach each other. In Chapter 3 we will encounter such a situation and introduce an analytical tool tailored to that scenario.

The determining quantity (up to constants and a factor of ω^2) for the emission intensity is the Fourier transform of the induced current density, see Equation 2.54. Assuming low valence band depletion and keeping only the leading order in $\boldsymbol{F}$ we find

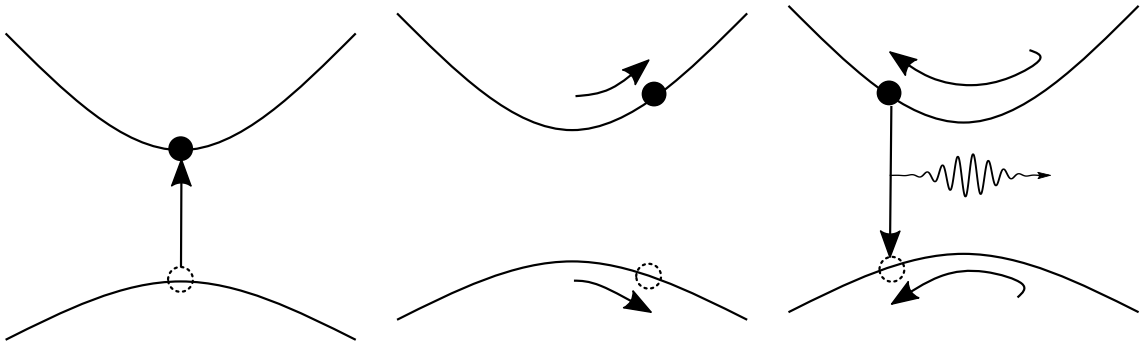
$$\begin{aligned}\boldsymbol{j}_{\text{inter}}(\omega) \approx & \int_{-\infty}^{\infty} \mathrm{d}\tau\, \mathrm{e}^{-\mathrm{i}\omega t} \int_{BZ} \mathrm{d}\boldsymbol{\kappa}\, \boldsymbol{j}_{cv}(\boldsymbol{\kappa}) \times \\ & \times \left\{ \int_{-\infty}^{\tau} \mathrm{d}\tau'\, h(\boldsymbol{\kappa} + \boldsymbol{a}(\tau), \tau') \mathrm{e}^{-\mathrm{i}S(\boldsymbol{\kappa}+\boldsymbol{a}(\tau),\tau,\tau')} + \text{c.c.} \right\}, \qquad (2.72) \\ \boldsymbol{j}_{\text{intra}}(\omega) \approx & 2 \int_{-\infty}^{\infty} \mathrm{d}\tau\, \mathrm{e}^{-\mathrm{i}\omega t} \int_{BZ} \mathrm{d}\boldsymbol{\kappa}\, \boldsymbol{j}_{cc}(\boldsymbol{\kappa}) \left\{ \int_{-\infty}^{\tau} \mathrm{d}\tau'\, g(\boldsymbol{\kappa} + \boldsymbol{A}(\tau), \tau') \times \right. \\ & \left. \times \int_{-\infty}^{\tau'} \mathrm{d}\tau''\, h(\boldsymbol{\kappa} + \boldsymbol{a}(\tau), \tau'') \mathrm{e}^{-\mathrm{i}S(\boldsymbol{\kappa}+\boldsymbol{a}(\tau),\tau'',\tau')} + \text{c.c.} \right\}, \qquad (2.73)\end{aligned}$$

where we let $\tau_i \to -\infty$. The essential strategy of the three-step model in solids [37] is to assume the prefactors of the integrals in Equation 2.72 are slowly varying functions of τ, $\boldsymbol{\kappa}$, τ', and τ'' respectively as compared to the exponentials. In that regime, the integrals can be treated with stationary phase approximation or saddle-point methods [93, 96]. The power of these methods lies not only in quantitative analysis but also in their connection to semi-classical physics, where $S(\boldsymbol{\kappa}, \tau_1, \tau_2)$ plays the role of a classical action. It is possible to get a physical understanding of the microscopic processes that contribute to HHG in that fashion. If mathematical rigor is desired in identifying such an action, a dimensionless number should be factored out in the exponential, e.g. $S(\boldsymbol{\kappa}, \tau, \tau') = \lambda \tilde{S}(\boldsymbol{\kappa}, \tau, \tau')$ with $\tilde{S}$ independent of λ. The scaling discussed in Section 2.4 can be useful in identifying such dimensionless quantities, but it is always system-dependent and in general difficult or impossible.

Here we follow [37] and only consider the interband current, because the intraband contribution is higher order in $\boldsymbol{F}$, see Equation 2.72. We identify the classical action as

$$S_{\text{cl}}(\boldsymbol{\kappa} + \boldsymbol{a}(\tau), \tau, \tau') = \phi_d(\boldsymbol{\kappa} + \boldsymbol{a}(\tau), \tau, \tau') - \omega\tau \ ,$$

*** Considering that $u_i = 0$ and $w_i = -1/2$ this means one integral for $u(\boldsymbol{\kappa}, \tau)$ and two for $w(\boldsymbol{\kappa}, \tau)$.



(a) Step 1: "Ionization", i.e. tunneling of a valence electron to the conduction band.

(b) Step 2: "Propagation". The electron/hole moves according to classical equations of motion.

(c) Step 3: "Recollision". If electron and hole collide in position space, they recombine by emitting a photon.

Figure 2.4: The Lewenstein/three-step model of HHG in two-band models, see [14, 37, 39].

i.e. we neglect the geometric phase and the dephasing term, also as in [37]. For the interband current, the action S_{cl} is stationary for

$$\epsilon_{cv}(\boldsymbol{\kappa} + \boldsymbol{a}(\tau) - \boldsymbol{a}(\tau')) = 0 \tag{2.74a}$$

$$\int_{\tau'}^{\tau} \mathrm{d}\tau'' \, \frac{\partial}{\partial \boldsymbol{\kappa}} \epsilon_{cv}(\boldsymbol{\kappa} + \boldsymbol{a}(\tau) - \boldsymbol{a}(\tau'')) = 0 \tag{2.74b}$$

$$\epsilon_{cv}(\boldsymbol{\kappa}) = \omega \, . \tag{2.74c}$$

The three steps illustrated in Figure 2.4 can now be read off Equation 2.74: step one is the tunneling of an electron from valence to conduction band at some (generally complex) time τ'. In the second the created electron (hole) travels according to classical equations of motion (group velocity from ϵ_{cv}) from time τ' to τ. At the end those trajectories where electron and hole collide after time $\tau' - \tau$ a photon with its energy given by the band gap at the instant of collision $\epsilon_{cv}(\boldsymbol{\kappa})$ is emitted.

Example Let us introduce a simple toy model which serves to illustrate the three-step model of HHG. Consider the one-dimensional Hamiltonian,

$$\hat{\mathscr{H}}_{\mathrm{ZnO}}(k_x) = \Delta \, \hat{\sigma}_x - t \sin(k_x a_x/2) \, \hat{\sigma}_z \, , \tag{2.75}$$

with band gap $2\Delta = 0.121$ a.u., hopping integral $t = 0.145$ a.u., and lattice constant $a_x = 5.21$ a.u.. These parameters are chosen such that the Hamiltonian fits a realistic, three-dimensional model for ZnO given in

[39], which is widely used and backed by several density functional theory (DFT) simulations (see [37, 40, 135–138]). Details of the three-dimensional model and a comparison to Equation 2.75 are shown in Appendix A. We drive the one-dimensional Hamiltonian by a pulse,

$$\boldsymbol{E}(t) = -\frac{\partial \boldsymbol{A}}{\partial t}, \quad \boldsymbol{A}(t) = \frac{E_0}{\Omega_0}\boldsymbol{e}_x \cos(\Omega_0 t)\mathrm{e}^{-t^2/2T_d^2}, \tag{2.76}$$

with peak field strength $E_0 = 0.00389$ a.u. $= 20.0\,\mathrm{MV\,cm^{-1}}$, central angular frequency $\Omega_0 = 0.0140$ a.u. and standard deviation to $T_d = 4\,T_0$. This driving field's time dependency is depicted in Figure 2.5. As characteristic time and length scales we set

$$t_c = \frac{1}{\Omega_0} \quad \text{and} \quad l_c = a_x\,, \tag{2.77}$$

such that $\kappa_x = a_x k_x$ and $\epsilon_{cv} = \varepsilon_{cv}/\Omega_0$ (according to Equation 2.47).

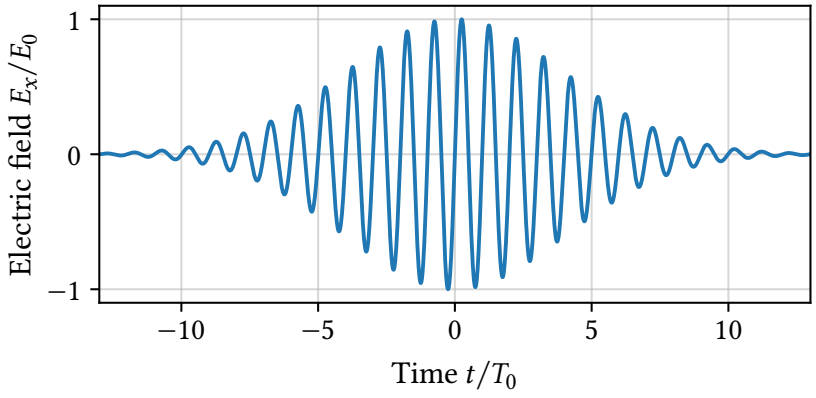


Figure 2.5: Time-dependence of the electric field in terms of peak field strength $E_0 = 0.00389$ a.u. $= 0.200\,\mathrm{MV\,cm^{-1}}$ with the formula given in Equation 2.76. The central angular frequency is set to $\Omega_0 = 0.0140$ a.u. (equivalent to $\nu = \Omega_0/2\pi = 92.2$ THz or $\lambda = 3.25\,\mu$m). The envelope's standard deviation is given by $T_d = 4\,T_0$ in terms of laser period $T_0 = 2\pi/\Omega_0$.

Employing the SBE (cf. Equation 2.30 and Section 2.4) we calculate system's time evolution and employ Larmor's formula (see Equations 2.41 and 2.54) in order to calculate the high-harmonic emission spectrum. The resulting data is shown in Figure 2.6, which shows only odd harmonics appearing. This harmonic structure results from driving along the x-axis, which lies in the basal plane of the hexagonal wurtzite structure and therefore preserves inversion symmetry. The z-axis on the other hand breaks inversion symmetry, such that even harmonics would appear for driving with non-vanishing z-component of the field. Additionally, the spectral intensity $I(\omega)$ is dominated by interband emission above and intraband emission below the band-gap.

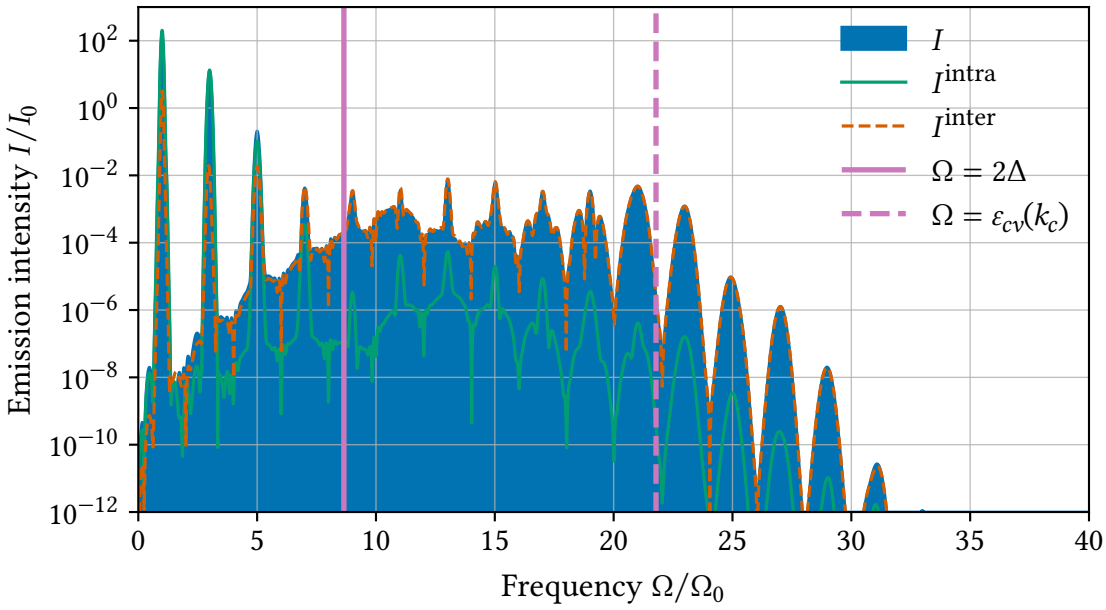


Figure 2.6: Spectral emission intensity (solid blue) from Equation 2.54 for a one-dimensional Semiconductor model (cf. Equation 2.75) decomposed into intra- (green line) and interband (dashed orange line) contributions (see Equation 3.13). The frequency equivalent of the band gap (solid purple) and the maximum re-collision energy (dashed purple) are shown as a vertical lines.

One can estimate the maximum transition probability with the Landau-Zener formula (see Equation 2.20), which gives $\max_k (P_{LZ}(k)) = 0.280$. Consequently, assuming low valence band depletion necessary for the three-step model as presented above seems unjustified. One must keep in mind, however, that most k-modes have a lower transition probability and it is also possible to generalize the Lewenstein model to arbitrarily large transition probabilities. For this generalization one can use the adiabatic impulse approximation instead of the integral form, Equation 2.68, before applying stationary phase approximation to the $\boldsymbol{\kappa}$ and τ-integrals. This approach introduces a small additional term to Equation 2.74, because the birth time is then fixed for each $\boldsymbol{k}$-mode.

Despite the rather large transition probability, we shall see that the three-step model can still be applied in a semi-quantitative way. To solve Equation 2.74 we follow [37, 39, 41, 42] and approximate Equation 2.74a by

$$\epsilon_{cv}(\kappa + a_x(\tau) - a_x) \approx 2\frac{\Delta}{\Omega_0} \quad \Rightarrow \quad \kappa + a_x(\tau) - a_x \approx 0\,, \tag{2.78}$$

which can be solved for the birth time τ'. This approximation neglects the imaginary component of the birth time τ', which would lead to the

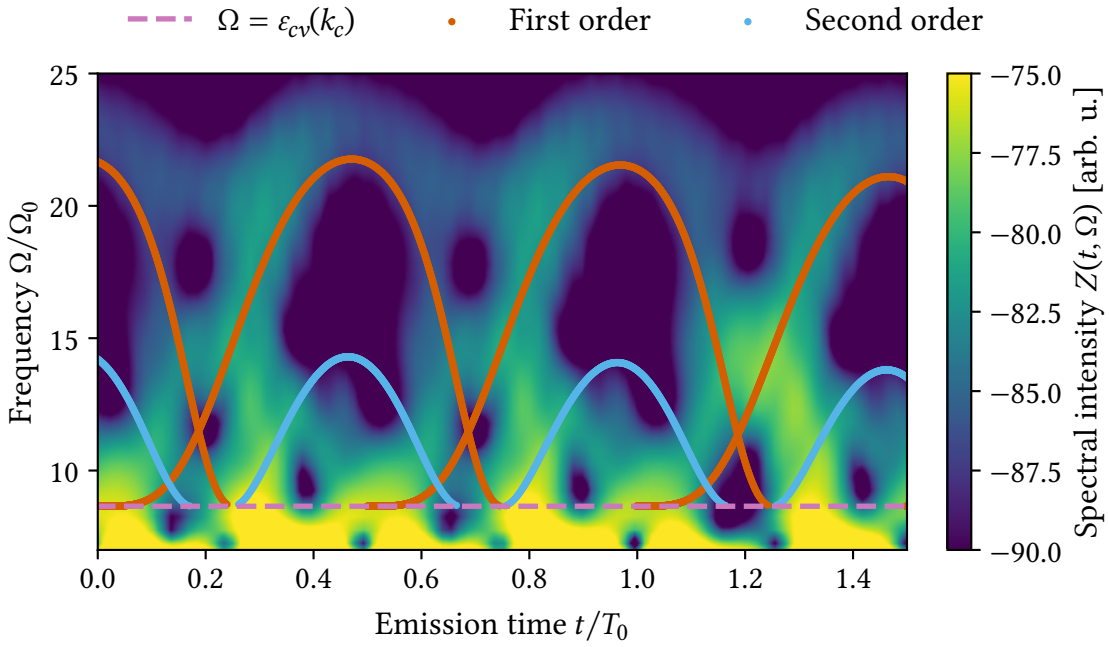


Figure 2.7: Time-frequency profiles (Equation 2.79) as heatmap plot from the one-dimensional model for a Semiconductor shown in Equation 2.75. The driving field is depicted in Figure 2.5 and its analytic form given in Equation 2.76. The orange (blue) lines show the first (second) order semi-classical re-collision events calculated from Equation 2.74 with the approximation given in Equation 2.78. The band gap energy is marked by a horizontal dashed purple line.

tunneling[†††] (approximately Landau-Zener) probability. Equations 2.74b and 2.74c are then solved numerically to obtain re-collision time τ and wave number κ. We label the wave vector with the *maximal re-collision energy* by $\kappa_c = a_x k_c$; this energy is marked in Figure 2.6 by a dashed vertical line. Clearly, the characteristic HHG plateau ranges from $\omega = 2\Delta$ to $\omega = \varepsilon_{cv}(k_c)$, which is a first indication that the three-step model at least qualitatively describes the underlying physics.

A more convincing analysis is provided in Figure 2.7 by a spectrogram (Gabor transformation or short-time Fourier transformation),

$$Z(t,\omega) = \left| \int_{-\infty}^{\infty} \mathrm{d}s\, \mathrm{e}^{-(s-t)^2/2w^2} \mathrm{e}^{-\mathrm{i}\omega s} j_{x,\mathrm{inter}}(s) \right|^2 , \tag{2.79}$$

with $w = 0.4\,T_0$. This quantity shows the frequency content in a time-resolved manner. It is then possible to compare $Z(t,\omega)$ with the re-collision energies and times from the semi-classical model, as the window is chosen so short that only a single re-collision event at a given frequency and time takes place, see [39–42]. At this point it is important to note that

[†††] This integral is treated in [139] and the same result can be obtained by WKB theory [140].

there is more than one trajectory calculated from Equations 2.74 and 2.78: the *first* order solution corresponds to electron and hole re-combining upon meeting in position space for the *first* time. Consequently, the *second* order event occurs when electron and hole encounter each other for the *second* time, and so on. However, each trajectory of duration τ_d contribution comes with a factor $e^{-\tau_d/\tau_2}$, such that higher orders are suppressed exponentially by dephasing.

Figure 2.7 compares the first and second order re-collision events with the Gabor transformation of the interband current. The comparison shows clear signatures of the first order solutions, but the second order is not as clearly distinguishable. While being consistent with the exponential suppression of higher orders, in regions where solutions come close one can expect interference to play a role, which is not reflected by simply plotting the solutions time and energy as presented in Figure 2.7. Moreover, the Gabor transformation's resolution is also limited by a Heisenberg uncertainty relation of time and energy such that the required sub-cycle time resolution comes at the cost of reduced energetic precision. Additionally, for saddle-point, stationary phase or related asymptotic approximations it is expected that they break down at the "caustics", which are located at maximum and minimum re-collision energies[‡‡‡] in Figure 2.7. We made several additional approximations for calculating the re-collision events (neglect complex time, low valence band depletion), which makes it difficult to judge whether this version of the Lewenstein model is applicable to a specific given physical system.

This difficulty of several approximations ultimately limits the generality of the semi-classical re-collision model and its various variants. In Chapter 3 we present a physical situation beyond this model and develop an alternative analytical approach.

2.7 Floquet theory

In this section we review a theoretical method that is useful from a numerical and a conceptual perspective for the description of time-dependent physical systems. Floquet theory is a well-known formalism for dealing with linear systems of ordinary differential equations with periodic

[‡‡‡] The caustics, where multiple stationary/saddle points coalesce, are typically located at the boundary of classically allowed and forbidden regions, see [141–144]. Uniform approximations around these are possible but notoriously challenging mathematically.

coefficients [73], so we keep our introduction brief here. The Floquet theorem can be viewed as a more general version of the Bloch theorem in solid state theory, which concerns electrons in periodic potentials. In the context of quantum mechanics Floquet theory usually refers to the special case of time-periodic Hamiltonians,

$$\hat{\mathscr{H}}_{\mathrm{per}}(t + T_0) = \hat{\mathscr{H}}_{\mathrm{per}}(t) \,,$$

of period T_0. The aim is to construct a solution to the time-dependent Schrödinger equation (TDSE),

$$\mathrm{i}\frac{\mathrm{d}}{\mathrm{d}t}\,|\psi(t)\rangle = \hat{\mathscr{H}}_{\mathrm{per}}(t)\,|\psi(t)\rangle \;.$$

According to the Floquet theorem [73, 74] any solution $|\psi(t)\rangle$ of the TDSE can be expanded in the Floquet basis,

$$|\psi(t)\rangle = \sum_b f_b \left|\varphi_b^F(t)\right\rangle \,,$$

with the constants $f_a \in \mathbb{C}$. The so-called Floquet functions,

$$|\varphi_a(t)\rangle = \mathrm{e}^{-\mathrm{i}\xi_a t}\,|u_a(t)\rangle \;, \tag{2.80}$$

can be expressed in terms of the T_0-periodic states $|u_a(t + T_0)\rangle = |u_a(t)\rangle$. Hereby, ξ_a is the *quasi-energy* which is conserved as a result of the discrete time translation invariance of the problem. The time-periodic part of the Floquet functions obey an eigenvalue equation,

$$\left[\hat{\mathscr{H}}_{\mathrm{per}}(t) - \mathrm{i}\frac{\mathrm{d}}{\mathrm{d}t}\right]|u_a(t)\rangle = \xi_a\,|u_a(t)\rangle \;, \tag{2.81}$$

which reveals the "Brillouin-zone structure" of the quasi-energies: if $|u_a(t)\rangle$ is a solution of Equation 2.81 with eigenvalue ξ_a, then $\mathrm{e}^{\mathrm{i}m\Omega_0 t}\,|u_a(t)\rangle$ is a solution with eigenvalue $\xi_a + m\Omega_0$ for $m \in \mathbb{Z}$. However, this solution describes the *same* Floquet function (see Equation 2.80). The quasi-energy ξ_a is then analogous to the Bloch wave-vector $\boldsymbol{k}$ and correspondingly we introduce the *first Floquet Brillouin zone* (1FBZ),

$$-\Omega_0/2 \leq \xi_a^{\mathrm{1FBZ}} < \Omega_0/2 \,,$$

in analogy to the case of periodic crystals. Those quasi-energies which are shifted by integer multiples of the driving photon energy,

$$\xi_{(a,l)} = \xi_a^{1\mathrm{FBZ}} + l\Omega_0 \ ,$$

are often referred to as *sidebands* or *replicas* and are crucial in the following discussion.

Experimental observables The analysis and interpretation of Floquet states is interesting in its own right, however it gained even more relevance with the advent of more precise and sophisticated experimental possibilities. Specifically, the occupations in Floquet replicas are related to the emission probability as it is measured in *photoelectron spectroscopy*. *Angle-resolved photoelectron spectroscopy* (ARPES) and especially its time-resolved variant (trARPES) provide fascinating opportunities to observe Floquet physics.

ARPES experiments utilize the photoelectric effect by shining monochromatic light on a solid-state sample, which frees electrons from the material. A photoemission spectrometer is then used to measure the freed electron's kinetic energy and emission angles. Through use of momentum and energy conservation laws the binding energy can be calculated and in turn the band structure can be determined.

For trARPES a pump-probe setup is usually employed, i.e. a weaker probe pulse follows a pump pulse with a certain time delay. ARPES data is then recorded as a function of this time delay to observe different dynamical phenomena. For example, in [55] the first direct imaging of Floquet-Bloch sidebands was achieved.

We follow [3, 145] in order to connect the Floquet formalism presented above to trARPES measurements. Neglecting the effect of the probe pulse and laser-assisted photo emission (LAPE) the transition probability is proportional to

$$P(\Omega) \propto \sum_{b,m} |f_b|^2 \left|f_{m,b}\right|^2 \delta(\xi_b + m\Omega_0 - \Omega) \tag{2.82}$$

with the projections $f_{m,b} = \left\langle u_b^{(m)} \middle| \psi(t_i) \right\rangle$ of the initial state onto the m-th replica. LAPE can be taken into account by including Volkov states—free electron states dressed by the pump field—into Equation 2.82, which also

possess Floquet replicas owing to the pump field, see [145–148]. Throughout this thesis we neglect these dressed states, which were shown to be suppressed for in-plane polarized driving fields considered in Chapter 4, see [56, 62]. Clearly this connection to experiment is much less concrete/precise than in seminal works building on nonequilibrium Green's functions (see [56, 62, 146, 149]) or also ab-initio approaches as presented in [150, 151]. Rather we seek a more explicit connection to Floquet theory for easier interpretation. However, there are possibilities to further develop Floquet theory and the t–t' method presented below and consequently move towards a more accurate description of experiments, see Section 4.4.

Finite pulses Up to this point, we exclusively focused on *perfectly time-periodic* systems, which leads to constant expansion coefficients f_a. In this work we are interested in driving systems with finite pulses, potentially only a few cycles long. There are various different perspectives regarding the generalization of Floquet theory to non-periodic systems. Firstly the t–t'-method was introduced primarily as a numerical tool [75–77] to deal with the appearance of two separate time scales: a fast and a slow time scale, e.g. the central driving frequency of a laser pulse and its slowly varying carrier envelope. Following a more analytically-inclined route a related formalism has been developed [78, 152, 153] with focus on adiabaticity and Landau-Zener-like transitions. Some authors [79, 80] refer to this as the "instantaneous Floquet state" (IFS) formalism. It has been applied to various physical scenarios including but not limited to molecules driven by chirped laser pulses [154], excitonic Floquet states in monolayer WSe_2[155], and photodissociation resonances in H_2^+[156–158]. Both t–t' method and IFS formalism employ an extension of the Hilbert space as a core idea to include the second time-scale. In a nutshell one allows the coefficients in the Floquet expansion to become time-dependent, i.e. $f_a \to f_a(t)$.

We closely follow [3] and briefly summarize the statements and equations. For an (effective) Bloch Hamiltonian $\hat{\mathscr{H}}_0(\boldsymbol{k})$ and upon including the external driving via minimal coupling[§§§], $\boldsymbol{k} \to \boldsymbol{k} - \boldsymbol{A}(t)$, the full Hamiltonian can be expressed in the form

$$\hat{\mathscr{H}}(\boldsymbol{k}, t) \equiv \hat{\mathscr{H}}_0(\boldsymbol{k} - \boldsymbol{A}(t)) = \hat{\mathscr{H}}(\boldsymbol{k}, \eta(t), t) = \hat{\mathscr{H}}_0(\boldsymbol{k}) + \hat{W}(\boldsymbol{k}, \eta(t), t)\,. \tag{2.83}$$

[§§§] See Section 2.5 for the connection of the SBE to this approach.

Hereby, we defined $\hat{W}(\boldsymbol{k}, \eta(t), t)$ as the time-dependent part of the full Hamiltonian and introduced the auxiliary variable $\eta(t)$, which describes the slow time scale, e.g. the pulse's variation with time. The latter must be chosen such that for fixed $\boldsymbol{k}$ and η the time-dependent part $\hat{W}$ is periodic in time,

$$\hat{W}(\boldsymbol{k}, \eta, t + T_0) = \hat{W}(\boldsymbol{k}, \eta, t) \,. \tag{2.84}$$

This enables the introduction of instantaneous Floquet states,

$$\left|\phi_a^F(\boldsymbol{k}, \eta, t)\right\rangle = \mathrm{e}^{-\mathrm{i}\xi_a(\boldsymbol{k},\eta)t} \left|u_a(\boldsymbol{k}, \eta, t)\right\rangle \,, \tag{2.85}$$

for each η. To keep track of sidebands, we define the double index $\alpha = (a, l)$, such that the Floquet states and their quasi-energies,

$$\left|u_\alpha(\boldsymbol{k}, \eta, t)\right\rangle = \mathrm{e}^{\mathrm{i}l\Omega_0 t} \left|u_a \boldsymbol{k}, \eta, t)\right\rangle \,, \tag{2.86}$$

$$\xi_\alpha(\boldsymbol{k}, \eta) = \xi_a(\boldsymbol{k}, \eta) + l\Omega_0 \,, \tag{2.87}$$

can be written down succinctly. Instead of choosing $\xi_a(\boldsymbol{k}, \eta)$ to lie in the 1FBZ, we define it by the limit

$$\lim_{\hat{W}\to 0} \xi_a(\boldsymbol{k}, \eta) = \epsilon_a(\boldsymbol{k}) \,, \tag{2.88}$$

i.e. it reduces to the unperturbed band dispersions ϵ_a in the limit of vanishing driving. Analogously to Equation 2.81, the periodic part of the instantaneous Floquet states solves an eigenvalue equation,

$$\left[\hat{\mathscr{H}}(\boldsymbol{k}, \eta, t) - \mathrm{i}\frac{\mathrm{d}}{\mathrm{d}t}\right] \left|u_\alpha(\boldsymbol{k}, \eta, t)\right\rangle = \xi_\alpha(\boldsymbol{k}, \eta) \left|u_\alpha(\boldsymbol{k}, \eta, t)\right\rangle \,, \tag{2.89}$$

for fixed η. As a result of the time periodicity, Equation 2.89 can be reduced to a linear system of equations by a Fourier series expansion,

$$\left|u_\alpha(\boldsymbol{k}, \eta, t)\right\rangle = \sum_{m\in\mathbb{Z}} \mathrm{e}^{-\mathrm{i}\,m\,t} \left|u_\alpha^{(m)}(\boldsymbol{k}, \eta)\right\rangle \,. \tag{2.90}$$

It is straightforward to show [3] that the solution of the TDSE with the Hamiltonian $\hat{\mathscr{H}}(\boldsymbol{k}, \eta(t), t)$ is given by

$$\left|\psi(\boldsymbol{k}, t)\right\rangle = \sum_\alpha c_\alpha(\boldsymbol{k}, t) \left|u_\alpha(\boldsymbol{k}, \eta, t)\right\rangle \,, \tag{2.91}$$

with the coefficients obeying

$$\mathrm{i}\frac{\mathrm{d}c_\alpha}{\mathrm{d}t} = \sum_\beta \mathscr{H}^{tt'}_{\alpha\beta}(\boldsymbol{k},\eta(t))\, c_\beta(\boldsymbol{k},t)\,, \tag{2.92a}$$

$$\mathscr{H}^{tt'}_{\alpha\beta}(\boldsymbol{k},\eta(t)) = \delta_{\alpha\beta}\,\xi_\alpha(\boldsymbol{k},t) - \mathrm{i}\frac{\mathrm{d}\eta}{\mathrm{d}t}G^{tt'}_{\alpha\beta}(\boldsymbol{k},\eta)\,, \tag{2.92b}$$

$$G^{tt'}_{\alpha\beta}(\boldsymbol{k},\eta) = \sum_{m\in\mathbb{Z}} \left\langle u_a^{(m+l-l')}(\boldsymbol{k},\eta)\middle|\frac{\partial}{\partial\eta}u^{(m)}_{a'}(\boldsymbol{k},\eta)\right\rangle\,, \tag{2.92c}$$

with $\alpha = (a,l)$ and $\beta = (a',l')$. We employ the parallel transport condition,

$$\left\langle u_a^{(m)}(\boldsymbol{k},\eta)\middle|\frac{\partial}{\partial\eta}u_a^{(m)}(\boldsymbol{k},\eta)\right\rangle = 0, \tag{2.93}$$

which fixes the gauge of the $\left|u_\alpha^{(m)}(\boldsymbol{k},\eta)\right\rangle$. The left-hand side of Equation 2.93 is nothing but the Berry connection (cf. Equation 2.9). Therefore, one must be careful in demanding parallel transport, since this condition can only be satisfied within one topological sector. Otherwise one picks up a geometric phase [3, 80, 84, 89].

Using the definition

$$a_\alpha(\boldsymbol{k},t) = c_\alpha(\boldsymbol{k},t)\mathrm{e}^{\mathrm{i}\int^t \mathrm{d}t'\xi_\alpha(\boldsymbol{k},t')}\,, \tag{2.94}$$

Equation 2.92 becomes form-equivalent to Equation 2.5,

$$\frac{\mathrm{d}a_\alpha}{\mathrm{d}t} = -\frac{\mathrm{d}\eta}{\mathrm{d}t}\sum_\beta G^{tt'}_{\alpha\beta}(\boldsymbol{k},\eta)\, a_\beta(\boldsymbol{k},\eta)\mathrm{e}^{\mathrm{i}\int^t \mathrm{d}t'\left[\xi_\alpha(\boldsymbol{k},t')-\xi_\beta(\boldsymbol{k},t')\right]}\,, \tag{2.95}$$

with η playing the role of the adiabatic parameter. Therefore, everything discussed in Section 2.1 immediately carries over to Equation 2.95, in particular Landau-Zener transitions and adiabatic perturbation theory. The latter can be given explicitly via

$$a_\alpha(\boldsymbol{k},t) \approx a^{(0)}_\alpha(\boldsymbol{k},t) + \frac{\mathrm{d}\eta}{\mathrm{d}t}a^{(1)}_\alpha(\boldsymbol{k},t) \tag{2.96a}$$

$$a^{(0)}_\alpha(\boldsymbol{k},t) = \delta_{\alpha\beta} \tag{2.96b}$$

$$a^{(1)}_\alpha(\boldsymbol{k},t) \approx -\frac{G^{tt'}_{\alpha\beta}}{\xi_\alpha(\boldsymbol{k},t)-\xi_\beta(\boldsymbol{k},t)}\mathrm{e}^{\mathrm{i}\int^t \mathrm{d}t'\left[\xi_\alpha(\boldsymbol{k},t')-\xi_\beta(\boldsymbol{k},t')\right]}\,, \tag{2.96c}$$

assuming that the system is initially in an eigenstate β of the unperturbed system.

With this analogy to adiabatic evolution Equation 2.92 can be interpreted in the following way: $\frac{\mathrm{d}\eta}{\mathrm{d}t}\hat{G}^{tt'}_{\alpha\beta}$ describes the coupling between different Floquet replicas and ξ_α represents a phase acquisition due to the quasi-energy of each coefficient. If the latter dominates, the system evolves "adiabatically" in the Floquet states. In the opposite case, $\frac{\mathrm{d}\eta}{\mathrm{d}t}G^{tt'}_{\alpha\beta}$ leads to nonadiabatic transitions between sidebands, which is proportional to the change of the slow time scale $\frac{\mathrm{d}\eta}{\mathrm{d}t}$.

Coherent suppression of high harmonics

3

Figure 3.1 illustrates a surprising phenomenon in the high-harmonic response of a light-driven Dirac material. Despite strong intra- and interband currents, the total emitted signal is drastically suppressed. This *coherent suppression* (CS) arises from destructive interference between intra- and interband contributions and is a consequence of a nontrivial interplay between tunneling, strong-field dynamics, and quantum coherence.

In this chapter we study CS using the SBE for a class of gapped Dirac materials and related two-dimensional systems.

In Section 3.1 we introduce two toy models covering a large class of materials ranging from topological insulator surface states to two-dimensional materials, which serve as platform to study CS.

3.1 Two theoretical toy models 40
3.2 Coherent suppression and the suppression ratio 45
3.3 Contributions throughout the Brillouin zone . . 51
3.4 Physical mechanism of coherent suppression 56
3.5 Re-entrant high harmonics 64
3.6 Conclusions and outlook 68

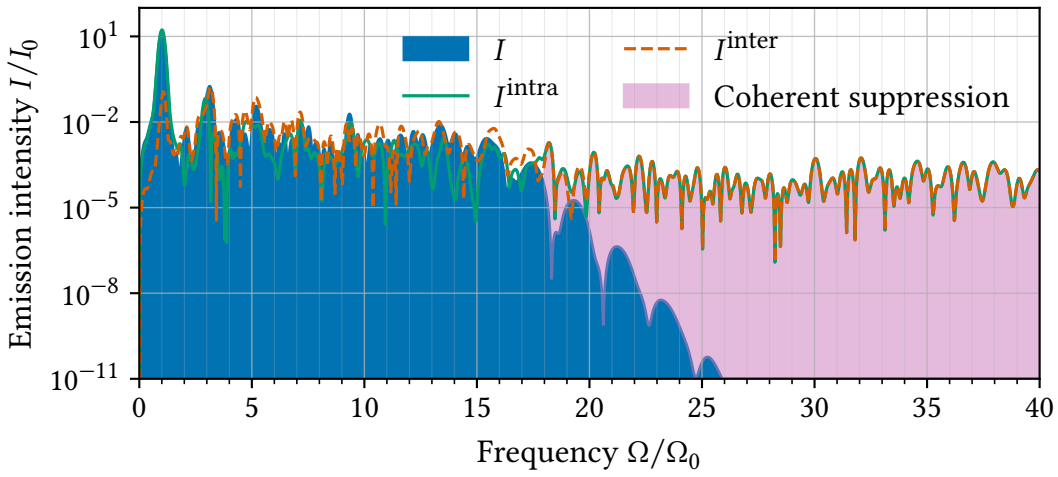


Figure 3.1: Spectral emission intensity (solid blue) from Equation 2.54 for the driven massive Dirac model (introduced in Section 3.1) decomposed into intra- (green line) and interband (dashed orange line) contributions (see Equation 3.13). Vanishing dephasing ($\tau_2 \to \infty$), a strong-field parameter of $\zeta = 10$, multi-photon number $M = 0.1$ (defined in Equation 3.8 and Equation 3.7) were used for the simulation. The spectrum shows strong *coherent suppression*: destructive interference of inter- and intraband contributions to HHG lead to a reduced total current (marked in pink).

We quantify CS by introducing a suitable figure of merit in Section 3.2 and use it to explore CS in the parameter space of the two systems. Section 3.3 shows how different parts of the Brillouin zone contribute to CS and reveals the multi-scale nature of the problem: separate regions of the BZ behave qualitatively different.

Section 3.4 discusses the physical mechanism of CS. At this point we introduce an asymptotic approximation, which leads to a concise analytical description of the mechanism behind CS. We also think the analytics are relevant beyond this work, because they represent a new analytical tool for small-gap systems in general.

In Section 3.5 we analyze how CS is lifted in the presence of dephasing, giving rise to a re-entrant regime of high-harmonic emission. A combination of numerical simulations and analytical insight in reduced-dimensional models reveals how the spectral phase relationship between intra- and interband currents controls the emission strength.

Together, these results shed light on the role of coherence and band structure in shaping high-harmonic emission from quantum materials. The research presented here additionally positions HHG as a sensitive probe of interference effects in driven two-dimensional systems and shows it may provide a way to understand phenomenological dephasing as typically included in the SBE. The bulk of this chapter is adapted from [2] with some additional analytical results and data for longer pulse durations.

3.1 Two theoretical toy models

The phenomenon of coherent suppression is investigated here for two Hamiltonians with a single valence and conduction band. The first model is a massive Dirac model with a linear dispersion and the second model hosts quadratic bands like e.g. bilayer graphene. Both Hamiltonians are low-energy approximations as described in Section 2.5, i.e. for energies around the Fermi-level. We drive both with the same external field,

$$\boldsymbol{E}(t) = -\frac{\partial \boldsymbol{A}}{\partial t}, \quad \boldsymbol{A}(t) = \frac{E_0}{\Omega_0}\boldsymbol{e}_x \cos(\Omega_0 t)\mathrm{e}^{-t^2/2\Delta t^2}, \tag{3.1}$$

where $\boldsymbol{E}$ denotes the electric field and $\boldsymbol{A}$ the vector potential (velocity gauge) in dipole approximation (see Section 2.2). Equation 3.1 describes a pulse with Gaussian envelope of standard deviation Δt linearly polarized

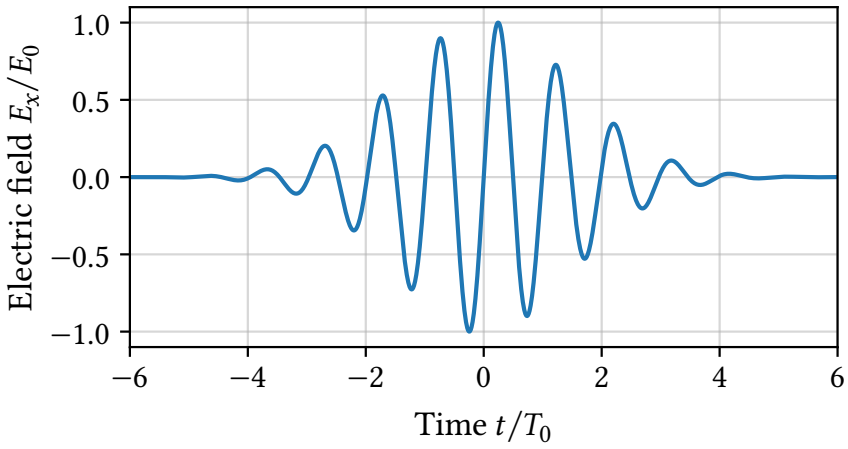


Figure 3.2: The electric field in terms of peak field strength E_0 as it depends on time measured in laser-cycles $T_0 = 2\pi/\Omega_0$. The standard deviation $\Delta t = 1.5T_0$ is used throughout this chapter.

along the x-direction with central (angular) frequency Ω_0. Figure 3.2 shows the electric field for $\Delta t = 1.5T_0$, which is used throughout this chapter. Following Section 2.4 we let the driving field dictate the time scale,

$$t_c = \frac{T_0}{2\pi} = \frac{1}{\Omega_0} \quad \Rightarrow \quad \tau = \Omega_0\, t \tag{3.2}$$

and the length scale*,

$$l_c = \frac{\Omega_0}{E_0}\,, \tag{3.3}$$

in the following. As a result the scaled vector potential reads

$$\boldsymbol{a}(\tau) = \boldsymbol{e}_x \cos(\tau) \mathrm{e}^{-\tau^2/2\sigma^2} \tag{3.4}$$

with $\sigma = \Delta t/t_c$. Note that the dimensionless vector potential conveniently satisfies $|\boldsymbol{a}(\tau)| \leq 1$ and that the laser period in scaled time is $\tau_0 = T_0/t_c = 2\pi$.

Now we consider the massive Dirac Hamiltonian in atomic units,

$$\hat{\mathscr{H}}_{\mathrm{Dirac}}(\boldsymbol{k}) = v_{\mathrm{F}}\big(k_x\hat{\sigma}_x + k_y\hat{\sigma}_y\big) + \frac{E_{\mathrm{gap}}}{2}\hat{\sigma}_z\,, \tag{3.5}$$

with the Fermi-velocity v_{F} and band gap E_{gap} at $\boldsymbol{\kappa} = 0$. The model Hamilto-

* Recall that atomic units are used for physical quantities unless indicated otherwise. In SI units, we have $l_c = \hbar\Omega_0/E_0$.

nian given in Equation 3.5 is qualitatively applicable to several solid-state materials. For small or vanishing E_{gap} it describes graphene [159] and certain topological insulator surface states, e.g. of the Bi_2Te_3-family [127], which demonstrated HHG experimentally [36, 64, 160]. For large E_{gap} it comes closer to semiconductors, albeit the dipoles match only qualitatively[†] [39, 41, 42].

Through nondimensionalization (see Section 2.4) we obtain the dimensionless/scaled Hamiltonian,

$$\hat{H}_{\mathrm{Dirac}}(\boldsymbol{\kappa}) = \frac{\zeta}{2}\left(\kappa_x\hat{\sigma}_x + \kappa_y\hat{\sigma}_y\right) + \frac{M}{2}\hat{\sigma}_z\,, \tag{3.6}$$

whereby two numbers characterizing the qualitative time-dynamics emerged naturally: the multi-photon number,

$$M = \frac{E_{\mathrm{gap}}}{\Omega_0}\,, \tag{3.7}$$

and the strong-field parameter,

$$\zeta = \frac{2v_{\mathrm{F}}\,E_0}{\Omega_0^2}, \tag{3.8}$$

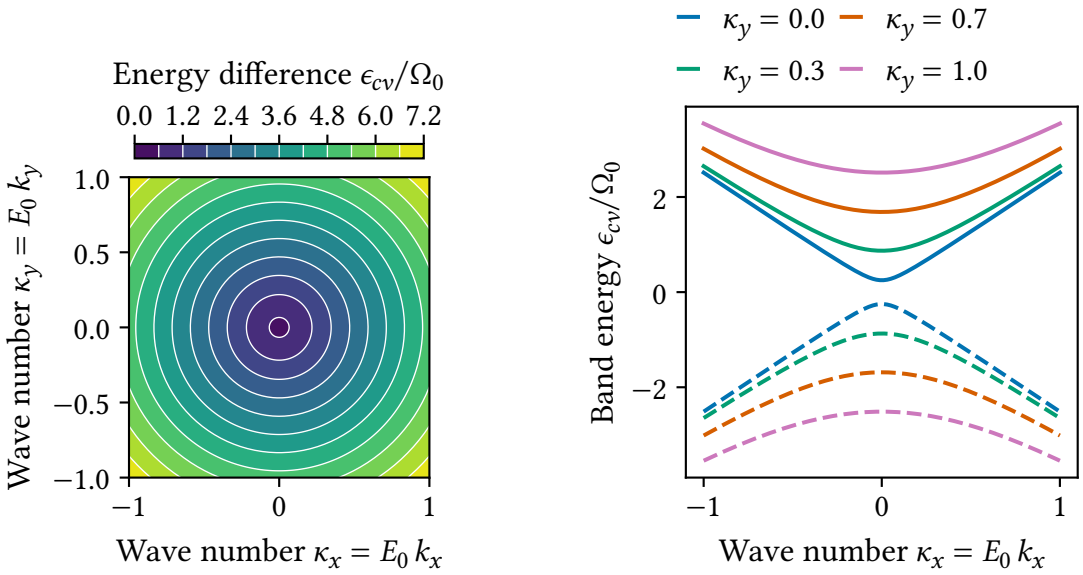
which is a generalization of the resonant adiabaticity parameter known in literature [97, 161]. For the special case of resonant ($M = 1$) driving, ζ is equivalent to the (resonant) adiabaticity parameter presented in [97], which can be interpreted as the ratio of laser cycle over transition time[‡]. For the massive Dirac model considered here, the term *adiabaticity parameter* is misleading. How adiabatic the system behaves depends strongly on the wavevector $\boldsymbol{\kappa}$ [98]. Additionally, we note that these dimensionless numbers are related to the Keldysh parameter (see [97, 140, 161, 162]),

$$\gamma_K = \frac{M}{\zeta}\,, \tag{3.9}$$

which qualitatively separates strong- ($\gamma_K \ll 1$) from weak-field regime ($\gamma_K \gg 1$). The connection to the Keldysh parameter motivates our nomenclature of "strong-field parameter" for ζ. The physical interpretation of the multi-photon number M, on the other hand, is clear: it measures how

[†] We note that in some cases (cf. [39]) the dipoles are even approximated as constants, still yielding valuable results.

[‡] Transition time refers to the transition between instantaneous eigenstates, which translates to bands in the the context of this thesis.



(a) Contours of energy difference of valence and conduction band in reciprocal space $\boldsymbol{\kappa} = (\kappa_x, \kappa_y)$.

(b) One-dimensional slices of band energy in κ_x-direction for different fixed κ_y (color-coded). Solid (dashed) lines show conduction (valence) band energy.

Figure 3.3: Bandstructure for the (scaled) massive Dirac model (see Equation 3.5) for $\zeta = 5$ and $M = 0.5$. Clearly visible in panel (b) is the change from a linear dispersion with small gap to a more quadratic behavior (for $\kappa_x \in [-1, 1]$) with increasing κ_y.

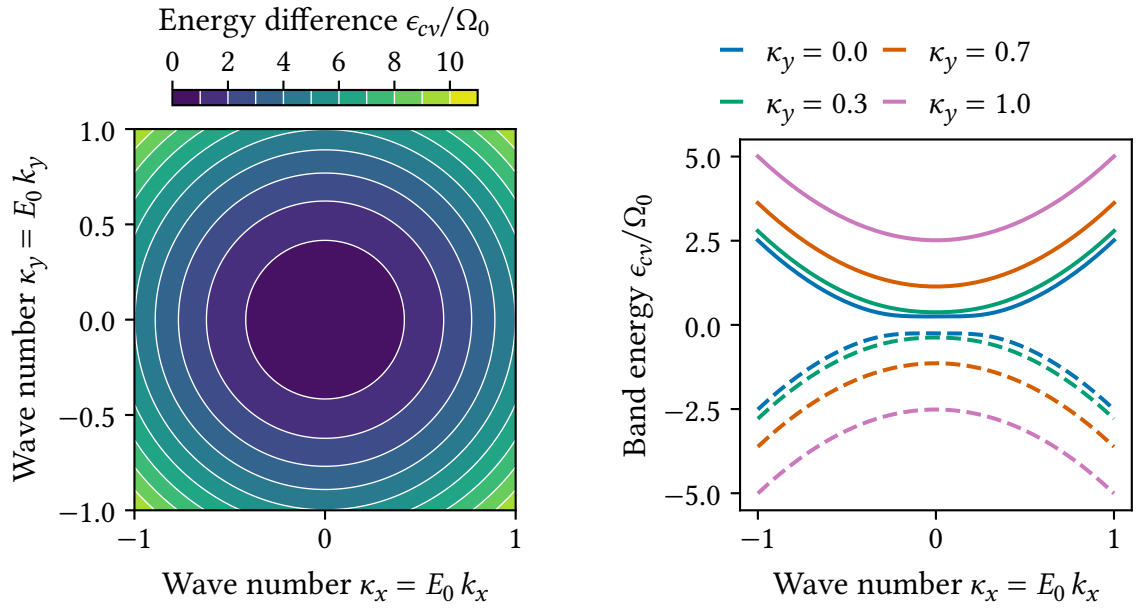
many photons fit into the minimum band-gap.

The band structure of the massive Dirac model is shown in Figure 3.3. Contours of the energy difference between the conduction and valence bands are presented in Figure 3.3a, demonstrating rotational symmetry with respect to the momentum $\boldsymbol{\kappa}$. In Figure 3.3b, one-dimensional cuts of the band structure along the κ_x direction are shown for several fixed values of κ_y. These slices highlight the crossover from linear to quadratic behavior in κ_x near the origin $\boldsymbol{\kappa} = 0$. For large wave vectors $|\boldsymbol{\kappa}|$, the dispersion asymptotically approaches a linear form.

The second Hamiltonian of interest is a toy model for bilayer graphene,

$$\hat{\mathscr{H}}_{\mathrm{BLG}} = \frac{1}{2m}\left[\left(k_y^2 - k_x^2\right)\hat{\sigma}_x - 2\,k_x k_y \hat{\sigma}_y\right] + \frac{E_{\mathrm{gap}}}{2}\hat{\sigma}_z\,, \tag{3.10}$$

which is motivated by the low-energy description near the K points of the Brillouin zone [163, 164]. The Hamiltonian $\hat{\mathscr{H}}_{\mathrm{BLG}}$ is given in atomic units, with effective mass m and a momentum-independent band gap E_{gap} at $\boldsymbol{\kappa} = 0$. This model describes massive chiral electrons and, besides serving as a minimal description of an experimentally relevant system, allows us



(a) Contours of energy difference of valence and conduction band in reciprocal space $\boldsymbol{\kappa} = (\kappa_x, \kappa_y)$.

(b) One-dimensional slices of band energy in κ_x-direction for different fixed κ_y. Solid (dashed) lines show conduction (valence) band energy.

Figure 3.4: Bandstructure for the (scaled) BLG toy model (see Equation 3.11) for $\zeta = 5$ and $M = 0.5$. The quadratic behavior is clearly visible in (b), solely around $\boldsymbol{\kappa} = 0$ the dispersion acquires a dominant fourth order component in $\boldsymbol{\kappa}$.

to investigate how the shape of the band structure influences coherent suppression.

Upon nondimensionalization, Equation 3.10 takes the scaled form

$$\hat{H}_{\mathrm{BLG}} = \frac{\zeta_{\mathrm{BLG}}}{2}\left[\left(\kappa_y^2 - \kappa_x^2\right)\hat{\sigma}_x - 2\,\kappa_x\kappa_y\hat{\sigma}_y\right] + \frac{M}{2}\hat{\sigma}_z\,, \tag{3.11}$$

with the strong-field parameter,

$$\zeta_{\mathrm{BLG}} = \frac{E_0^2}{m\Omega_0^3}\,, \tag{3.12}$$

and the multi-photon number $M = E_{\mathrm{gap}}/\Omega_0$, which coincides exactly with the definition used for the massive Dirac model.

The band structure of the bilayer graphene toy model is shown in Figure 3.4. The left panel displays contours of the energy difference between conduction and valence bands, exhibiting rotational symmetry about $\boldsymbol{\kappa} = 0$ and pronounced nonlinear dispersion. In Figure 3.4b, we present cuts along the κ_x direction for different values of κ_y. These slices emphasize the

quartic dispersion near $\boldsymbol{\kappa} = 0$, which crosses over to quadratic behavior in κ_x for larger κ_y.

3.2 Coherent suppression and the suppression ratio

In this section, we introduce the phenomenon of coherent suppression (CS) and define a suitable measure to quantify its occurrence and strength. We employ the SBE in the form given in Section 2.4 to simulate the response of the two models introduced in the preceding section to the driving pulse shown in Figure 3.2; see Equations 3.5, 3.10 and 3.11. At times preceding the pulse, $t \to -\infty$, the system is prepared in its ground state as specified by Equation 2.31. Throughout the remainder of this chapter, we set $\epsilon_\mathrm{F} = 0$ and $T = 0$, such that the Fermi level lies in the middle of the band gap and the valence band is initially fully occupied while the conduction band is empty.

The observable of interest here is the emission intensity of radiation (see Equation 2.41 and Equation 2.54), which can be expressed in terms of intra- and interband contributions (Equation 2.52),

$$I(\omega) = I^\mathrm{inter}(\omega) + I^\mathrm{intra}(\omega) + 2\sqrt{I^\mathrm{intra}(\omega)\, I^\mathrm{inter}(\omega)}\, \cos\phi \quad \text{with} \tag{3.13}$$

$$I^\mathrm{intra/inter}(\omega) = \omega^2 \left| \boldsymbol{j}_\mathrm{intra/inter}(\omega) \right|^2 . \tag{3.14}$$

Figure 3.5, panel (f) shows the effect we dubbed CS calculated for the massive Dirac model from Equation 3.6 with $\zeta = 10$ and $M = 0.1$ for vanishing dephasing (or $\tau_2 \to \infty$). For large emission frequencies beyond the HHG plateau I^inter and I^intra remain roughly constant over a large range ω, whereas the total emission quickly decays. Evidently, destructive interference of $\boldsymbol{j}_\mathrm{inter}(\omega)$ and $\boldsymbol{j}_\mathrm{intra}(\omega)$ is occurring. Similar observations were made in other studies [45, 46] for massive and massless Dirac models with one proposed explanation being the linear dispersion relation of their band energies. We provide a counter-example in the following by studying the response of the BLG model with non-linear dispersion.

In the following we take advantage of the relatively small number of model parameters of Equation 3.6 and Equation 3.11 to conduct a large-scale numerical exploration study. To this end a driving field of *fixed shape* (see Equation 3.4 and Figure 3.2) is employed, i.e. the duration in terms of laser

cycles τ_0 is held constant at $\sigma = 1.5\,\tau_0$. Additionally, we focus on perfectly coherent ($T_2 \to \infty$) dynamics; the influence of finite dephasing times is studied in Section 3.5. This restriction together with the fixed driving field reduces the parameter space of the Dirac (BLG) system introduced above to two dimensions, spanned by the multi-photon number M and ζ (ζ_{BLG}). We performed simulations for $9 \times 9 = 81$ different points in parameter space for the massive Dirac model on a two-dimensional grid with logarithmic spacing,

$$(\zeta, M) \in \left[10^{-1}, 10^{-0.75}, \ldots, 10^{1}\right] \times \left[10^{-1}, 10^{-0.75}, \ldots, 10^{1}\right] \tag{3.15}$$

$$\approx \left[0.1, 0.18, 0.32, 0.56, 1, 1.8, 3.2, 5.6, 10\right]^2 . \tag{3.16}$$

We note that each point was individually tested for convergence (length of time steps, initial time, $\boldsymbol{k}$-grid density and BZ size).

Figure 3.5 shows the emitted intensities for six different points within this grid for the massive Dirac model, demonstrating the qualitative dependence of the emission spectra on ζ and M. In panels (a), (c), and (e) the strong-field parameter ζ is held fixed while changing M and only one spectrum with small multi-photon number, $M = 0.18$, shows CS On the other hand whereas for $M > 1$ the interband contribution becomes dominant, see panels (b) and (c) of Figure 3.5.

Figure 3.5, panels (b), (d), and (f) depict data for varying strong-field parameters with fixed multi-photon number $M = 0.18$. Here, all spectra exhibit CS and larger ζ lead to a higher cutoff of HHG. Additionally, we see slower decay of inter- and intraband contributions with increasing strong-field parameter. A dashed purple line marks the frequency with emitted photon energy of the minimal band-gap. This line reveals why the total intensity—dominated by interband emission here—is non-monotonic with respect to frequency in panel (e) of Figure 3.5: there is a resonance at the band gap.

This small sample already shows the richness and complexity in the HHG spectra resulting from a seemingly simple two-band system. We will elaborate some of these aspects in the following sections, like the HHG cutoff and resonances, but first let us focus on CS. The data presented clearly suggests the multi-photon parameter as the primary determining factor for the latter.

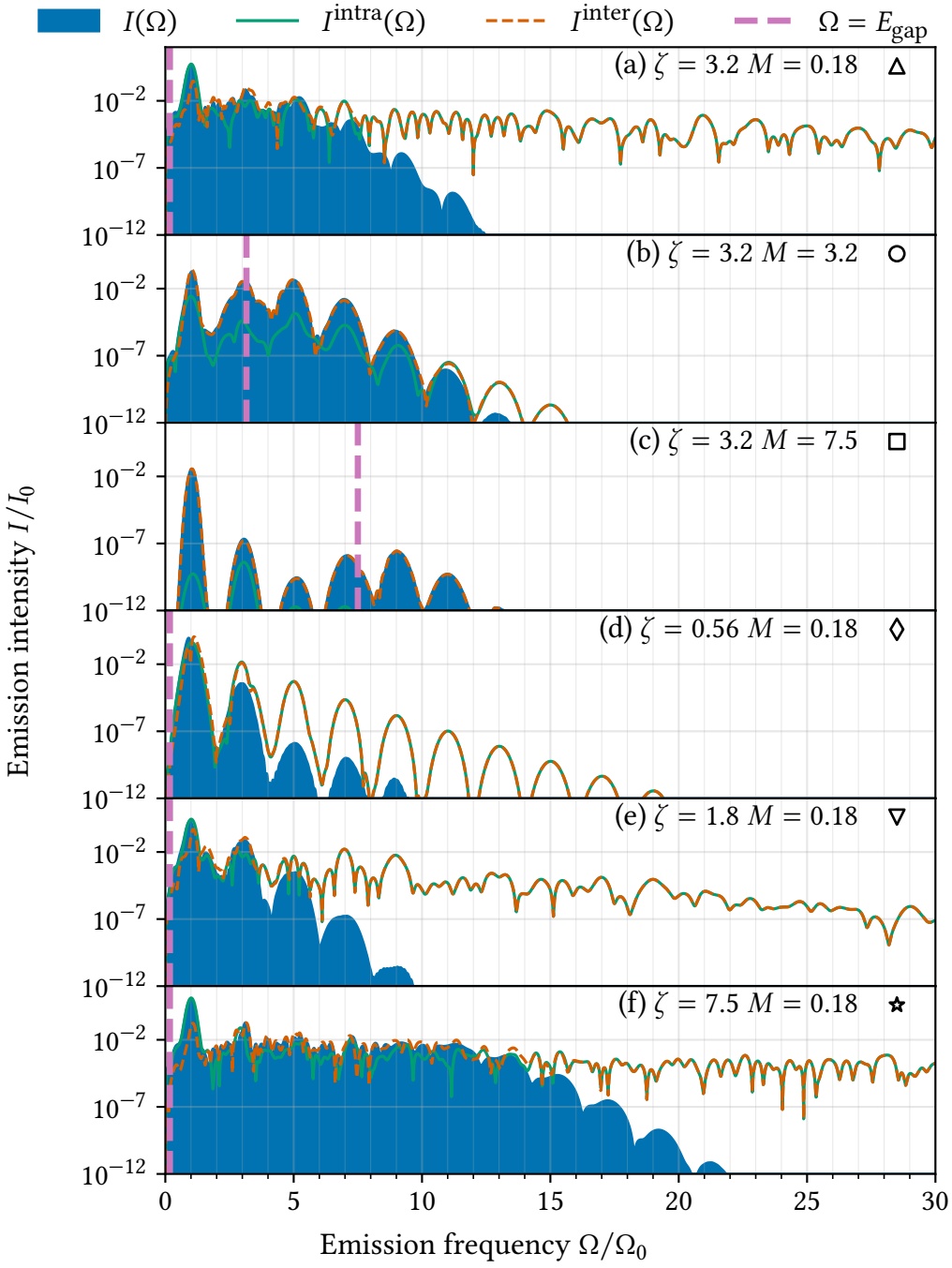


Figure 3.5: Total frequency-resolved emission intensity $I(\omega) = I(\Omega/\Omega_0)$ (Equation 2.54), shaded blue) compared to intraband (solid green line) and interband (dashed orange line) contributions according to Equation 3.13 for different multi-photon numbers, M, and strong-field parameters, ζ. Here, we drive a massive Dirac model, (Equation 3.6), without dephasing ($\tau_2 \to \infty$) by the driving field given in Equation 3.4 with $\sigma = 1.5\,\tau_0$. Panels (a)-(c) depict results for various multi-photon numbers M at $\zeta = 3.2$, showing the transition from CS to interband dominated emission. Panels (d)-(f) show intensities with different strong-field parameters ζ for $M = 0.18$, demonstrating CS over a wide range of ζ. Markers refer to parameter space positions in Figure 3.6 and the dashed purple lines show the frequency with emitted energy corresponding to the band-gap E_{gap}. For a driving frequency of $\Omega_0/2\pi = 10\,\text{THz}$, the multi-photon numbers $M \in \{0.18, 3.2, 7.5\}$ correspond to band gaps of $\Delta \in \{7.5\,\text{meV}, 130\,\text{meV}, 310\,\text{meV}\}$. At a Fermi velocity of $v_F = 5.0 \times 10^5\,\text{m/s}$, strong-field parameters $\zeta \in \{0.56, 3.2, 7.5\}$ correspond to peak field strengths of $E \in \{0.015\,\text{MV/cm}, 0.083\,\text{MV/cm}, 0.19\,\text{MV/cm}\}$. Figure adapted from [2].

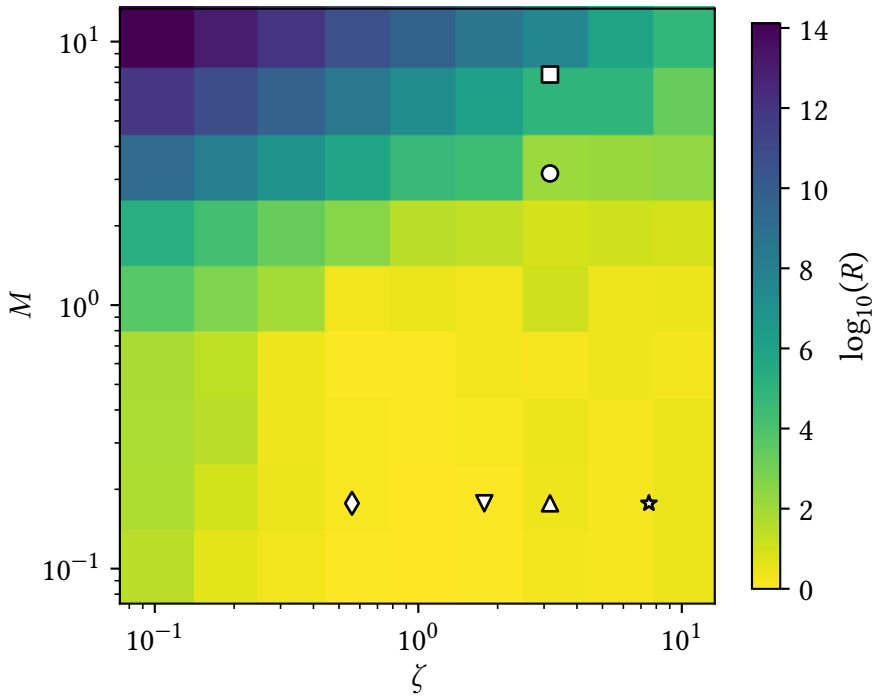


Figure 3.6: Suppression ratio R from Equation 3.17 for the massive Dirac model with driving field given in Equation 3.4 and $\sigma = 1.5\,\tau_0$ for different multi-photon numbers M and strong-field parameters ζ. Spectral instensity with inter- and intraband decompositions for parameters at the markers are shown in Figure 3.5. For a driving frequency of $\Omega_0/2\pi = 10\,\mathrm{THz}$, the multi-photon numbers $M \in [0.1, 10]$ correspond to band gaps in the range of $\Delta \in [4.2\,\mathrm{meV}, 420\,\mathrm{meV}]$. At that frequency and with a Fermi velocity of $v_F = 5.0 \times 10^5\,\mathrm{m/s}$, strong-field parameters $\zeta \in [0.1, 10]$ correspond to peak field strengths of within $E \in [2.6 \times 10^{-3}\,\mathrm{MV/cm}, 0.26\,\mathrm{MV/cm}]$. Figure adapted from [2].

In order to verify this hypothesis we introduce the *suppression ratio*,

$$R = \left\langle I^{\mathrm{inter}} / I^{\mathrm{intra}} \right\rangle_{\omega} , \tag{3.17}$$

where the average $\langle \ldots \rangle_{\omega}$ includes all frequencies above the (numerical) noise threshold (see Appendix D). Evidently, the suppression ratio is close to unity when the interband and intraband intensities coincide, and it is smaller (larger) than one when the intraband (interband) contribution dominates. In general, a suppression ratio close to one does not necessarily imply destructive interference between the two contributions. For the data presented here, however, no constructive interference is observed. A numerical confirmation of this statement based on a second figure of merit is provided in Appendix B. Under the additional restriction that only destructive interference occurs within the considered parameter range, the suppression ratio R defined in Equation 3.17 therefore allows for a qualitative identification of coherent suppression using a single scalar quantity. In a nutshell, bright color in Figure 3.6 corresponds to coherent

suppression.

Figure 3.6 shows a heatmap of R across the parameter space introduced above and largely confirms that the multi-photon number M is the *primary parameter enabling coherent suppression.*

However, there is some additional variation of R with the stron-field parameter ζ visible in Figure 3.6, which we dicsuss in the following. For $M \ll 1$, the suppression ratio decreases with increasing ζ, an effect that can be attributed to numerical resolution and to the definition of R. Smaller values of ζ lead to a more rapid decay of both I_{inter} and I_{intra} with increasing harmonic order (cf. Figure 3.5a and d), such that fewer harmonics contribute to the frequency average $\langle \cdots \rangle_\omega$. When only a small number of harmonics is included, disproportionate weight is placed on the lowest orders, where interband and intraband contributions differ most strongly, thereby increasing R.

Additional insight can be gained from Figure 3.6. First, for large multi-photon numbers M, the total emission intensity is dominated by the interband contribution. Second, the suppression ratio never falls below unity, indicating that throughout the entire parameter space considered, interband emission remains comparable to and cannot be neglected with respect to intraband emission.

We now consider the second model introduced in Section 3.1—a toy model of bilayer graphene (BLG), see Equation 3.11. Besides its experimental relevance, this system is an ideal candidate to investigate the influence of band dispersion shape on coherent suppression. We employ the same field as the Dirac case (cf. Equation 3.4) and also turn off dephasing ($\tau_2 \to \infty$) for better comparison of the two systems. The same footprints of CS are visible in panels(b), (b), and (d) of Figure 3.7. However, these signatures are less pronounced as compared to Figure 3.5 for similar strong-field parameters and multi-photon numbers. To be more specific, the inter- and intraband contributions do not plateau as e.g. in panels (a), (e), and (f) of Figure 3.5, but rather decay. Still, they exactly coincide and are significantly larger than the total signal, which we consider defining features of CS. We suspect that smaller multi-photon numbers M are required to achieve results more similar to the Dirac model; further exploration of the model's parameter space is necessary for clarification. More importantly, M still seems to be the deciding factor of enabling CS.

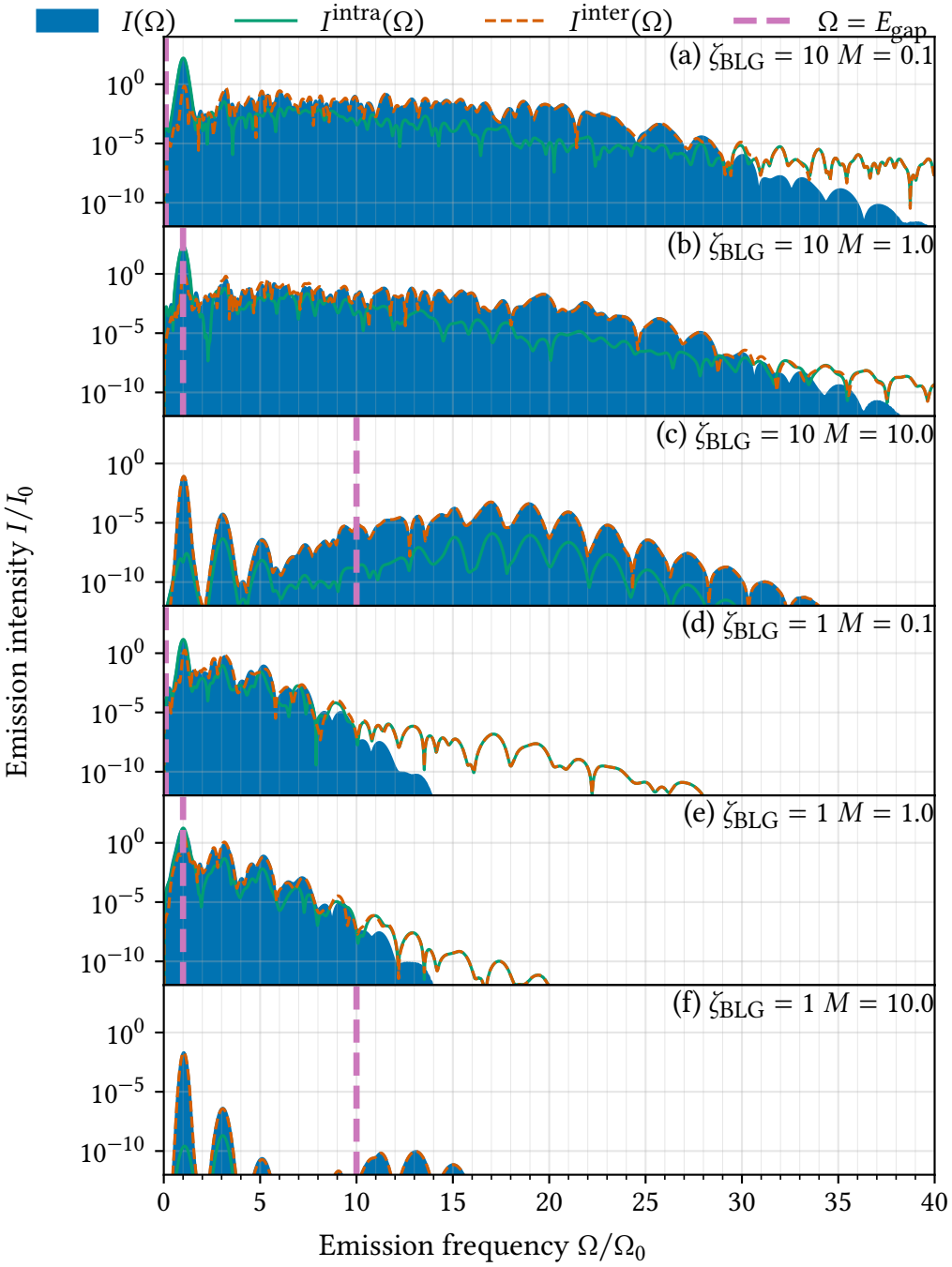


Figure 3.7: Total frequency-resolved emission intensity $I(\omega) = I(\Omega/\Omega_0)$ (Equation 2.54), shaded blue) compared to intraband (solid green line) and interband (dashed orange line) contributions according to Equation 3.13 for different multi-photon numbers, M, and strong-field parameters, ζ_{BLG}. We consider a BLG model here, (Equation 3.11), without dephasing ($\tau_2 \to \infty$) and driven by the field given in Equation 3.4 with $\sigma = 1.5\,\tau_0$. Panels (a)-(c) show results for a strong-field parameter $\zeta = 1$ and panels (d)-(f) for $\zeta = 10$ respectively. Multi-photon numbers $M \in \{0.1, 1, 10\}$ are shown. The same signatures of CS as in Figure 3.5 are present here, however slightly weaker at comparable M: the inter- and intraband contributions do not plateau as e.g. in panels (a),(e), and (f) of Figure 3.5. For a driving frequency of $\Omega_0/2\pi = 10\,\text{THz}$, the multi-photon numbers $M_{\text{BLG}} \in \{0.1, 1, 10\}$ correspond band gaps of $\Delta_{\text{BLG}} \in \{4.2\,\text{meV}, 42\,\text{meV}, 420\,\text{meV}\}$. Additionally setting the effective mass as $m = 0.032 m_e$, the strong-field parameters $\zeta \in \{1, 10\}$ correspond to field strengths of $E \in \{0.054\,\text{MV/cm}, 0.17\,\text{MV/cm}\}$. Figure adapted from [2].

Another common feature of Dirac and BLG models can be seen in Figures 3.5 and 3.7. There is a crossover from CS to interband dominance with increasing multi-photon number. In both systems the band structure and dipoles start to resemble wide-gap Semiconductor systems for large M. We hypothesize that the physics increasingly resembles the example presented in Section 2.6 as a result. The systems then behave according to the three-step model such that the interband contribution dominates and a plateaeu (with clear cutoff) emerges. We provide evidence for the semi-classical behavior of the massive Dirac model at the end of Section 3.3.

3.3 Contributions throughout the Brillouin zone

Having identified the importance of a small multi-photon number M for coherent suppression, we disentangle contributions from different regions in the BZ within this section. As a result we can employ a reduction of dimensionality for describing the physical origin of CS in Section 3.4. Consider the structure of the SBE (Section 2.4) for Dirac/BLG models: different $\boldsymbol{\kappa}$-modes can be interpreted as an ensemble of two-level systems. The wave-vector $\boldsymbol{\kappa}$ strongly influences the qualitative dynamics. Consequently, the different dynamical regimes identified in [97] at the level of a single mode at $\boldsymbol{\kappa} = 0$ can be found throughout the BZ as already pointed out by Junk [98, chapter 5]. Herein lies the multi-scale nature of coherent suppression mentioned in this chapter's opening paragraph.

To gain a physical intuition of the occupation dynamics, one can inspect the band structures shown in Figures 3.3b and 3.4b. Upon increasing $|\kappa_y|$ the charge carriers experience a larger gap[§], corresponding to an effectively larger multi-photon number. As a result a more dominant interband contribution to the emission intensity is expected for states with larger $|\kappa_y|$—consistent with Figures 3.5 and 3.7. We also expect the physics to be better described by the three-step model for larger effective gaps and HHG spectra more closely resembling the characteristic plateau structure as a consequence.

In order to verify this intuition, we consider one-dimensional slices of the

[§] This is not the "full story", dipole and current matrix elements also vary considerably with the wave vector $\boldsymbol{\kappa}$.

BZ with fixed κ_y and introduce the current densities of these subsystems,

$$j_x(\tau,\kappa_y) = j_x^{\text{intra}}(\tau,\kappa_y) + j_x^{\text{inter}}(\tau,\kappa_y) \tag{3.18}$$

$$j_x^{\text{intra}}(\tau,\kappa_y) = \int_{BZ(\tau)} \frac{\mathrm{d}\kappa_x}{2\pi} \sum_{n=1}^{N} \rho_{nn}(\boldsymbol{\kappa},\tau) j_{x,nn}(\boldsymbol{\kappa}) \tag{3.19}$$

$$j_x^{\text{inter}}(\tau,\kappa_y) = \int_{BZ(\tau)} \frac{\mathrm{d}\kappa_x}{2\pi} \sum_{\substack{m,n=1 \\ m\neq n}}^{N} \rho_{nn}(\boldsymbol{\kappa},\tau) j_{x,nn}(\boldsymbol{\kappa}) \,, \tag{3.20}$$

in terms of $j_{x,mn}(\boldsymbol{\kappa}) = \langle m\boldsymbol{\kappa}| \frac{\partial \hat{H}}{\partial \kappa_x} |n\boldsymbol{\kappa}\rangle$. Similarly we define the spectral yield,

$$S(\omega,\kappa_y) = \omega^2 \left| j_x(\omega,\kappa_y) \right|^2 = \omega^2 \left| \frac{1}{\sqrt{2\pi}} \int_{-\infty}^{\infty} \mathrm{d}\tau \, j_x(\tau,\kappa_y) \mathrm{e}^{-\mathrm{i}\omega\tau} \right|^2 \tag{3.21a}$$

$$S^{\text{inter/intra}}(\omega,\kappa_y) = I_0 \omega^2 \left| j_x^{\text{inter/intra}}(\omega,\kappa_y) \right|^2 \,, \tag{3.21b}$$

which is labeled by S in order to distinguish it from the emission intensity of the two-dimensional system.

Firstly, consider the massive Dirac model with a strong-field parameter of $\zeta = 7.5$ and a multi-photon number of $M = 0.18$, where strong CS was observed (see Figure 3.5, panel (f) and Figure 3.6). Figure 3.8, panel (d) shows the total emission intensity I_x depending on frequency ω and wavenumber κ_y. There we see a narrow dark strip around $\kappa_y = 0$, where the total intensity is strongly suppressed for $\omega/\Omega_0 > 1$ i.e. only the carrier wave frequency Ω_0 is contained in the total current response. On the other hand appreciable intensities beyond the first few harmonics are visible for $0.1 \lesssim |\kappa_y| \lesssim 1.5$. This region in the BZ is hence responsible for the plateau visible in Figure 3.5, panel (f).

Figure 3.8, panels (a)-(c) display the decomposition of the intensity in terms of inter- and intraband contributions for three exemplary values of κ_y marked by dashed white lines in panel (d) for comparison. Our expectation is confirmed, with increasing $|\kappa_y|$ the interband contribution becomes more and more dominant, such that modes further away from the BZ origin are not responsible for coherent suppression. Additionally, the 1D slice at $\kappa_y = 0$ shown in panel (b) of Figure 3.8 displays large intra- and interband emissions even far beyond the plateau of the total intensity.

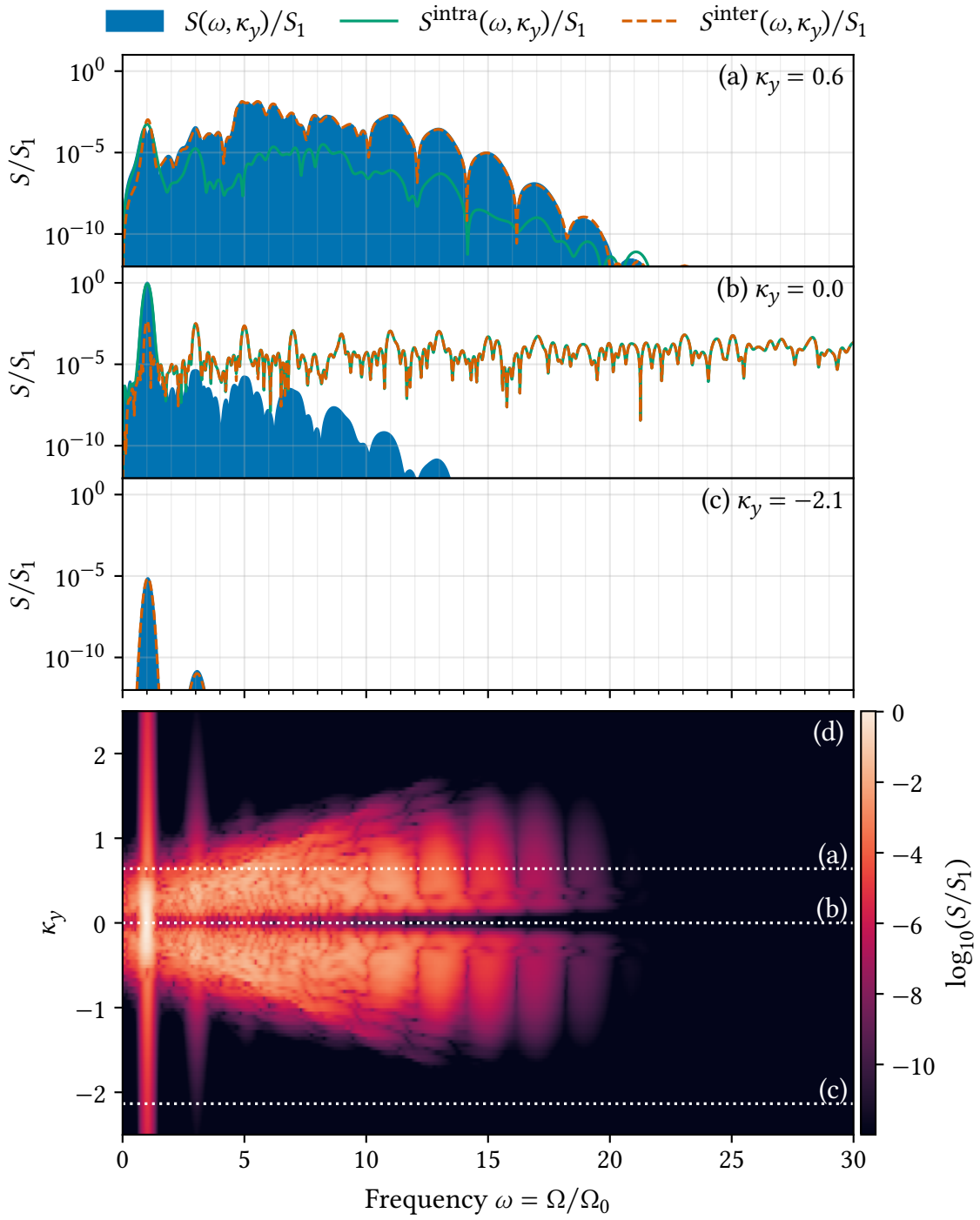


Figure 3.8: Spectral yield from several one-dimensional massive Dirac models with parameters $\zeta = 7.5$, $M = 0.18$, $\tau_2 \to \infty$, and $\sigma = 1.5\,\tau_0$ (see Equations 3.4, 3.6 and 3.21). Emission spectra are obtained from a one-dimensional Brillouin zone integral along the κ_x-direction for fixed values of κ_y (cf. Equation 3.21). The spectral yields are normalized to the weight of the principal harmonic $S_1 = S(1, 0)$ (see Equation 3.21) for $\kappa_y = 0$. Panels (a)-(c) display the decomposition of the total (shaded blue) emission into inter- (dashed orange) and intraband (solid green line) contibutions according to Equation 3.21 for $\kappa_y = 0.6$, $\kappa_y = 0$, and $\kappa_y = -1.7$. Panel (d) displays the color-coded and frequency-resolved total emission intensities for $\kappa_y \in [-4, 4]$ with dashed white lines marking the cuts shown in (a)-(c). Figure adapted from [2].

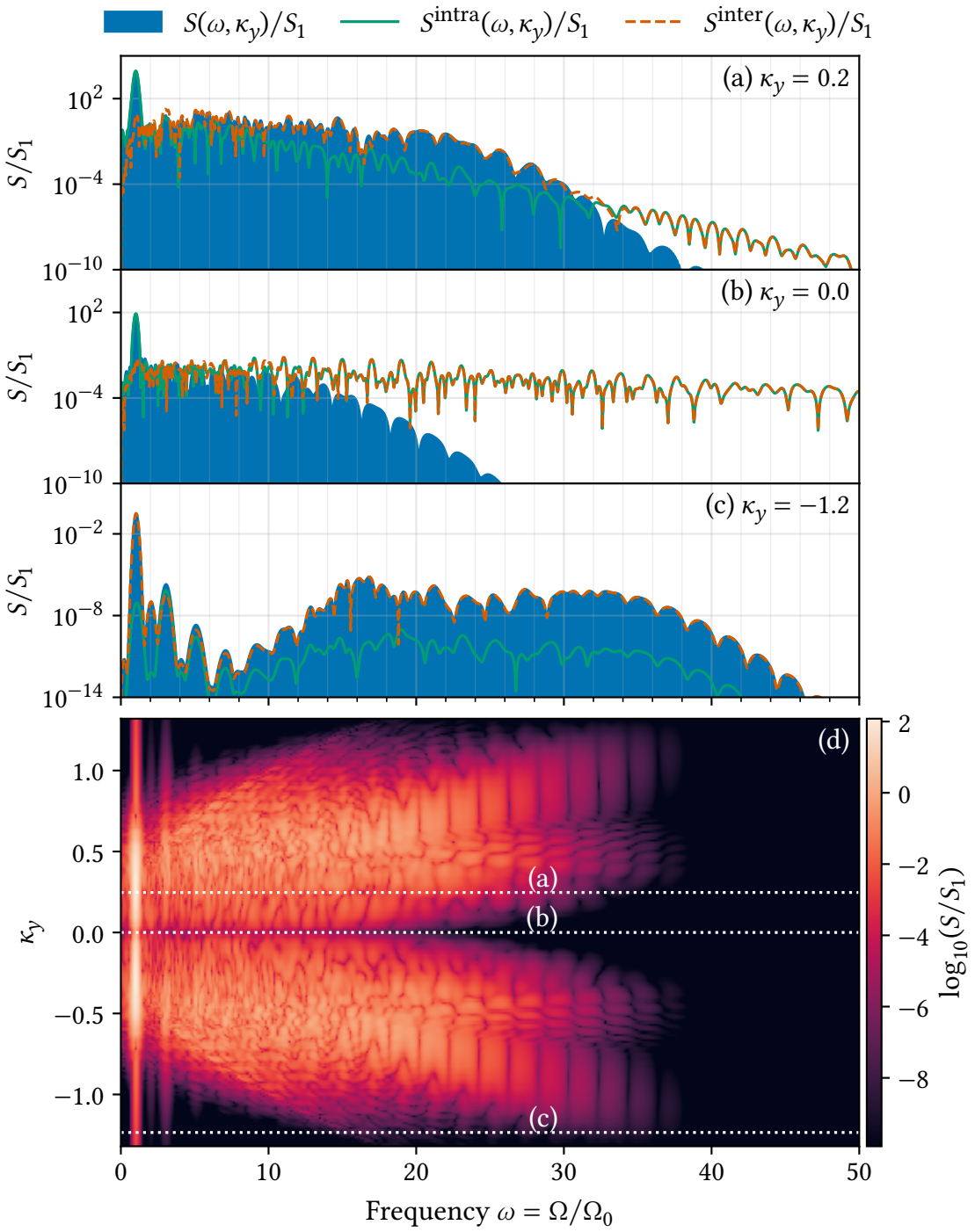


Figure 3.9: Spectral yield from several one-dimensional massive BLG models with parameters $\zeta = 10$, $M = 0.1$, $\tau_2 \to \infty$, and $\sigma = 1.5\,\tau_0$ (see Equations 3.4, 3.11 and 3.21). Emission spectra are obtained from a one-dimensional Brillouin zone integral along the κ_x-direction for fixed values of κ_y (cf. Equation 3.21). The spectral yields are normalized to the weight of the principal harmonic $S_1 = S(1, 0)$ (see Equation 3.21) for $\kappa_y = 0$. Panels (a)-(c) display the decomposition of the total (shaded blue) emission into inter- (dashed orange) and intraband (solid green line) contibutions according to Equation 3.21 for $\kappa_y = 0.2$, $\kappa_y = 0$, and $\kappa_y = -1.2$. Panel (d) displays the color-coded and frequency-resolved total emission intensities for $\kappa_y \in [-1.3, 1.3]$ with dashed white lines marking the cuts shown in (a)-(c).

In Figure 3.9 the same analysis is repeated for the BLG model (see Equation 3.11) with $\zeta_{\mathrm{BLG}} = 10$ and $M = 0.1$. These parameters again enable strong CS (cf. Figure 3.7). Overall the qualitative picture is very similar to the massive Dirac case above. Panel (d) displays a narrow strip around $\kappa_y = 0$ with a single peak at Ω_0, whereas the signal for larger frequencies in panel (a) of Figure 3.7 arise from modes outside of this strip with $|\kappa_y| \lesssim 1$. Additionally, interband emission is more dominant for increasing values of $|\kappa_y|$.

Our analysis of different regions in the Brillouin zone clearly suggests that a one-dimensional model at $\kappa_y = 0$ is sufficient to understand CS for both models presented, although not for all features of the HHG spectrum (like the plateau). Exploring the consequence of this observation is the subject of the next section.

To conclude this section, we apply the approach introduced in Section 2.6 to assess the validity of the three-step model for individual κ_y slices. Figure 3.10 compares the time-frequency profile of the interband current, obtained via a Gabor transform (see Equation 2.79), with the first- and second-order recollision trajectories predicted by the semiclassical three-step model. We employ the same approximation as in Section 2.6 and Figure 2.7, namely neglecting the imaginary part of the trajectories' birth times in the saddle-point approximation Equation 2.78. The other two saddle-point equations, Equations 2.74b and 2.74c, are then solved numerically.

While the emission *times* associated with first-order recollisions agree well with the numerical results, the corresponding emission *energies* are systematically underestimated by the semiclassical trajectories. As discussed in Section 2.6, several approximations enter the calculation of these trajectories, making it difficult to assess the relative importance of individual contributions. By comparing Figure 3.10 with Figure 2.7, we therefore conclude that the κ_y slices responsible for the plateau-like behavior observed in Figure 3.5f are not clearly within the three-step regime. Instead, the underlying dynamics appear to lie in an intermediate regime between the nearly diabatic behavior of the $\kappa_y = 0$ slice and a fully semiclassical behavior. A more detailed investigation of this crossover is left for future work; in particular, extending the analysis to the bilayer graphene model would help clarify the role of band dispersion.

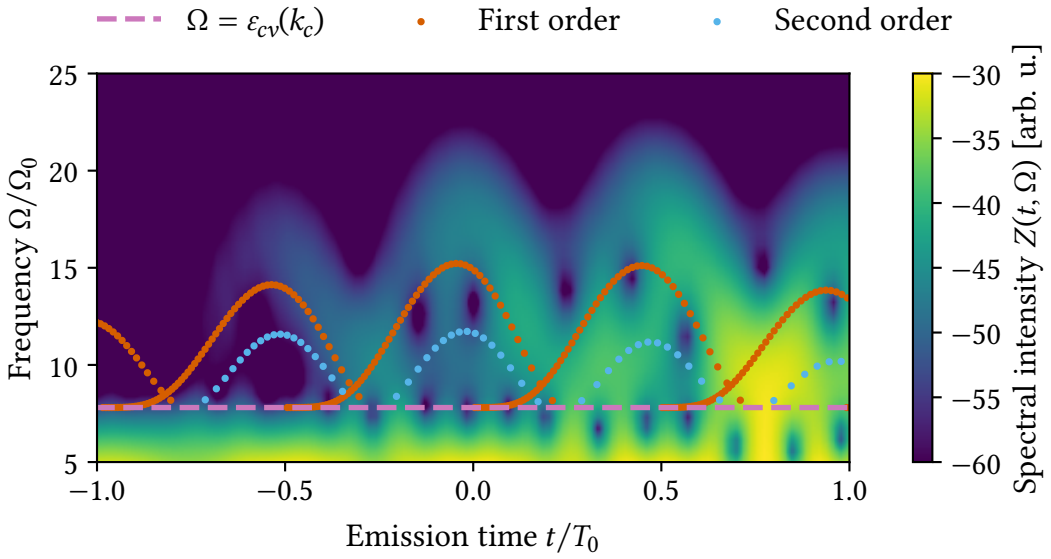


Figure 3.10: Time-frequency profiles (Equation 2.79) from a κ_y-slice at $\kappa_y = -0.78$ of the massive Dirac model for the parameters $\zeta = 10$ and $M = 0.1$. The orange (blue) lines show the first (second) order semi-classical re-collision events calculated from Equation 2.74 with the approximation given in Equation 2.78. The band gap energy at $\kappa_x = 0$ is marked by a horizontal dashed purple line.

3.4 Physical mechanism of coherent suppression

Motivated by the previous section we consider a one-dimensional restriction of Equation 3.6 for $\kappa_y = 0$,

$$\hat{H}_{\text{Dirac,1d}}(\kappa) = \frac{1}{2}(\zeta\kappa\hat{\sigma}_z + M\hat{\sigma}_x)\,. \tag{3.22}$$

We focus on the massive Dirac model, because the qualitative behavior of the BLG toy model is very similar. A unitary rotation of Equation 3.6 with $\hat{U} = \frac{1}{\sqrt{2}}\left(\begin{smallmatrix} 1 & 1 \\ 1 & -1 \end{smallmatrix}\right)$ leads to Equation 3.22 with the definition $\kappa = \kappa_x$ introduced for brevity. We are interested in an approximation of the SBE solutions for small M and $\tau_2 \to \infty$ to describe CS. In the absence of dephasing the SBE are equivalent to the time-dependent Schrödinger equation, which has trivial analytic solutions for $M = 0$,

$$\begin{aligned} \mathrm{i}\frac{\partial}{\partial\tau}\,|\psi(\kappa,\tau)\rangle &= \frac{\zeta}{2}[\kappa - a(\tau)]\hat{\sigma}_z\,|\psi(\kappa,\tau)\rangle \\ \Rightarrow\quad |\psi_\pm(\kappa,\tau)\rangle &= \mathrm{e}^{\mp\frac{\mathrm{i}}{2}\zeta\int^\tau \mathrm{d}\tau'[\kappa - a(\tau')]}\,|\pm\rangle\ , \end{aligned} \tag{3.23}$$

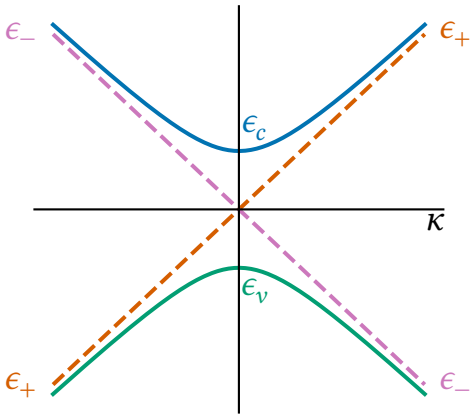


Figure 3.11: Schematic sketch of the adiabatic energies $\epsilon_{c/v}$ (band structure) and the diabatic energies $\epsilon_{\pm}$.

with the Pauli matrix eigenstates $\hat{\sigma}_z |\pm\rangle = \pm |\pm\rangle$ and $a(\tau) = a_x(\tau)$ (see Equation 3.4). Figure 3.11 shows a schematic of the instantaneous eigenenergies compared to the diabatic energies $\epsilon_{\pm} = \langle\pm| \hat{H}_{\text{Dirac,1d}} |\pm\rangle$. This avoided crossing scenario is analogous to the two-level system discussed in Section 2.1, however we are dealing with a continuous ensemble parametrized by κ. The exact solutions for $M = 0$ are proportional to the diabatic states introduced in Section 2.1, so for small M the system should be in the diabatic regime shown in Figure 2.2, panel (b). Note that these solutions transform to non-continuous jumps in the occupations upon changing to the co-moving (adiabatic) Houston basis—just as described in Section 2.1. If the system behaves diabatically, the adiabatic basis is a poor choice as a starting point for an analytical solution and we consequently choose the *diabatic basis* $|\pm\rangle$ in order to expand around the exact solutions for $M = 0$. Physically, the diabatic states describe left- and right-movers, which can be easily seen by applying the velocity operator to $|\pm\rangle$.

Rather than working with the equations of motion for the density matrix-elements $\rho_{\pm\pm}(\kappa, \tau) = \langle\pm| \hat{\rho}(\kappa, \tau) |\pm\rangle$ directly, we introduce the occupation imbalance,

$$\delta(\kappa, \tau) = \frac{1}{2}[\rho_{++}(\kappa, \tau) - \rho_{--}(\kappa, \tau)] \,, \tag{3.24}$$

and the coherence,

$$\eta(\kappa, \tau) = \rho_{+-}(\kappa, \tau) \,, \tag{3.25}$$

which are sufficient to determine the density matrix fully. The equations

of motion,

$$\frac{\partial \eta}{\partial \tau} = -\mathrm{i}\zeta[\kappa - a(t)]\eta(\kappa,\tau) + \mathrm{i}M\delta(\kappa,\tau)\,, \tag{3.26a}$$

$$\frac{\partial \delta}{\partial \tau} = -2M\,\mathrm{Im}[\eta(\kappa,\tau)]\,, \tag{3.26b}$$

decouple for $M = 0$ thanks to the unitary rotation. The initial condition of a filled valence band (see Equation 2.31),

$$\eta(\kappa,\tau\to-\infty) = \frac{-M}{2\sqrt{\zeta^2\kappa^2+M^2}} \quad \text{and} \tag{3.27a}$$

$$\delta(\kappa,\tau\to-\infty) = \frac{-\zeta\kappa}{2\sqrt{\zeta^2\kappa^2+M^2}}\,, \tag{3.27b}$$

reveals a technical difficulty for standard time-dependent perturbation theory in M: the initial states are themselves dependent on M. While it is possible to expand the initial condition, we propose an alternative that leverages our precise analytic knowledge of its M-dependency. We seek an asymptotic expansion of Equation 3.26 of the form

$$\eta(\kappa,\tau) \sim \frac{1}{2\sqrt{\zeta^2\kappa^2+M^2}}\big[\eta_0(\kappa,\tau) + M\eta_1(\kappa,\tau) + M^2\eta_2(\kappa,\tau) + \cdots\big] \tag{3.28a}$$

$$\delta(\kappa,\tau) \sim \frac{1}{2\sqrt{\zeta^2\kappa^2+M^2}}\big[\delta_0(\kappa,\tau) + M\delta_1(\kappa,\tau) + M^2\delta_2(\kappa,\tau) + \cdots\big]\,, \tag{3.28b}$$

which allows exact matching of Equation 3.27 while still being well-ordered[¶] in M. We demand the expansion functions in Equation 3.28 to satisfy Equation 3.27, yielding matching conditions,

$$\delta_n(\kappa,\tau\to-\infty) = \begin{cases} -\zeta\kappa & \text{if } n = 0 \\ 0 & \text{otherwise} \end{cases} \tag{3.29a}$$

$$\eta_n(\kappa,\tau\to-\infty) = \begin{cases} -1 & \text{if } n = 1 \\ 0 & \text{otherwise.} \end{cases} \tag{3.29b}$$

[¶] By well-ordered we mean that for an asymptotic expansion $f(\epsilon,x) \sim f_0(x)g_0(\epsilon) + f_1(x)g_1(\epsilon) + \cdots$ it holds that $g_{n+1} = o(g_n)$ as $\epsilon \to \epsilon_0$ (see e.g. [93, 125]).

The formal solution of Equations 3.28 and 3.29,

$$\delta_0(\kappa,\tau) = -\zeta\kappa, \quad \delta_1(\kappa,\tau) = \eta_0(\tau) = 0\,, \tag{3.30a}$$

$$\eta_1(\kappa,\tau) = -e^{-i\phi(\kappa,\tau)}\left[1 + 2i\zeta\kappa\int_{-\infty}^{\tau} \mathrm{d}\tau' e^{i\phi(\kappa,\tau')}\right], \tag{3.30b}$$

$$\delta_{n+1}(\kappa,\tau) = -\int_{-\infty}^{\tau} \mathrm{d}\tau'\,\mathrm{Im}\,\eta_n(\kappa,\tau'), \tag{3.30c}$$

$$\eta_{n+1}(\kappa,\tau) = 2ie^{-i\phi(\tau)}\int_{-\infty}^{\tau} \mathrm{d}\tau'\delta_n(\kappa,\tau')e^{i\phi(\kappa,\tau')}\,, \tag{3.30d}$$

can be expressed in terms of the diabatic phase,

$$\phi(\kappa,\tau) = \int_{-\infty}^{\tau} \mathrm{d}\tau'\,[\kappa - a(\tau')]\,. \tag{3.31}$$

Note that matching at $\tau \to -\infty$ makes this phase divergent. However, in practice this is irrelevant, because one simply matches at some time $\tau \to \tau_0 \ll 0$ for which the driving field is negligible (which is the whole point of the limit).

We demonstrate the accuracy of Equation 3.30 in Figure 3.12 by comparing the asymptotic approximation for the scaled current,

$$j_x^{(n)}(\kappa,\tau) = \frac{\zeta}{4\sqrt{\zeta^2\kappa^2 + M^2}}\sum_{m=0}^{n} M^m\,\delta_m(\kappa,\tau)\,, \tag{3.32}$$

to the exact one, $j_x(\kappa,\tau) = \frac{\zeta}{2}\delta(\kappa,\tau)$, with the solutions $\delta(\kappa,\tau)$ of Equation 3.26. Four pairs of multi-photon numbers and wavevectors with $\zeta = 10$ are examined. The left (right) column panels shows data for $M = 0.1$ ($M = 1$) and the upper (lower) row panels show currents at wavenumber $\kappa = 0.5$ ($\kappa = 0$). In all cases leading and first order approximations coincide, which follows from $\forall\tau,\kappa\;\delta_1(\kappa,\tau) = 0$. Remarkably, out of the second order approximations in panels (a)-(d) of Figure 3.12 only (b) at $\kappa = 0.5$ and $M = 1$ shows any visible deviation from the numerical solution.

Figure 3.12 shows two other striking properties of the approximation: leading and first order in M coincide and they are constant in time (cf. Equation 3.30). While this fact is mathematically obvious from Equation 3.30, let us try to understand it physically in the following.

At leading order in the multi-photon number M Equation 3.26 describe

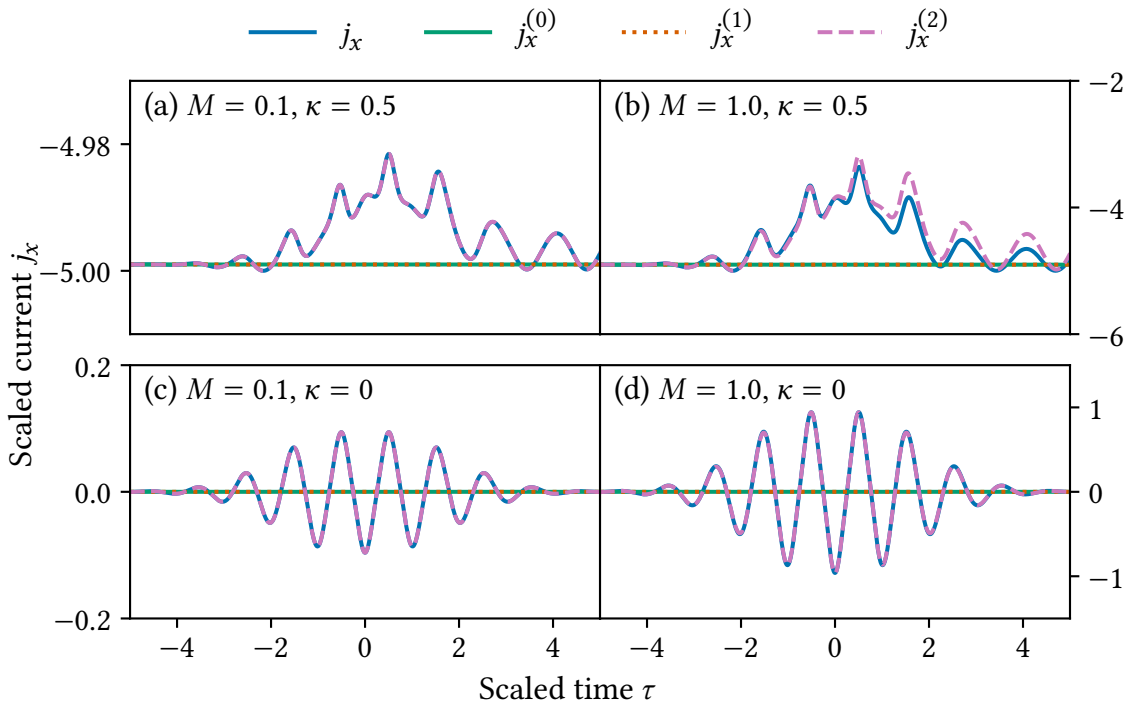


Figure 3.12: Comparison between the asymptotic approximation from Equation 3.32 to the scaled current and numerical solutions for individual κ-modes of the one-dimensional massive Dirac model (see Equation 3.22) with the strong-field parameter $\zeta = 10$. Panels in the top (bottom) row show data for $\kappa = 0.5$ ($\kappa = 0$). The multi-photon number in the left (right) row is given by $M = 0.1$ ($M = 1$). Leading and first order approximations are identical, because $\delta_1(\kappa, \tau) = 0 \forall \kappa, \tau$ (cf. Equation 3.30) with the reason explained in the main text. Evidently, the second order is very accurate in all four cases shown despite the assumption of small multi-photon number.

decoupled left- and right-movers, which results in constant velocity. The only consequence of the driving field here is the movement in $\boldsymbol{\kappa}$-space of left- and right-movers, which influences their energy, but leaves their velocity unchanged. The phase relationship included via the coherences is of first order in our expansion (see Equation 3.29). However, the relative phase is irrelevant for the velocity, thus first order in M has no impact on it—in contrast to other observables like the conduction band occupation. Only at second order the coherences' influence on the imbalance $\delta(\kappa, \tau)$ emerges and hence affects the velocity.

In order to understand coherent suppression analytically, one needs access to the intensities (see Equation 3.21) and in turn to the current densities (cf. Equation 3.18). The latter have no asymptotic expansion of the form shown in Equation 3.28, because the κ-dependency is integrated out. Nevertheless, it is possible to approximate the total current density by expanding the

prefactor in M,

$$\begin{aligned} j_x(\tau, \kappa_y = 0) &\sim \int_{BZ(\tau)} \frac{\mathrm{d}\kappa}{2\pi} \frac{-\zeta^2 \kappa}{4\sqrt{M^2 + \zeta^2 \kappa^2}} [1 + \mathcal{O}(M)] \\ &\sim -\zeta \int_{BZ} \frac{\mathrm{d}\kappa}{8\pi} \{\mathrm{sgn}\,[\kappa + a(\tau)] + \mathcal{O}(M)\} [1 + \mathcal{O}(M)] \\ &\sim -\frac{\zeta}{4\pi} a(\tau) + \mathcal{O}(M)\,. \end{aligned} \tag{3.33}$$

Evidently, the total current density is given by the driving vector potential up to a constant, which is a cosine with a Gaussian envelope (see Equation 3.4). Its Fourier transform is again a Gaussian, such that the emission intensity contains only a single peak at the carrier frequency Ω_0 and no harmonics of high order. This explains the lack of high-frequency peaks for small multi-photon numbers M, but not why inter- and intraband contributions contain such high frequencies. A basis change from diabatic to adiabatic basis yields an expression in terms of the imbalances $\delta(\kappa, \tau)$ and coherences $\eta(\kappa, \tau)$,

$$j_x^{\mathrm{intra}}(\tau, \kappa_y = 0) = \int_{-K}^{K} \frac{\mathrm{d}\kappa}{2\pi} \frac{\zeta^2 \kappa}{2(M^2 + \zeta^2 \kappa^2)} [\zeta \kappa\, \delta(\kappa'_\tau, \tau) - M\, \mathrm{Re}\, \eta(\kappa'_\tau, \tau)] \tag{3.34a}$$

$$j_x^{\mathrm{inter}}(\tau, \kappa_y = 0) = \int_{-K}^{K} \frac{\mathrm{d}\kappa}{2\pi} \frac{\zeta M}{2(M^2 + \zeta^2 \kappa^2)} [M \delta(\kappa'_\tau, \tau) + \zeta \kappa\, \mathrm{Re}\, \eta(\kappa'_\tau, \tau)]\,, \tag{3.34b}$$

where we introduced $\kappa'_\tau = \kappa + a(\tau)$ and the boundaries[‖] $(-K, K)$ of the BZ and used $K > |a(\tau)|$. Intuitively, Equation 3.34 already gives a hint on how the high frequencies in the inter- and intraband spectra arise: for small multi-photon numbers M an imbalance $\delta(\kappa, \tau)$ that is smooth in κ is integrated with a strongly peaked prefactor $1/(M^2 + \zeta^2 \kappa^2)$. A consistent expansion of the integrands above only recovers Equation 3.33, giving vanishing interband current. This demonstrates the highly nonperturbative nature of the inter- and intraband harmonics. To obtain a good approximation for CS, we insert the leading order asymptotic approximation (only $\delta_0(\kappa, \tau)$ and $\eta_0(\kappa, \tau)$), keep the aforementioned prefactor, expand the rest of the integrand as power series in M, and solve the κ-integral

[‖] See Section 2.5 for details on BZ boundary treatment of effective models.

exactly**. The resulting approximation,

$$j_x^{\text{intra}}(\tau, \kappa_y = 0) \approx -\frac{\zeta}{4\pi}\left[a(\tau) - \frac{M}{\zeta}\arctan\left(\frac{\zeta}{M}a(\tau)\right)\right], \tag{3.35a}$$

$$j_x^{\text{inter}}(\tau, \kappa_y = 0) \approx -\frac{M}{4\pi}\arctan\left(\frac{\zeta}{M}a(\tau)\right), \tag{3.35b}$$

includes the leading order approximation to the total current *and* a highly non-linear function of the vector potential. More precisely, the function $\arctan\left(\frac{\zeta}{M}a(\tau)\right)$ behaves like a sharp sigmoid/sign-function for $\zeta \gg M$ with the time-tails smoothed out as the vector potential vanishes there. Note that the arctan appears with *opposite sign* for inter- and intraband current in Equation 3.35. It is precisely this cancellation, which gives rise to coherent suppression.

In Figure 3.13 the emission intensities from the approximations shown in Equations 3.33 and 3.35 are compared to the numerical SBE solutions, demonstrating how closely CS is captured by the analytics. While in the top panel only a single peak in the total emission is captured by the leading order, the bottom panel shows how all odd frequency-multiple peaks and the envelope behavior are recovered. Inspecting Equation 3.35 also reveals that the qualitative impact of the strong-field parameter ζ on CS is captured (as seen in panels (d), (e), and (f) of Figure 3.5): for increasing ζ the function $\arctan\left(\frac{\zeta}{M}a(\tau)\right)$ gets closer to a periodic sign-function, which leads to more high harmonics, closer to a perfect plateau. As such the qualitative picture of CS is represented very well by within this approximation. However, with increasing frequency more deviations from the approximation occur, especially in the valleys between harmonics.

Although an analytical Fourier transform of Equation 3.35 is not known at this point, we can supply a hand-waving argument for the aforementioned plateau-like behavior in the following. Consider the limit of CW driving,

$$j_x^{\text{inter}}(\tau, \kappa_y = 0) \approx -\frac{M}{4\pi}\arctan\left(\frac{\zeta}{M}a(\tau)\right) \to \frac{M}{4\pi}\arctan\left(\frac{\zeta}{M}\cos(\Omega_0\tau)\right), \tag{3.36}$$

such that the Fourier transform turns into a Fourier series,

$$S^{\text{inter}}(\omega, 0) \to S_n^{\text{inter}}(0) = \Omega_0^2 n^2 \left|\frac{1}{T_0}\int_0^{T_0} \mathrm{d}\tau\, \mathrm{e}^{2\pi \mathrm{i}\, n\tau/T_0} j_x^{\text{inter}}(\tau, 0)\right|^2. \tag{3.37}$$

** Note the manipulations leading to Equation 3.35 break the ordering in M.

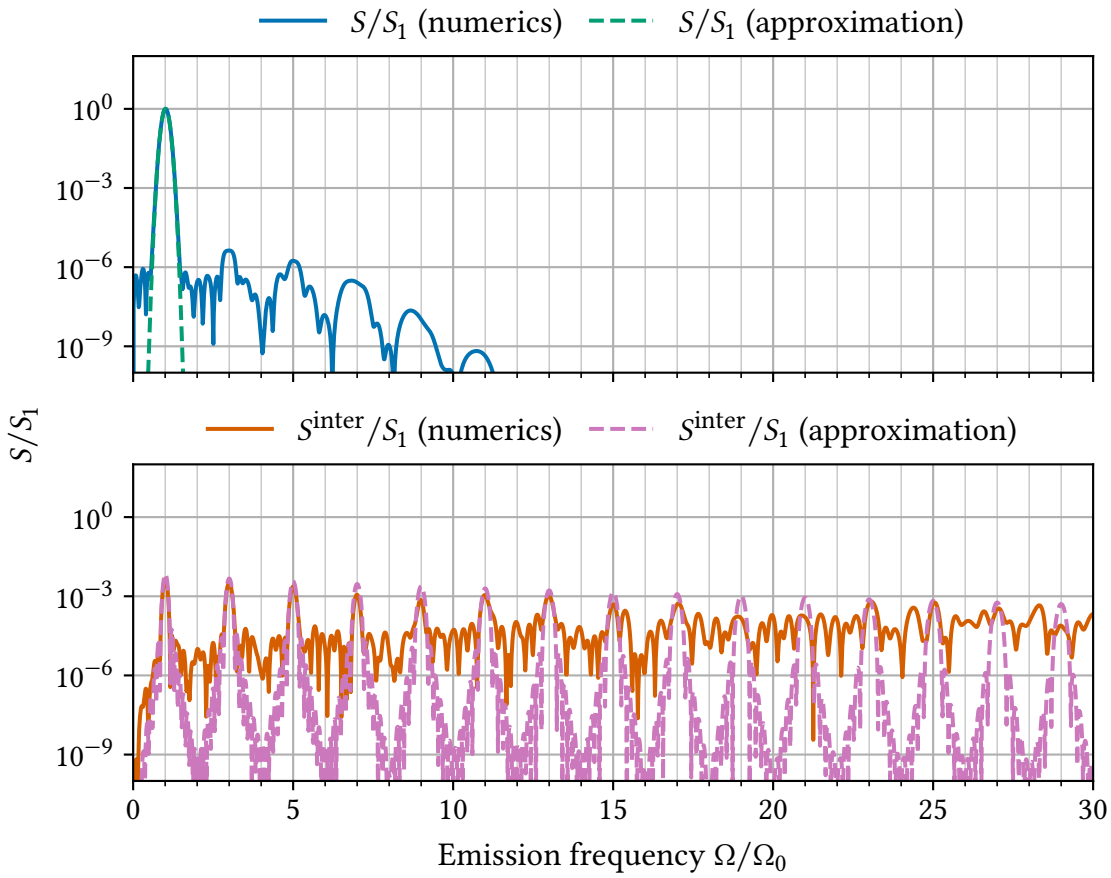


Figure 3.13: Comparison of spectral emission intensity from the approximations given in Equations 3.33 and 3.35 for the total (interband) contribution in the top (bottom) panel. The spectral yields are normalized to the weight of the principal harmonic $S_1 = S(1, 0)$ (see Equation 3.21). The Fourier transformation is calculated numerically and we used the one-dimensional massive Dirac model (Equation 3.22) with $\zeta = 7.5$ and $M = 0.18$ (same parameters as in Figure 3.8 and Figure 3.5, panel (f)). Clearly the approximation presented in Equation 3.36 captures the essential feature of CS: a suppressed total emission intensity together with much larger slowly decaying interband harmonics.

For large arguments[††] of the arctan we can approximate

$$\arctan\left(\frac{\zeta}{M}a(\tau)\right) \approx \frac{\pi}{2}\,\mathrm{sgn}(a(\tau))$$

in Equation 3.36, which precisely turns the interband current into a periodic sign function. A quick calculation shows that

$$S_n^{\mathrm{inter}}(\kappa_y = 0) \propto \Omega_0^2 \sin^2\left(\frac{n\pi}{2}\right), \tag{3.38}$$

i.e. the magnitude of all (odd) harmonics is independent of their order.

Altogether we conclude that the counter-intuitive high-harmonic emission in the inter- and intraband contributions are a result of the highly nonlinear prefactors $\propto 1/(M^2 + \zeta^2\kappa^2)$ in Equation 3.34, which in-turn trace back to the change from diabatic to adiabatic basis with its strongly-peaked matrix-elements around $\boldsymbol{\kappa} = 0$.

Everything we discussed regarding CS up to this point is more of conceptual interest rather than practical, because experiments only have access to the total spectral emission intensity rather than the decomposition from Equation 3.13. In the following section we introduce phenomenological dephasing, which enables observable harmonics of high order created by the mechanism explained above.

3.5 Re-entrant high harmonics

In this section the dephasing mechanism introduced in Section 2.2 is considered, which is implemented by adding a damping term to the coherences in the co-moving Houston basis. To begin with we focus on the one-dimensional model from Equation 3.22 to isolate the CS physics, which takes place mostly around $\kappa_y = 0$. Figure 3.14 shows data for the massive Dirac model (1D) at $\zeta = 7.5$ and $M = 0.18$ with the three different dephasing times $\tau_2 \in \{\infty, 2\,\tau_0, 0.2\,\tau_0\}$. The top panel of Figure 3.14 depicts the spectral yield (see Equation 3.21) and demonstrates that dephasing results in re-entrant harmonics of high order. The inter- and intraband contributions no longer cancel each other in contrast to the perfectly coherent case discussed in the previous section. The bottom panel illustrates the reason for the lifting of CS. The relative phase $\phi(\omega)$ (see Equation 3.13)

[††] This is reasonable in CS regime where $\frac{\zeta}{M} \gg 1$ is satisfied.

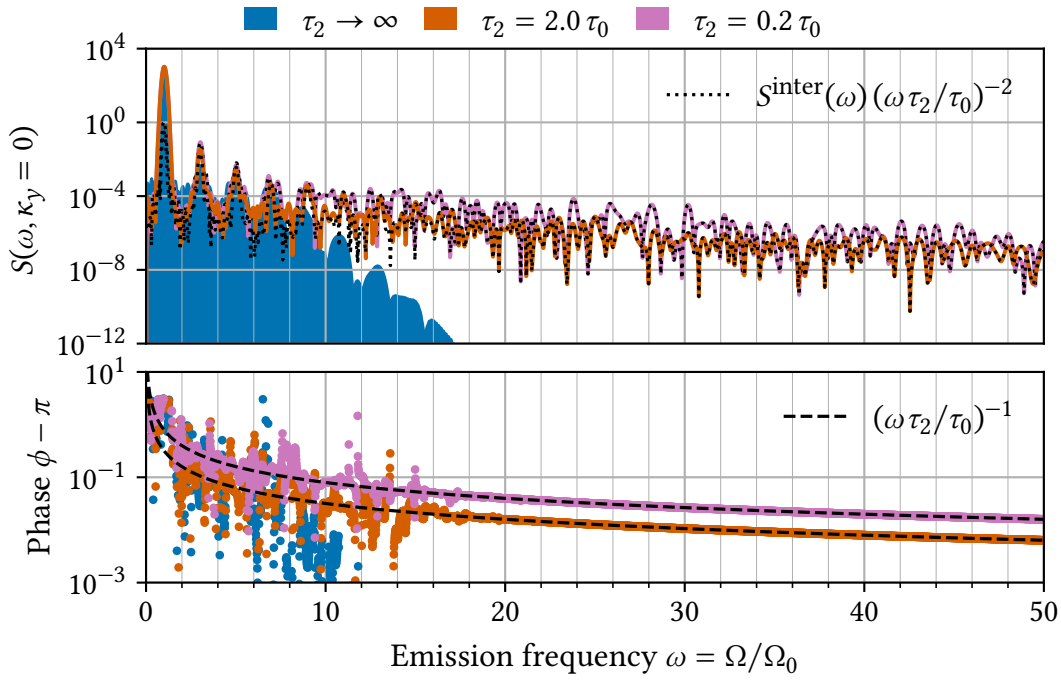


Figure 3.14: Dephasing-induced HHG—spectral yield $S(\omega, \kappa_y = 0)$ (top) from Equation 3.21 and deviation from π of relative phase ϕ (bottom) between inter- and intraband intensities (Equation 3.13) for different dephasing times. Recall that $\Omega = \omega/t_c$. Colors correspond to scaled dephasing times $\tau_2 \to \infty$ (blue), $\tau_2 = 2.0\,\tau_0$ (orange) and $\tau_2 = 0.2\,\tau_0$ (purple). The total emission coincides with $S^{\text{inter}}(\omega)/(\omega\tau_2/\tau_0)^2$ (dotted lines) for $\Omega \gg \Omega_0$. This follows directly from $\phi - \pi \approx 1/(\omega\tau_2/\tau_0)$ (dashed lines in lower panel). Parameters used are $\zeta = 7.5$, $M = 0.18$ and $\sigma = 1.5\,\tau_0$ as in Figures 3.8 and 3.13 and Figure 3.5, panel (f). For a driving frequency of $\Omega_0/2\pi = 10\,\text{THz}$, the scaled dephasing times $\tau_2 \in \{0.2, 2\}$ correspond to $T_2 \in \{20\,\text{fs}, 200\,\text{fs}\}$. Figure adapted from [2].

between inter- and intraband contributions exhibits a simple dependence on frequency and dephasing time,

$$\phi(\omega) \approx \pi - \frac{1}{\omega\,\tau_2/\tau_0} = \pi - \frac{1}{\Omega\,T_2}\,, \tag{3.39}$$

for $\omega \gg \Omega_0$. This dependence is demonstrated numerically by the dashed lines in the bottom panel of Figure 3.14.

Moreover, we observe a near-perfect coincidence of S^{inter} and S^{intra} for $\Omega \gg \Omega_0$ in Figure 3.14. Using Equation 3.39 we can expand the cosine in Equation 3.13, leading to $S(\omega, 0) \approx S^{\text{inter}}(\omega, 0)/(\omega\tau_2)^2$, which is confirmed as a good approximation by the dotted lines in the upper panel of Figure 3.14. Although Equation 3.39 is of a very simple analytical form, it is currently a purely numerical observation and no derivation from the equations of motion is known to the author. We suspect that a formulation in frequency- rather than time-space of the SBE might be amenable

to approximation, by assuming that high frequencies are only weakly (perhaps perturbatively) affected by dephasing.

We continue our analysis with the full, two-dimensional massive Dirac model (Equation 3.6) in Figure 3.15, which shows the emission intensity for four different dephasing strengths, $\tau_2 \to \infty$, $\tau_2 = 20\,\tau_0$, $\tau_2 = 2\,\tau_0$, and $\tau_2 = 0.2\,\tau_0$. All other parameters of the massive Dirac system used for the data shown in Figure 3.15 set to the same values as in Figure 3.14. As discussed in Section 3.3, a HHG-plateau with a cutoff roughly at the 11th harmonic is visible which is absent in the one-dimensional case. The plateau gradually disappears for stronger dephasing, especially for characteristic times τ_2 below one laser cycle. Beyond this cutoff, re-entrant harmonics emerge for finite dephasing times. These harmonics for $\tau_2 = 2\,\tau_0$ and $\tau_2 = 20\,\tau_0$ seem to differ only by a multiplicative constant. On the other hand, for strong dephasing ($\tau_2 = 0.2\,\tau_0$) the shape of the emission spectrum also changes. The change in shape hints at the fact that strong dephasing qualitatively influences the dynamics, but weak dephasing manifests primarily through the relative phase of inter- and intraband currents as observed in Figure 3.14.

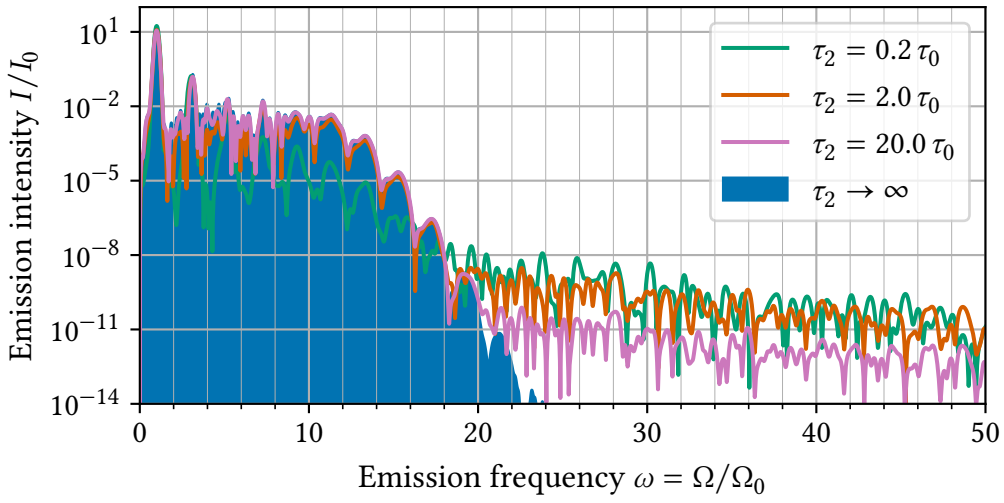
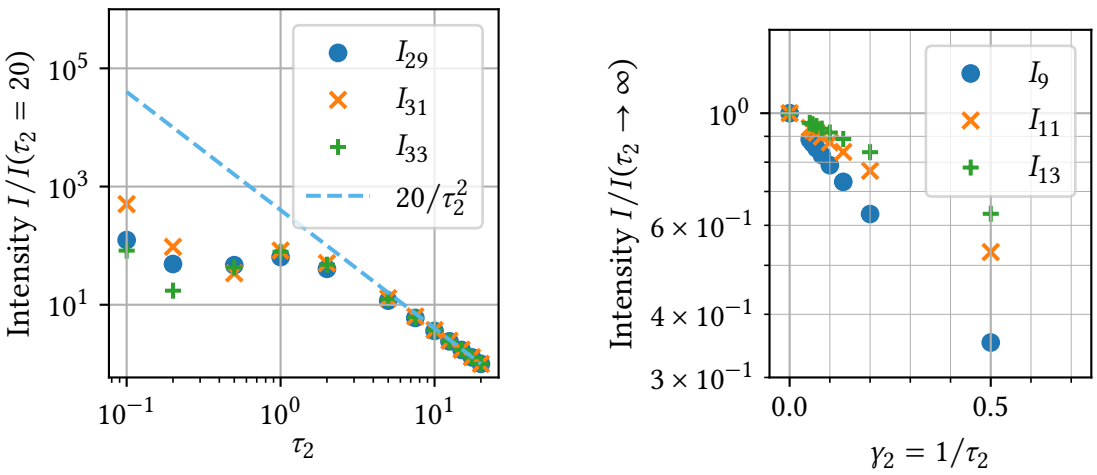


Figure 3.15: Effect of dephasing on high-harmonic emission intensity $I(\omega)$ for the driven two-dimensional massive Dirac model for dephasing times $\tau_2 \to \infty$ (blue), $\tau_2 = 1\,\tau_0$ (purple), and $\tau_2 = 0.1\,\tau_0$ (orange) in units of the laser cycle τ_0. Re-entrance of high-harmonic emission beyond the plateau is clearly visible, but less pronounced compared to the one-dimensional model (see Figure 3.14). Parameters are $\zeta = 7.5$, $M = 0.18$, and $\sigma = 5.5\,\tau_0$ (as in Figure 3.5, panel (f) and marked by □ in Figure 3.6). For a driving frequency of $\Omega_0/2\pi = 10\,\mathrm{THz}$, the scaled dephasing times $\tau_2 \in \{0.2, 2, 20\}$ correspond to $T_2 \in \{20\,\mathrm{fs}, 200\,\mathrm{fs}, 2\,\mathrm{ps}\}$. Figure adapted from [2].

‡‡ The value $\tau_2 = 20\,\tau_0$ in Figure 3.16b represents an arbitrarily chosen number in the weak dephasing regime. In contrast to Figure 3.16a it is impossible to normalize to $\tau_2 \to \infty$, since there the intensity lies below the numerical noise threshold and cannot be reliably extracted.



(a) Harmonic instensity of re-entrant harmonics (29th, 31st, and 33rd) versus dephasing time normalized to the intensity for $\tau_2 = 20\,\tau_0$[‡‡]. The power-law fit (blue dashed line) shows that the primary effect of weak dephasing is the change of the relative inter- and intraband phase (see Equation 3.39 and following discussion).

(b) Influence of dephasing strength $\gamma_2 = 1/\tau_2$ on normalized intensity of the 9th, 11th, and 13th harmonic (below cutoff). Contrary to the re-entrant harmonics these follow an exponential rather than a power law, which is consistent with the three-step model (see main text).

Figure 3.16: Dependence of harmonics below (left) and above (right) the cutoff on dephasing strength for the driven two-dimensional massive Dirac model at $\zeta = 7.5$, $M = 0.18$, and $\sigma = 1.5\,\tau_0$ (as in Figures 3.14 and 3.15 and marked by □ in Figure 3.6).

We provide further evidence for qualitatively distinct behavior of harmonics below and above the cutoff in Figure 3.16a. The latter harmonics follow a power-law dependence as $\propto \tau_2^{-2}$, consistent with Equation 3.39, for $\tau_2 \gtrsim 2\,\tau_0$, but clearly deviate for shorter times τ_2. The former harmonics behave as $\propto \mathrm{e}^{-\mathrm{const}\times\gamma_2}$ for weak dephasing, see Figure 3.16b. The exponential dependence on dephasing is expected from the Lewenstein/three-step-model where the amplitude from every classical trajectory of duration $\Delta\tau$ contributes with a factor $\mathrm{e}^{-\Delta\tau/\tau_2}$ [14, 37]. At this point the role of the constant in the exponential $\propto \mathrm{e}^{-\mathrm{const}\times\gamma_2}$ is unknown, but this is an intriguing avenue of future research, since it might reveal how to make the three-step model more quantitative in these small-gap systems.

One striking feature of the re-entrant harmonics both in the one- and two-dimensional massive Dirac models (cf. Figures 3.14 and 3.15) is the apparent lack of a clear harmonic structure as compared to the lower-order harmonics, i.e. they are more "noisy" (see Figures 3.14 and 3.15). In Section 3.4 we gave an argument for the generation of harmonics in the intra- and interband contributions, which relied on approximating the arctan in Equation 3.36 as a sign function ("CW-driving limit"). We

expect these harmonics to become sharper for longer pulse durations. Since the re-entrant harmonics are proportional to the coinciding inter- and intraband (shown above), they should respond accordingly to longer pulses. Figure 3.17 demonstrates this behavior of the re-entrant harmonics for longer pulse durations by showing the emission intensity for massive Dirac system driven by a longer pulse with $\sigma = 7.5\,\tau_0$ and for the two dephasing times $\tau_2 = 0.5\,\tau_0$ and $\tau_2 = 5\,\tau_0$. The inset shows the time-dependence of the electric field in contrast to the shape used throughout the rest of this chapter (cf. Figure 3.2).

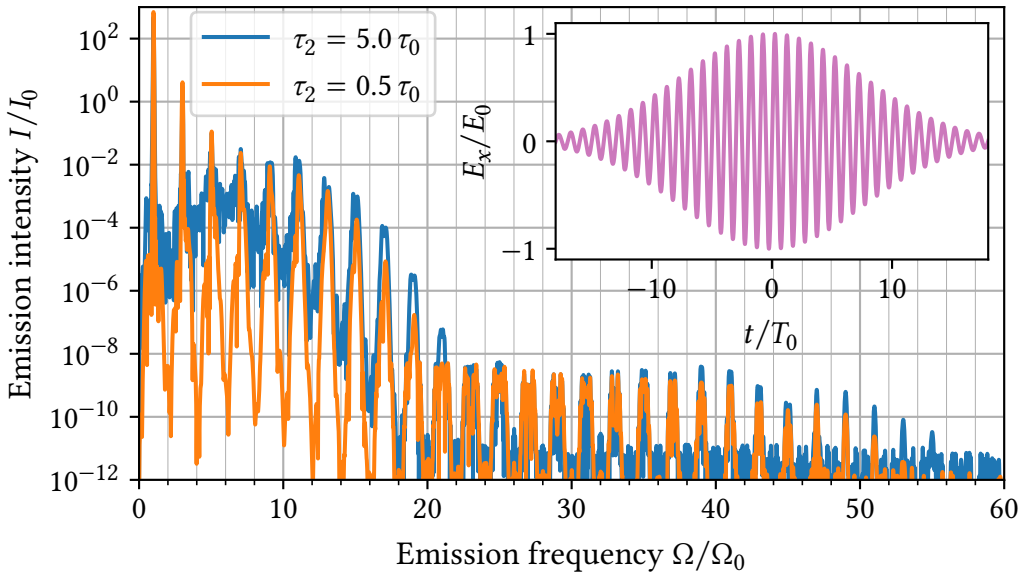


Figure 3.17: Influence of pulse duration on re-entrant HHG. Total emission intensity $I(\omega)$ for the driven two-dimensional massive Dirac model for the dephasing times $\tau_2 = 0.5\,\tau_0$ (orange) and $\tau_2 = 5\,\tau_0$(blue). Strong-field parameter and multi-photon number are the same as in Figure 3.15 ($\zeta = 7.5$ and $M = 0.18$). The system is driven by a longer pulse with $\sigma = 7.5\,\tau_0$ as compared to previous data in this chapter. The longer duration leads to more pronounced re-entrant harmonics beyond the plateau, which is consistent with the approximation proposed in Section 3.4 (see main text). The inset shows the time dependence of the electric field strength E in terms of the maximum E_0. For a driving frequency of $\Omega_0/2\pi = 10\,\mathrm{THz}$, the scaled standard deviation of the pulse corresponds to $\Delta t = 750\,\mathrm{fs}$.

3.6 Conclusions and outlook

In this chapter, we investigated the phenomenon of coherent suppression of high harmonics in two-dimensional light-driven systems, which arises from destructive interference between interband and intraband currents at high frequencies. We systematically extended earlier observations [45,

46] by exploring a broad region of parameter space in the massive Dirac model. We provided the first analytical approach that clarifies the physical mechanism behind CS. In addition, we demonstrated that CS also occurs in a model of bilayer graphene, supporting the notion that this effect is of a generic nature rather than tied to a specific dispersion.

Our analysis shows that a small multi-photon number,

$$M = \frac{E_{\mathrm{gap}}}{\Omega_0} ,$$

is a key prerequisite for the emergence of CS. Importantly, this dimensionless parameter can be defined for arbitrary band structures. Identifying the multi-photon number as the relevant control parameter enabled an analytical treatment of an effective one-dimensional model describing modes that pass through, or remain close to, the Dirac point under linearly polarized driving. These modes reveal the physical origin of CS: they predominantly follow *diabatic states* rather than the adiabatic band basis, resulting in a current that closely tracks the driving field and therefore lacks high-harmonic components. By contrast, the individual interband and intraband currents acquire harmonic of high order due to the rapidly varying dipole and velocity matrix elements in the vicinity of the Dirac point.

We further showed that CS is lifted when dephasing is included, giving rise to re-entrant harmonics. This behavior can be traced back to a characteristic scaling of the relative interband–intraband phase proportional to $\propto 1/(\omega\tau_2)$. As a consequence, high harmonics above the HHG plateau exhibit a scaling behavior opposite to that of harmonics below the plateau. These findings suggest that controlling the dephasing time T_2 provides direct insight into the microscopic mechanisms underlying HHG. With sufficiently precise control, T_2 may even be extracted without fitting the full HHG spectrum. Experimental knobs such as temperature variation or resonant photo-doping [36] offer possible routes toward this control, although a more detailed understanding of the relevant microscopic dephasing channels will be required for quantitative conclusions.

Floquet-Bloch sidebands with finite driving pulses

4

This chapter is concerned with the buildup of transient Floquet side bands in topological insulator surface states through the pumping with a pulsed laser. The theoretical method introduced in Section 2.7 relies on a periodic signal—the pump pulse—with an envelope changing on a slower time scale.

In Section 4.1 a well-established model for TI surface states of the Bi_2Se_3-family is presented, which is used to study Floquet side bands.

We demonstrate the buildup of Floquet replicas in Section 4.2 and reveal how the side band population and the quasi-energy spectrum evolves with time. Higher order terms responsible for the well-known hexagonal warping of the system's band structure also crucially impact the Floquet spectra, leading to avoided crossings.

In Section 4.3 we use the picture of adiabatic evolution and nonadiabatic transitions introduced in Section 2.1 to explain the occupation dynamics in the Floquet side bands. Comparison to adiabatic perturbation theory and Landau-Zener transition probability are shown for two exemplary Bloch states.

The bulk of this chapter is based on [3] with additional insight provided by the adiabatic approximation introduced in Section 2.7.

4.1 A model for topological instulator surface states . . . 72
4.2 Floquet sidebands in topological insulators 74
4.3 Adiabaticity in Floquet sidebands 78
4.4 Conclusions and outlook 81

4.1 A model for topological instulator surface states

In this section we introduce a well-established model for the Bi_2Se_3-family (additionally including Bi_2Te_3 and Sb_2Te_3) of materials. For these systems the surface states can be described by an effective Hamiltonian,

$$\hat{\mathscr{H}}_{\mathrm{TI}}(\boldsymbol{k}) = \left(C_0 + C_2\boldsymbol{k}^2\right) + v\left(k_y\hat{\sigma}_x - k_x\hat{\sigma}_y\right) + r(k_+^3 + k_-^3)\hat{\sigma}_z \,, \tag{4.1}$$

with $k_\pm = k_x \pm \mathrm{i}k_y$ and the constants,

$$c_0 = C_0 + \alpha_3 M_0 \,, \quad c_2 = C_2 + \alpha_3 M_2 \,, \quad v = v_0\alpha_1 \,, \quad r = R_1\alpha_1/2 \,, \tag{4.2}$$

see references [127, 165, 166]. The numerical values of the Hamiltonian's parameters are given in Table 4.1.

We consider driving by a linearly polarized electric field,

$$\boldsymbol{E}(t) = -\frac{\partial \boldsymbol{A}}{\partial t} \,, \quad \boldsymbol{A}(t) = \frac{E_0}{\Omega_0}\eta(t)\boldsymbol{e}_x \sin(t) \,, \quad \eta(t) = \mathrm{e}^{-t^2/2\Delta t^2} \,, \tag{4.3}$$

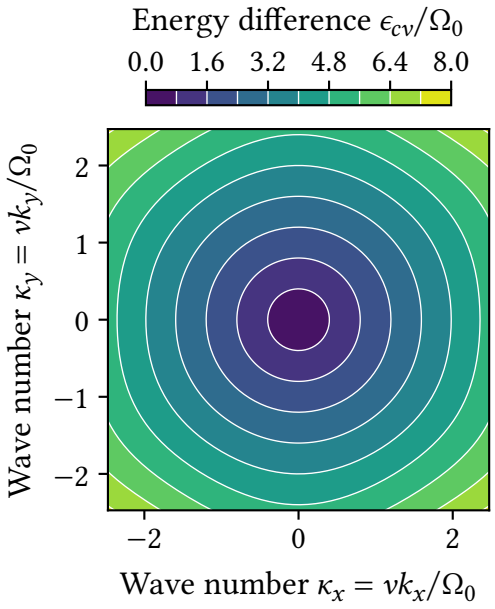
where we introduced the slow time scale η according to the t–t' formalism introduced in Section 2.7. Throughout this chapter we fix $\Omega_0/2\pi = 38.7\,\mathrm{THz}$, $\Delta t = 38.8\,\mathrm{fs}$, and $E_0 = 3.11\,\mathrm{MV\,cm^{-1}}$. Hence, the frequency is exactly the same and the peak field strength larger by a factor of about 2.7 when compared to [167]. The pulse duration was intentionally chosen very short in order to access a regime which is not amenable to traditional Floquet theory. Including the vector potential via minimal coupling $\boldsymbol{k} \to \boldsymbol{k} - \boldsymbol{A}(t)$ and comparing the resulting hamiltonian with Equation 2.83 allows an identification of the time-dependent and unperturbed parts,

$$\hat{W}(\boldsymbol{k}, \eta, t) = \hat{W}_x(\boldsymbol{k}, \eta, t) + \hat{W}_y(\boldsymbol{k}, \eta, t) + \hat{W}_{xy}(\boldsymbol{k}, \eta, t) \,, \tag{4.4}$$

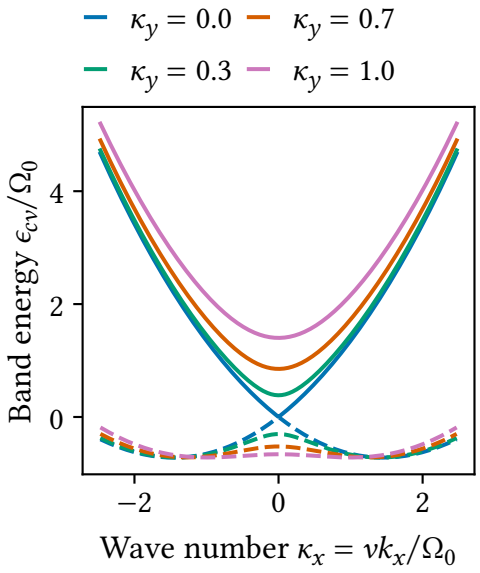
$$\hat{\mathscr{H}}_0(\boldsymbol{k}) = \hat{\mathscr{H}}_{\mathrm{TI}}(\boldsymbol{k}) \,, \tag{4.5}$$

Table 4.1: Numerical values of constants for the TI model Hamiltonian given in Equation 4.9. All quantities are given in atomic units besides α_1 and α_3, which are numbers.

Constant	v_0	C_0	M_0	R_1	C_2	M_2	α_1	α_3
Value [a.u.]	0.23	-3.1×10^{-4}	−0.010	13	4.0	5.8	0.99	-0.15



(a) Contours of energy difference of valence and conduction band in reciprocal space $\boldsymbol{\kappa} = (\kappa_x, \kappa_y)$.



(b) One-dimensional slices of band energy in κ_x-direction for different fixed κ_y (color-coded). Solid (dashed) lines show conduction (valence) band energy.

Figure 4.1: Band structure for the (scaled) Bi_2Se_3 model (see Equations 4.1 and 4.9) for the parameters given in Table 4.1. The contours of the energy difference in panel (a) is very similar to the massive Dirac model (see Figure 3.3) with the hexagonal warping effect being visible only for larger $|\boldsymbol{\kappa}|$ at the edges of the contours. Panel (b) shows the change due to the quadratic term, bending both valence and conduction band upwards with increasing $|\boldsymbol{\kappa}|$.

with three different components,

$$\hat{W}_x = 2r\hat{\sigma}_x A_x^3(t) + (c_2 + 6rk_x\hat{\sigma}_z)A_x^2(t) + \left[6r\left(k_x^2 - k_y^2\right)\hat{\sigma}_z + 2c_2k_x - v\hat{\sigma}_y\right]A_x(t)\,, \tag{4.6a}$$

$$\hat{W}_y = [c_2 - 6rk_x\hat{\sigma}_z]A_y^2(t) + \left[2c_2k_y - 12rk_xk_y\hat{\sigma}_z + v\hat{\sigma}_x\right]A_y(t)\,, \tag{4.6b}$$

$$\hat{W}_{xy} = -6r\hat{\sigma}_z A_x(t)A_y^2(t) - 12rk_y\hat{\sigma}_z A_x(t)A_y(t)\,, \tag{4.6c}$$

coupling to A_x, A_y, and both respectively. For the linear polarization considered the two contributions $\hat{W}_y$ and $\hat{W}_{xy}$ vanish.

In Chapter 3 we let the length scale be determined by the field strength of the driving radiation. This choice is convenient for analyzing variation of the strong-field parameter investigated in the aforementioned chapter. However, here we consider only a single exemplary field-strength, hence we choose the dominant $\boldsymbol{k}$-terms (linear) as reference. The higher-order terms of $\hat{H}_{\mathrm{TI}}$ also prevent a simple scaling with the field strength as it was

possible in the massive Dirac system.

For the aforementioned reasons the time scale is set to

$$t_c = \frac{1}{\Omega_0} \tag{4.7}$$

and the length scale is set to

$$l_c = \frac{v}{\Omega_0} \,. \tag{4.8}$$

As a result we obtain the dimensionless Hamiltonian,

$$\hat{H}_{\mathrm{TI}}(\boldsymbol{k}) = \left(\gamma_0 + \gamma_2 \boldsymbol{\kappa}^2\right) + \left(\kappa_y \hat{\sigma}_x - \kappa_x \hat{\sigma}_y\right) + \gamma_3 (\kappa_+^3 + \kappa_-^3)\hat{\sigma}_z \,, \tag{4.9}$$

describing the TI surface states with

$$\gamma_0 = \frac{C_0}{\Omega_0} \,, \quad \gamma_2 = \frac{C_2}{v^2} \,, \quad \gamma_3 = \frac{r^2}{v^3} \,, \quad \text{and} \quad \kappa_\pm = \kappa_x \pm \mathrm{i}\,\kappa_y \,. \tag{4.10}$$

Figure 4.1 depicts the contours of the conduction and valence band's energy difference and band structure slices along κ_x. The contours show a strong similarity to the massive Dirac model (see Figure 3.3), demonstrating the dominance of the terms linear in $\boldsymbol{k}$ for the band energy difference. Only for large wave numbers the hexagonal warping becomes visible in panel (a) of Figure 4.1. Figure 4.1, panel (b) shows slices of the band structure along k_x, where the importance of the term quadratic in $\boldsymbol{\kappa}$ can be seen. The term bends both bands upwards, breaking electron-hole symmetry.

4.2 Floquet sidebands in topological insulators

This section is concerned with the buildup of Floquet sidebands in Bi_2Se_3 and thereby following Ref. [3]. To this end we analyze the time-dependence of the instantaneous Floquet coefficients $c_\alpha(\boldsymbol{k}, t)$ and the quasi-energies $\xi_\alpha(\boldsymbol{k}, t)$, which follow Equation 2.92. Solving the time evolution of $c_\alpha(\boldsymbol{k}, t)$ is equivalent to solving the TDSE for individual $\boldsymbol{k}$-modes. With the velocity gauge considered here the time evolution of an ensemble of $\boldsymbol{k}$-modes is equivalent to the SBE without dephasing. Therefore, the instantaneous Floquet formalism for an ensemble of Bloch states is in fact the lowest

order of the many-body quantum cluster expansion and hence not merely a single-particle approach.

With that equivalence to the SBE without dephasing in mind, the initial state of the system is given by Equation 2.31. In [3] the Fermi level was set to the Dirac point, but in experiments [56, 167] it often lies in the conduction band. To take these experimental parameters into account, we set $T = 300\,\mathrm{K}$ and $E_F = 0.3\,\mathrm{eV}$ in accordance with [167]. The initial state is then a mixed state such that the most straightforward way to calculate the time evolution would be in the density matrix formalism, i.e. solving the SBE. The generalization of the t–t' formalism to the SBE (without dephasing) is fairly clear-cut: one can write the equations of motion (Equation 2.92) in Liouville space which essentially amounts to writing the entries of the density matrix as a column vector (see [69, 70, 168]). Then, we obtain a matrix differential equation form-equivalent to the TDSE,

$$\frac{\partial}{\partial t}\boldsymbol{\varrho}(\boldsymbol{k},t) = \hat{\mathscr{L}}(\boldsymbol{k},t)\,\boldsymbol{\varrho}(\boldsymbol{k},t)\,, \tag{4.11a}$$

$$\hat{\mathscr{L}}(\boldsymbol{k},t) = -\mathrm{i}\Big[\hat{\mathscr{H}}(\boldsymbol{k},t),\ \cdot\ \Big]\,, \tag{4.11b}$$

where $\boldsymbol{\varrho}(\boldsymbol{k},t)$ is a column vector of all density matrix elements and $\hat{\mathscr{L}}(\boldsymbol{k},t)$ a matrix operator with respect to some chosen basis. The t–t' formalism can be applied to Equation 4.11 analogous to the TDSE. However, at the time of writing the code from [3] lacks the possibility of solving Equation 4.11 with t–t'. Therefore, we employ the pedestrian route to a mixed state of solving Equation 2.92 for the conduction and valence band contributions separately and summing the Floquet occupations.

Figure 4.2 visualizes the time-dependence of $c_\alpha(\boldsymbol{k},t)$ and $\xi_\alpha(\boldsymbol{k},t)$ for a cut along k_x through the Dirac cone ($k_y = 0$): the band occupations (color-coded) are projected over the instantaneous Floquet spectrum for six different times during the pulse using the driving field and TI Hamiltonian introduced in the previous section. Hence, the system differs from the data shown figure 11 of [3] merely in the (slightly longer) pulse duration and the mixed initial state.

Remarkably, the instantaneous Floquet quasi-energies themselves barely change in form during the system's time evolution. Mainly there is an overall shift due to the term quadratic in $\boldsymbol{k}$, which is proportional to the identity matrix, with time, see Equations 4.1 and 4.9. This shifting has no influence on the occupation dynamics, because it can be absorbed into a unitary transform for each $\boldsymbol{k}$-point. Closer inspection also reveals a slight

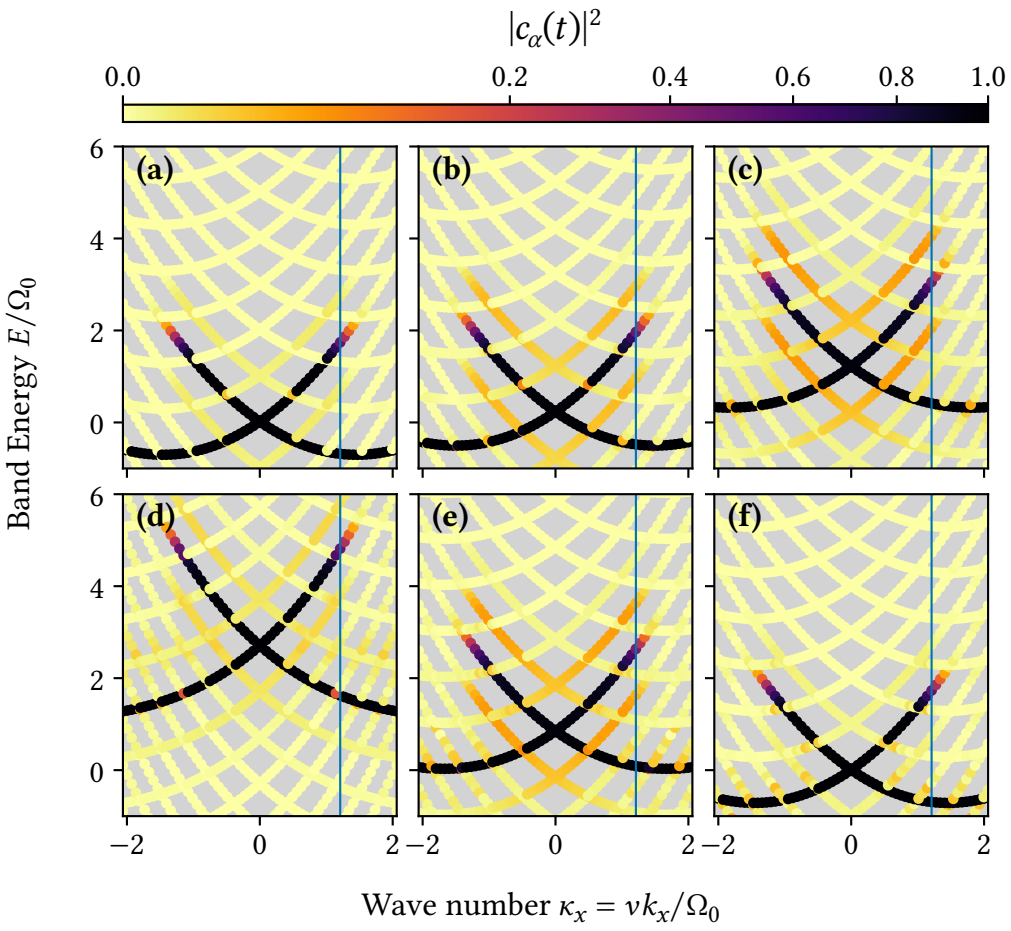


Figure 4.2: Expansion coefficients $|c_\alpha(\boldsymbol{k}, t)|$ (see Equation 2.92) projected over instantaneous Floquet quasi-energies along k_x ($k_y = 0$) for times $t/T_0 \in \{-3.36, -2.36, -1.36, -0.26, 1.64, 3.64\}$ in panels (a)-(f) for the TI model shown Equations 4.1 and 4.9. The Hamiltonian's parameters are given in Table 4.1 and the driving field from Equation 4.3 with frequency $\Omega_0/2\pi = 38.7\,\mathrm{THz}$, duration $\Delta t = 38.8\,\mathrm{fs}$, and $E_0 = 3.11\,\mathrm{MV\,s^{-1}}$ is employed. The initial state is given by Equation 2.31 with $T = 300\,\mathrm{K}$ and $E_F = 0.3\,\mathrm{eV}$. The times are marked in Figures 4.4 and 4.5 for reference. The vertical blue lines mark the wave number $\kappa_x = 1.21$, corresponding data shown in Figure 4.5.

compression of the spectrum along k_x, we come back to its relevance in Section 4.3.

At the time when the driving field begins, shown in panel (a) of Figure 4.2, we observe occupation up to the Fermi level and no sideband population. As the pulse becomes stronger with time, there is an increasing shift towards higher and lower replicas (mostly adjacent sidebands), see panels (b), (c), and (e) of Figure 4.2. In Figure 4.2, panel (d) at the time of maximum driving field strength the shift and stretch of the spectrum is maximal but the occupations are hardly spread over more than a single replica. This counter-intuitive concentration on one Floquet band is explained further below (Section 4.3). Towards the end of the pulse

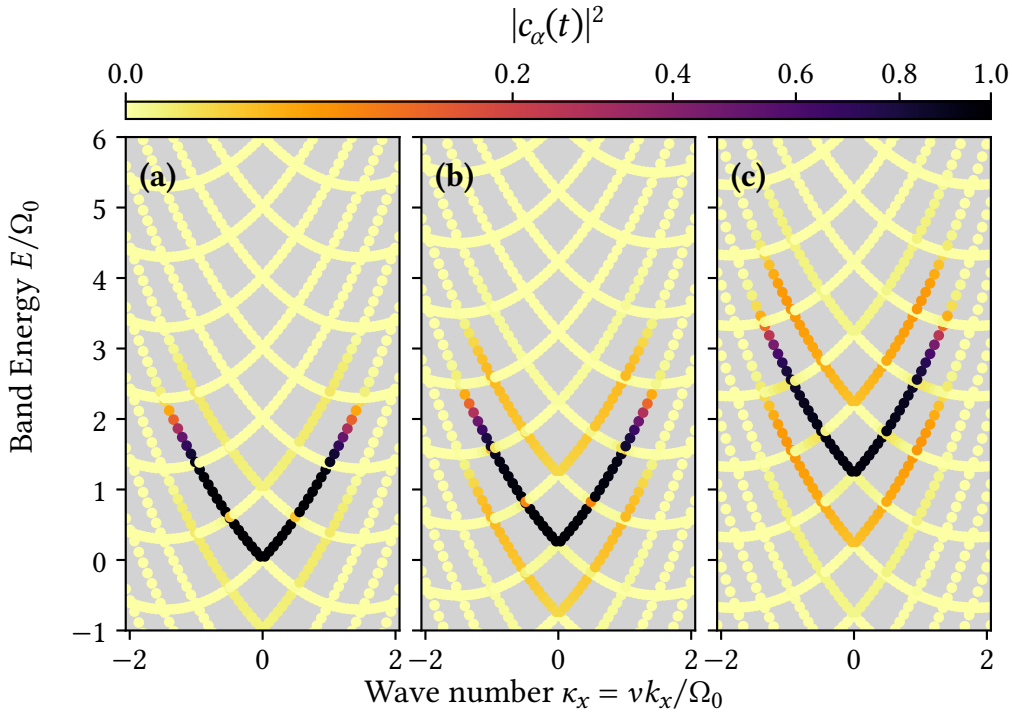


Figure 4.3: Expansion coefficients $|c_\alpha(\boldsymbol{k}, t)|$ (see Equation 2.92) projected over instantaneous Floquet quasi-energies along k_x ($k_y = 0$) for times $t/T_0 \in \{-3.36, -2.36, -1.36\}$ in panels (a)-(f) for the TI model shown Equations 4.1 and 4.9. The Hamiltonian's parameters are given in Table 4.1 and the driving field from Equation 4.3 with frequency $\Omega_0/2\pi = 38.7\,\mathrm{THz}$, duration $\Delta t = 38.8\,\mathrm{fs}$, and $E_0 = 3.11\,\mathrm{MV\,cm^{-1}}$ is employed. The initial state is given by Equation 4.12 with $T = 300\,\mathrm{K}$ and $E_F = 0.3\,\mathrm{eV}$. The times are marked in Figures 4.4 and 4.5 for reference.

in panel (f) of Figure 4.2 the Floquet expansion coefficients have nearly returned to their initial state with some remnant occupations visible for isolated $\boldsymbol{k}$-points.

It was found in [3] that valence band states primarily couple to other valence-band type replicas. Figure 4.2 suggests that conduction-band type sidebands behave just like the valence-band types. In order to investigate this numerically, we choose the initial state

$$\rho_{vv}(\boldsymbol{k})^{\mathrm{in}} = \frac{1}{\mathrm{e}^{\beta[\epsilon_v(\boldsymbol{k}) - \epsilon_\mathrm{F}]}}\,, \tag{4.12}$$

$$\rho_{cc}(\boldsymbol{k})^{\mathrm{in}} = \rho_{cv}(\boldsymbol{k})^{\mathrm{in}} = \rho_{vc}(\boldsymbol{k})^{\mathrm{in}} = 0\,, \tag{4.13}$$

with $T = 300\,\mathrm{K}$ and $E_F = 0.3\,\mathrm{eV}$. This state is nothing but the conduction part only of the mixed state used above (Equation 2.31). By investigating the expansion coefficients only for the conduction band part of the mixed initial state in Figure 4.3 we prove that this holds true for the conduction band states as well. As discussed in [3], near the Dirac point the

system behaves essentially like a Dirac model which can be integrated trivially. However, for larger k_x the hexagonal warping terms become increasingly important and substantially impact the dynamics, creating avoided crossings in the Floquet spectrum. In the subsequent section we will disentangle these dynamics with the intuitive picture of adiabatic and diabatic dynamics introduced in Section 2.1 applied to the instantaneous Floquet formalism (see Section 2.7).

4.3 Adiabaticity in Floquet sidebands

By reformulating the equations of motion for the instantaneous Floquet coefficients from Equation 2.92 to Equation 2.95 we can apply the physical picture introduced in Section 2.1 to the Floquet states. As hinted at in the preceding section, there are two regimes along the k_x-axis for large and small $|k_x|$. In the latter region, the Dirac-like term $v(k_y\hat{\sigma}_x - k_x\hat{\sigma}_y)$ dominates the dynamics and in the former the hexagonal warping term $r(k_+^3 + k_-^3)\hat{\sigma}_z$ becomes more relevant.

Figure 4.4 shows data from the Dirac-like regime. Initially, the 0-th order valence band replica is fully occupied and we show the population of valence band order -1 in the top panel. Additionally, the first order correction from adiabatic perturbation theory is depicted for comparison (see Equation 2.96 for the formula*). This approximation agrees very precisely with the numerical results and in turn proves we are deep in the adiabatic regime. Moreover, the two maxima of $c_{(v,-1)}(\boldsymbol{k}, t)$ coincide in time with the most significant sideband population in panels (b), (c), and (e) of Figure 4.2. We conclude that the primary reason for sideband population in the instantaneous Floquet spectra shown in Figure 4.2 is an *adiabatic correction* to the coefficients of the IFS.

The dip occurring at the time where the driving field is strongest (around $t = 0$) corresponds to the counter-intuitive lack of side band occupation in Figure 4.2, panel (d) and can be explained by the adiabatic picture: the first order correction is proportional to $\frac{\mathrm{d}\eta}{\mathrm{d}t}$ and therefore vanishes at the maximum of the envelope function $\eta(t)$.

In Figure 4.5 we analyze the k_x-region where the hexagonal warping term becomes important and leads to avoided crossings in the instantaneous

* To be precise, the approximation in Equation 2.96 differs by a phase factor, but this is irrelevant for the occupations.

Floquet spectrum. The time-dependence of the quasi-energies (bottom panel) shows a crossing of $(v, 0)$ and $(c, -1)$ replicas, but at the scale it is impossible to see whether it is an avoided or a true crossing. In the center panel of Figure 4.5 we plot the difference of those quasi-energies and only then it becomes visible that the crossing is gapped. The top panel reveals the almost instantaneous and full population transfer from $(v, 0)$ to $(c, -1)$ at the crossings. Thus, we are in the diabatic regime (cf. panel (b) of Figure 2.2).

A numerical fit of the crossing's parameters (dashed yellow line, center panel of Figure 4.5) allows the extraction of the Landau-Zener transition probability of $P_{LZ} = 0.997$, which is consistent with a diabatic transition.

Let us connect this transition picture to the instantaneous Floquet spectra shown in Figure 4.2, where no abrupt transitions are apparent at first glance. As the Floquet spectrum is continuously "stretched" in time, the

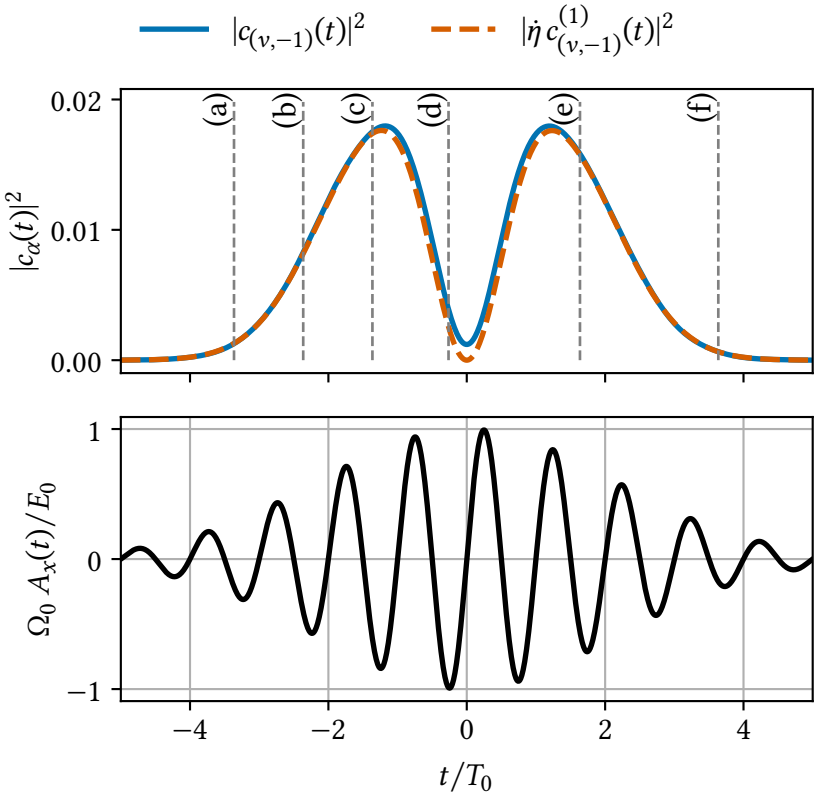


Figure 4.4: Time dependence of exemplary Floquet coefficients (top) and the driving field (bottom) at $\boldsymbol{\kappa} = (0.098, 0)$ for the TI model given in Equations 4.1 and 4.9 with parameters taken from Table 4.1. The driving field is given in Equation 4.3 with frequency $\Omega_0/2\pi = 38.7\,\mathrm{THz}$, duration $\Delta t = 38.8\,\mathrm{fs}$, and $E_0 = 3.11\,\mathrm{MV\,cm^{-1}}$ (all system parameters are as in Figure 4.2). Vertical dashed lines indicate the times shown in the panels of Figure 4.2. Top panel depicts occupations of the first valence band replica (solid blue) and its first order adiabatic approximation (dashed orange) calculated from Equation 2.96.

crossings visible in Figure 4.2 sweep past individual $\boldsymbol{k}$ modes. For example, between the time snapshots shown in panels (c) and (d), a crossing passes the $\kappa_x = 1.21$ mode, corresponding to the data shown in Figure 4.5. As demonstrated there, this crossing is in fact an *avoided crossing* associated with a diabatic transition, even though no clear population transfer is visible in Figure 4.2. Only if the transition probability were significantly below unity would the instantaneous Floquet spectrum exhibit visible population leakage in the vicinity of such crossings.

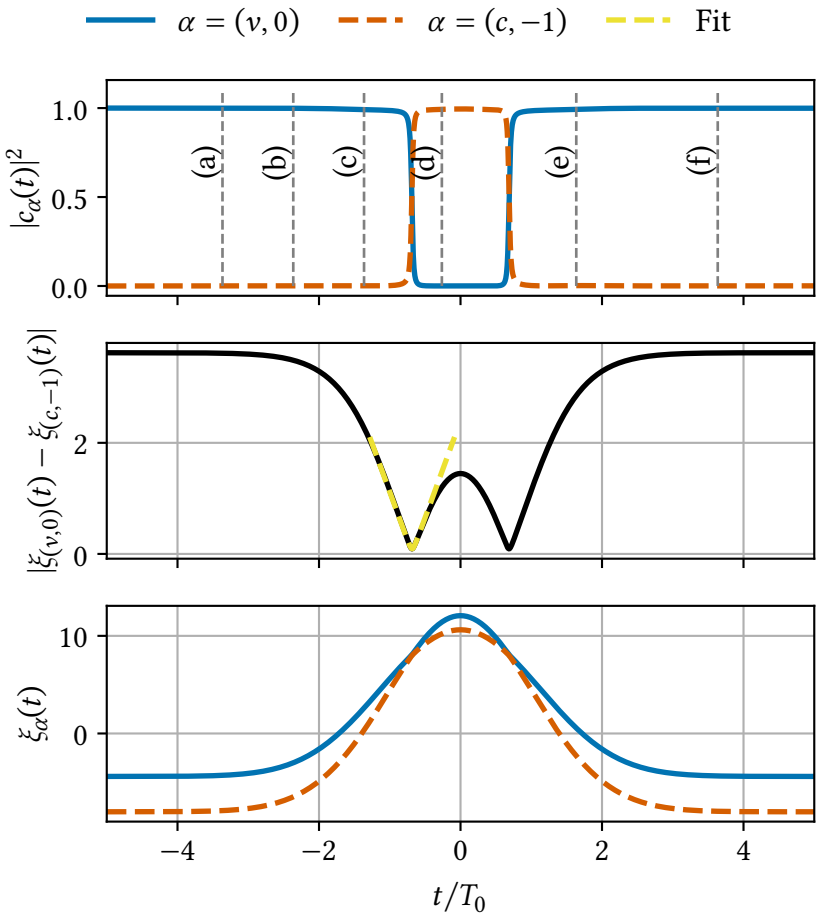


Figure 4.5: Time dependence of exemplary Floquet coefficients (top), the quasi-energy difference (center), and the individual quasi-energies (bottom) at $\boldsymbol{\kappa} = (1.21, 0)$ (marked by vertical blue lines in Figure 4.2) for the TI model given in Equations 4.1 and 4.9 with parameters taken from Table 4.1. The driving field is given in Equation 4.3 with frequency $\Omega_0/2\pi = 38.7\,\mathrm{THz}$, duration $\Delta t = 38.8\,\mathrm{fs}$, and $E_0 = 3.11\,\mathrm{MV\,cm^{-1}}$ (all system parameters are as in Figure 4.2). Vertical dashed lines indicate the times shown in the panels of Figure 4.2. Top panel depicts coefficients of the initially occupied valence band replica (solid blue) and a first order replica of the conduction band (dashed orange). From the numerical fit (dashed yellow) in the center panel yields a Landau-Zener transition probability of $P_{LZ} = 0.997$.

4.4 Conclusions and outlook

This chapter presented an in-depth study of the buildup of Floquet sidebands in light-driven topological insulator surface states using the t–t' formalism. In particular, we analyzed the hexagonally warped Dirac surface states of Bi_2Se_3 subjected to a linearly polarized driving pulse.

Building on Ref. [3], we extended the analysis by incorporating a more realistic thermal initial state with a Fermi level chosen to match room-temperature experiments [167]. We further showed that the time evolution of the instantaneous Floquet coefficients is well described by an adiabatic picture, punctuated by isolated, nearly instantaneous population transfers of Landau-Zener type. This perspective provides a natural explanation for why even few-cycle pulses can generate pronounced Floquet sidebands, despite the fact that standard Floquet theory is strictly inapplicable—or, at best, a poor approximation—in the short-pulse regime. Importantly, this seemingly counterintuitive behavior has been directly observed in time- and angle-resolved photoemission spectroscopy (trARPES) experiments [62].

As already indicated in Section 2.7, the t–t' formalism offers several promising directions for further investigation in the context of trARPES. For instance, a more direct connection to experimentally measured ARPES spectra could be achieved by explicitly including photoemission matrix elements with Volkov final states, as discussed in Refs. [145, 169]. This extension would also enable a description of laser-assisted photoemission (LAPE) and thereby provide access to a broader range of light polarizations. Moreover, nonequilibrium Green's function approaches [56, 62, 146] are naturally compatible with the instantaneous Floquet-state picture, since the equations of motion for the lesser Green function inherit the approximate periodicity of the driven system.

5 Conclusion

Simplifying assumptions and approximations are indispensable tools in theoretical physics, particularly when dealing with complex solid-state systems. At the same time, these assumptions must be continuously re-evaluated, as physically relevant phenomena often emerge at the edge of—or beyond—the parameter regimes in which established approximations are expected to apply.

Strong-field light–matter interaction in solids is commonly interpreted using theoretical frameworks that rely on specific physical decompositions of the driven electron dynamics. In high-harmonic generation, this typically involves separating the emitted current into intraband contributions associated with acceleration within a band and interband contributions associated with coherent polarization between valence and conduction bands. Likewise, Floquet theory describes periodically driven systems in terms of well-defined quasi-energy bands, an approach that formally requires strict temporal periodicity of the driving field. While these pictures have been highly successful in explaining a broad range of experimental observations, modern attosecond experiments increasingly operate in regimes where these underlying assumptions are no longer satisfied, such as ultrashort driving pulses, strong phase-coherent dynamics, and temporally isolated transitions between bands.

The central question addressed in this thesis is therefore which aspects of coherent electron dynamics remain physically meaningful in such regimes. The results presented here demonstrate that, even beyond their nominal domains of validity, coherent structure survives and reorganizes in observable-dependent ways, leaving clear signatures in both high-harmonic generation and time-resolved photoemission spectroscopy.

The three-step model rests on even stricter assumptions, such as temporally isolated transitions between bands. The results presented here show that this picture breaks down for small multi-photon numbers, where neither intraband nor interband contributions alone determine the spectrum. Instead, the emitted signal is governed by their coherent interference, which can lead to a pronounced suppression of high-frequency radiation. We show that this nonperturbative interference effect is inherently multi-scale, involving qualitatively different behavior across the Brillouin zone. By identifying the multi-photon number as the relevant control parameter and carefully analyzing the competing scales, this complex interference

phenomenon can nevertheless be reduced to an effective one-dimensional model describing modes near the Dirac point. This reduced description supports a simple analytical approximation in the small-multi-photon-number regime, which reveals that the dominant modes follow diabatic rather than adiabatic states. As a result, the system's current closely tracks the driving field and therefore lacks high-harmonic components. The interference of interband and intraband contributions can then be concisely summarized by the analytical expressions

$$j_x^{\text{intra}}(\tau, \kappa_y = 0) \approx -\frac{\zeta}{4\pi}\left[a(\tau) - \frac{M}{\zeta}\arctan\left(\frac{\zeta}{M}a(\tau)\right)\right],$$
$$j_x^{\text{inter}}(\tau, \kappa_y = 0) \approx -\frac{M}{4\pi}\arctan\left(\frac{\zeta}{M}a(\tau)\right),$$

which makes the cancellation between the two contributions explicit.

The survival of coherent dynamics is further underscored by the role of dephasing, which lifts the suppression and induces re-entrant harmonics with characteristic scaling behavior. From an experimental perspective, these effects suggest that external control parameters such as temperature or resonant photo-doping can be used to probe the underlying interference mechanism, although a quantitative extraction of microscopic dephasing processes requires careful modeling beyond the scope of this work.

A complementary manifestation of coherent dynamics beyond formal limits is provided by the buildup of Floquet sidebands in ultrafast photoemission, as discussed in Chapter 4. Floquet theory is conventionally formulated for strictly periodic driving and describes the system in terms of time-independent quasi-energy bands, an assumption that is formally violated in the few-cycle pulse regime relevant for time- and angle-resolved photoemission spectroscopy. Nevertheless, the results presented here show that essential elements of Floquet structure persist even under ultrashort driving pulses. Using the t–t' formalism, the driven system can be described in terms of instantaneous Floquet states whose populations evolve predominantly adiabatically, with isolated Landau-Zener-type transitions occurring at avoided crossings in the extended Floquet space. This analysis clarifies why pulses that are ultrashort in the sense of attosecond science can nevertheless act as a slow parameter for the electronic dynamics, thereby allowing Floquet sidebands to form despite the absence of strict periodicity. While the treatment presented here focuses on this adiabatic mechanism and does not aim at a quantitative description of photoemission intensities, it provides a consistent physical interpretation

of experimentally observed sidebands and delineates the regime in which instantaneous Floquet concepts remain meaningful.

Viewed together, the results of Chapters 3 and 4 highlight the central role of adiabatic and nonadiabatic dynamics and their nontrivial interplay in shaping coherent strong-field responses in solids. In the context of high-harmonic generation, coherent suppression arises because a subset of driven states follows diabatic trajectories near the Dirac point, leading to a current response that remains locked to the driving field and therefore lacks high-frequency components. In ultrafast photoemission, by contrast, the relevant dynamics is predominantly adiabatic in an extended Floquet space, with occasional nonadiabatic transitions that redistribute population between instantaneous quasi-energy states and give rise to sidebands. While these behaviors appear qualitatively different at the level of observables, they reflect the same underlying competition between adiabatic following and diabatic transitions in driven electronic systems, manifested through different experimental probes.

Taken together, these results emphasize that the breakdown of formal theoretical assumptions does not imply a loss of physical structure, but rather a change in how that structure is most transparently described. In both high-harmonic generation and ultrafast photoemission, coherent electron dynamics remain well organized even when standard pictures such as additive current decompositions or strict Floquet periodicity no longer apply. The appropriate description in such regimes is therefore not determined by formal validity alone, but by which representation most clearly exposes the surviving structure of the driven system.

Attosecond experiments in solids place theoretical descriptions under exceptional stress, as they deliberately probe regimes where simplifying assumptions are no longer guaranteed. The results presented here show that such regimes are not characterized by the absence of structure, but by a reorganization of coherent dynamics that depends on the observable and the chosen representation. In this sense, attosecond science serves not only as a tool for time-resolved measurement, but also as a stringent test of how robust our theoretical concepts remain when pushed beyond their formal limits.

Appendix

A

Model comparison for ZnO

In the following we give the details for a two-band model incorporating the lowest conduction band and the crystal field split valence band of ZnO. Furthermore, we compare its band structure and dipole strength to the one-dimensional Hamiltonian used as an example in Section 2.6. The 3d model for ZnO or slight variations of it are discussed in several studies, see [37, 39, 40, 135–138]. For each direction $i \in \{x, y, z\}$ the valence ($n = v$) and conduction ($n = c$) bands are given by

$$E_n(\boldsymbol{k}) = E_{n,x}(k_x) + E_{n,y}(k_y) + E_{n,z}(k_z) \tag{A.1a}$$

$$E_{v,i}(k_i) = \sum_j \alpha_{v,i}^{(j)} \cos(j k_i a_i) \tag{A.1b}$$

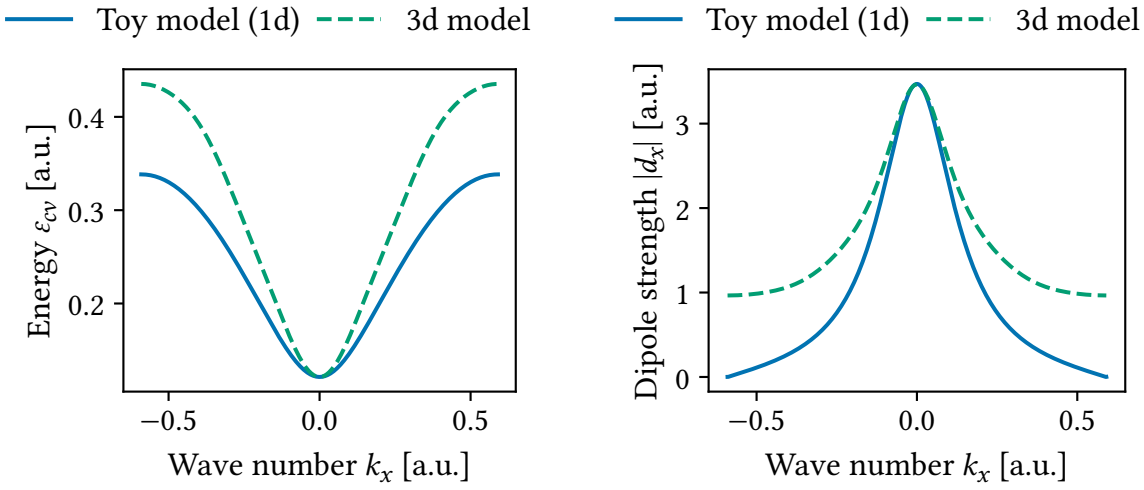
$$E_{c,i}(k_i) = \frac{E_g}{3} + \sum_j \alpha_{c,i}^{(j)} \cos(j k_i a_i) \tag{A.1c}$$

with the band gap $E_g = 0.121\,\text{a.u.} = 3.30\,\text{eV}$ and the coefficients $\alpha_{n,i}^{(j)}$ shown in Table A.1.

The coordinate system for this example is chosen so that $\boldsymbol{e}_x \parallel \Gamma - M$, $\boldsymbol{e}_y \parallel \Gamma - K$, and $\boldsymbol{e}_z \parallel \Gamma - A$; along these directions the lattice constants of ZnO are $(a_x, a_y, a_z) = (5.21, 6.14, 9.83)\,\text{a.u.}$. The dipoles

$$\boldsymbol{D}_{cv}(\boldsymbol{k}) \approx \frac{1}{\sqrt{2}(E_c(\boldsymbol{k}) - E_v(\boldsymbol{k}))} \begin{pmatrix} \sqrt{E_{p,x}} \\ \sqrt{E_{p,y}} \\ \sqrt{E_{p,z}} \end{pmatrix} \tag{A.2}$$

are obtained from $\boldsymbol{k}\cdot\boldsymbol{p}$ theory in terms of the Kane parameters $E_{p,x} = E_{p,y} = 0.353\,\text{a.u.}$ and $E_{p,z} = 0.375\,\text{a.u.}$ (see [37, 40]). Our choice of $t = 0.145\,\text{a.u.}$ in Equation 2.75 ensures that the dipole strength $|\boldsymbol{D}_{cv}|$ matches Equation A.2. The diagonal dipole matrix elements vanish for both models.



(a) Energy difference of the conduction and valence bands ε_{cv} in reciprocal space.

(b) Absolute value of the dipole coupling $\boldsymbol{D}_{cv}$ in x-direction in terms of the wavenumber k_x.

Figure A.1: Comparison of the one-dimensional toy Hamiltonian (solid blue) defined in Equation 2.75 and a more realistic model for ZnO (dashed green) with bands and dipoles given in Equation A.1 and Equation A.2 respectively. Here the x-axis of the Brillouin zone's coordinate system is parallel to the $\Gamma - M$ direction of the crystal.

Figure A.1 shows a comparison of the conduction and valence band energy difference (Figure A.1a) and the dipole strength (Figure A.1b) for the one-dimensional model, Equation 2.75, and the more realistic ZnO model, Equations A.1 and A.2. In the vicinity of $\boldsymbol{k} = 0$ both variants quantitatively agree, but towards the Brillouin zone edge there are substantial deviations. While the dipole of the one-dimensional Hamiltonian exhibits a zero at the BZ edge, the more realistic model does not.

Table A.1: Expansion coefficients $\alpha_{j,i}^{(v)}$ and $\alpha_{j,i}^{(c)}$ for the valence (v) and conduction (c) bands used in Equation A.1. Coefficients are given for the x direction (left) and for the y and z directions (right). All values are in atomic units.

Coefficient	Value	Coefficient	Value
$\alpha_{0,x}^{(v)}$	-0.0928	$\alpha_{0,y}^{(v)}$	-0.0307
$\alpha_{1,x}^{(v)}$	0.0705	$\alpha_{1,y}^{(v)}$	0.0307
$\alpha_{2,x}^{(v)}$	0.0200	$\alpha_{0,z}^{(v)}$	-0.0059
$\alpha_{3,x}^{(v)}$	-0.0012	$\alpha_{1,z}^{(v)}$	0.0059
$\alpha_{4,x}^{(v)}$	0.0029		
$\alpha_{5,x}^{(v)}$	0.0006		
$\alpha_{0,x}^{(c)}$	0.0898	$\alpha_{0,y}^{(c)}$	0.1147
$\alpha_{1,x}^{(c)}$	-0.0814	$\alpha_{1,y}^{(c)}$	-0.1147
$\alpha_{2,x}^{(c)}$	-0.0024	$\alpha_{0,z}^{(c)}$	0.0435
$\alpha_{3,x}^{(c)}$	-0.0048	$\alpha_{1,z}^{(c)}$	-0.0435
$\alpha_{4,x}^{(c)}$	-0.0003		
$\alpha_{5,x}^{(c)}$	-0.0009		

B

A second suppression ratio

Here we present an additional figure of merit for coherent suppression that augments R defined in Equation 3.17. The ratio

$$R_2 = \left\langle I^{\text{inter}} / I \right\rangle_\omega \tag{B.1}$$

measures how "interband-dominated" the total emission intensity I is. The average $\langle \ldots \rangle_\omega$ in Equation B.1 includes all frequencies above the (numerical) noise threshold (see Appendix D). Figure B.1 shows the ratio R_2 for

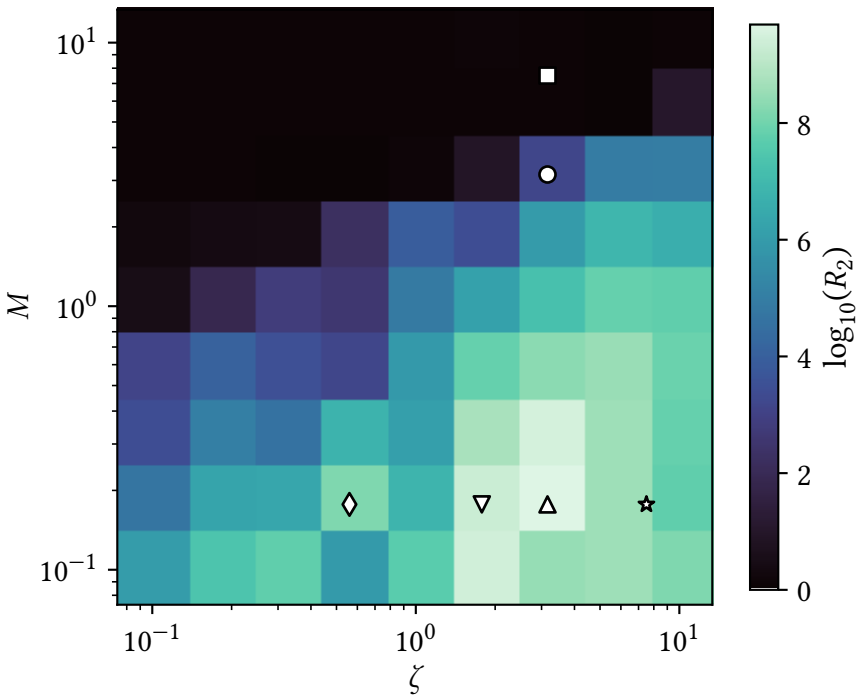


Figure B.1: Ratio R_2 from Equation B.1 for the massive Dirac model with driving field given in Equation 3.4 and $\sigma = 1.5\,\tau_0$ for and for vanishing dephasing ($\tau_2 \to \infty$). The multi-photon numbers M and strong-field parameters ζ are taken from Equation 3.15, i.e. we show data from the same simulations as in Figure 3.6. Spectral instensity with inter- and intraband decompositions for parameters at the markers are shown in Figure 3.5.

the massive Dirac system with multi-photon number M and strong-field parameters ζ taken from Equation 3.15. In the regions where R_2 is close

to one the HHG emission is dominated by the interband contribution, whereas for large R_2 the total spectral yield lies significantly below the interband emission. Bright areas in Figure B.1 are therefore synonymous with coherent suppression, if they are also bright in Figure 3.6. As a result Figure B.1 proves our statement in Section 3.2 that no constructive interference occurs anywhere in the presented parameter range and all bright areas in Figure 3.6 correspond to coherent suppression.

C

Description of open-source code

All numerical simulations of the SBE in [2] and this thesis employed our fully-parallelized, GPU-enabled software `Damysos.jl` [170]. In this appendix we outline some of the features and numerical strategies used in this software. There source code with documentation additionally features instructions on how to reproduce the simulations performed in this work [170].

C.1 Modular nature

At the heart of our software is the `Simulation` object which holds the physical system and the time and $\boldsymbol{k}$-space grid used. We sketch the structure in Figure C.1: the physical system is represented by `Liouvillian`, `DrivingField`, and `UnitScaling` (defines length and time scale, see Section 2.4). `NGrid` holds the time and $\boldsymbol{k}$-space grids used for numerical evaluation and `Vector{Observable}` contains all observables to be calculated. This modular nature of the software allows easy addition of new Hamiltonians and driving electric fields. Note that `KGrid` implicitly specifies the BZ and dimensionality of the system. Both must be compatible with the model Hamiltonian or an error is raised.

The second core element in our code consists of a solver, which determines how the ODE ensembles are solved, i.e. on GPU/CPU and with adaptive/fixed-step solvers. More on that in Section C.2 below.

The available Hamiltonians, observables, and driving fields are listed in the documentation (`https://github.com/howbgl/Damysos.jl`, cf. [170]).

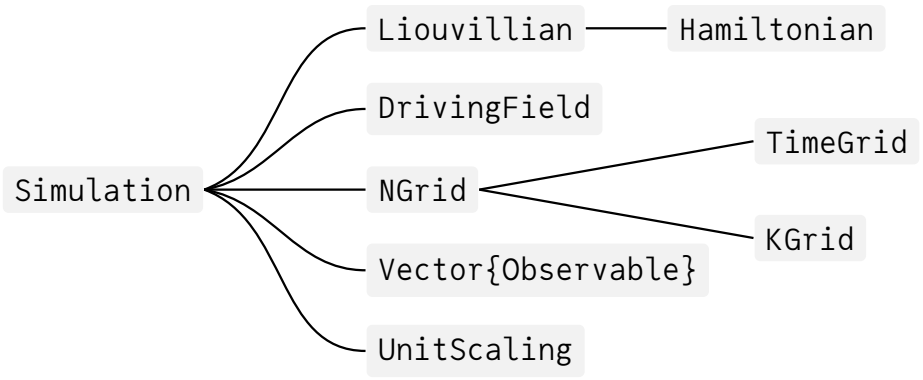


Figure C.1: Structure of the simulation object.

C.2 Parallelization

We exclusively use velocity gauge for our SBE simulations. As a result the strategy for massive parallelization is straightforward: individual wave vectors $\boldsymbol{k}$ are decoupled and the problem reduces to an ensemble of ordinary differential equations (ODEs) for the density matrix at each $\boldsymbol{k}$. We chose the Julia language for this software, because the package `DifferentialEquations.jl` is one the fastest and most feature-complete libraries for solving ODEs, see [171]. Additionally, there is GPU support via `DiffEqGPU.jl` (cf. [172]) that can be used to parallelize ensembles with little programming effort.

The principal tasks in calculating observables such as the current density Equations 2.32 and 2.50 are the following:

1. Solve the ODEs for all $\boldsymbol{k}$ (Section 2.4 and Equation 2.30).
2. Calculate the matrix elements for the desired observables, e.g. $\boldsymbol{J}_{mn}(\boldsymbol{k})$ (Equation 2.33).
3. Integrate/sum observables (Equation 2.32).

In `Damysos.jl` we currently implement three "solvers". The strategy is illustrated in Figure C.2: all $\boldsymbol{k}$-points of the grid are grouped into chunks, which can be processed independently. We currently provide three solvers:

1. `LinearChunked`: linear indexing on CPUs, multithreaded and distributed
2. `LinearCUDA`: linear indexing on GPUs, multi-GPU support and automated memory estimate
3. `SingleMode`: performs no integration, calculates observables at a single $\boldsymbol{k}$-point (velocity gauge)

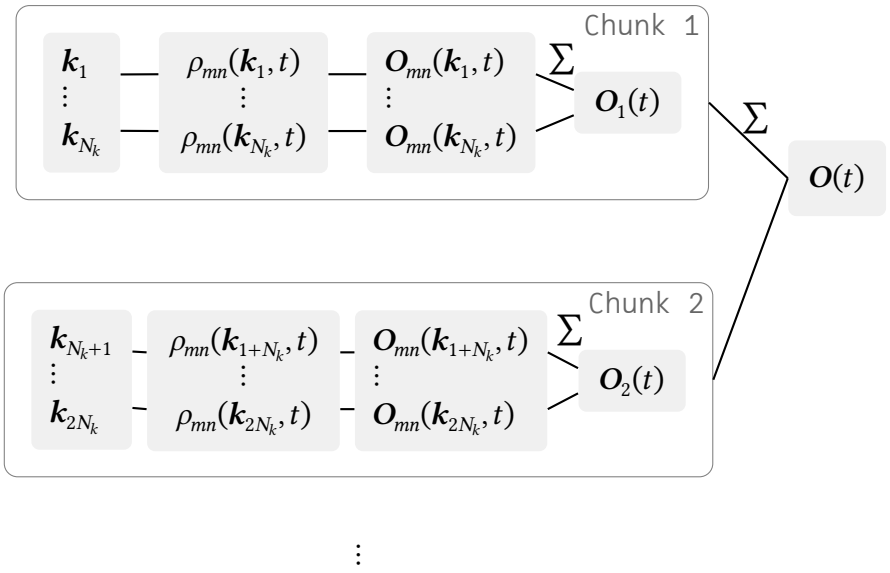


Figure C.2: Schematic of the numerical solution strategy implemented in [170]. The discretized $\boldsymbol{k}$-space is distributed into several chunks, which are processed independently. For each element int the chunks the SBE are solved for the time dependence of the density matrix $\rho_{mn}(\boldsymbol{k}, t)$ and the matrix elements of all desired observables (collectively designated $\boldsymbol{O}_{mn}(\boldsymbol{k}, t)$ here) are calculated. First the observables are summed/integrated in each chunk and then the results combined to give the final result.

Both `LinearChunked` and `LinearCUDA` use midpoint rule to calculate the integral in $\boldsymbol{k}$-space and enumerate the $\boldsymbol{k}$-points "linearly" as opposed to subdividing the integration region into tiles or slices. We chose linear indexing and midpoint rule for simplicity, but due to the modular structure one can easily add more involved strategies with adaptive subdivision or other features. The heavy lifting of ODE solving is handled by `DifferentialEquations.jl` and `DiffEqGPU.jl` utilizing their functionality to solve ensembles of ODEs with minimal overhead*. As a result it is easy to switch to any solver provided by the aforementioned packages, which can optimize runtime or memory requirements.

C.3 ODE construction

When constructing the right-hand side necessary for solving the ODEs for the density matrix we rely on the metaprogramming capabilities of Julia. Exploiting the formulas given in Section 2.5 we use Julia's `@eval` functionality to effectively teach the software to hard-code all physical

* For the CPU solver we group several $\boldsymbol{k}$-points in a single coupled ODE, because benchmarking has shown that this is faster than creating as many ensembles as $\boldsymbol{k}$-points. The slowdown for many $\boldsymbol{k}$-samples is presumably from launch overhead. We did not test this on GPUs.

parameters. This strategy has two main advantages: it sidesteps any issues that GPUs tend to have when using closures or the overhead from passing many parameters between CPU and GPU *and* it maximizes speed, because no lookup of any parameter has to be performed at runtime.

The construction is handled by the function `define_functions` which takes the simulation and solver as arguments. If new functionality is to be implemented, it may be easier to first use closures to pass functions-as-objects or other strategies to avoid metaprogramming, which can be error-prone and less readable.

C.4 Convergence testing

Every simulation with the SBE must be checked for convergence with respect to discretization. This includes the time step (or adaptive tolerances), the density of the $\boldsymbol{k}$-grid, and the initial time (the driving field must vanish there to be physical, no instant turn-on of the field). See also [45, 69, 70] for nice discussions on this.

Our software provides the `ConvergenceTest` object in order to automate such tests and also calculate reasonable error bounds. When executing such a convergence test, subsequent simulations are generated by an iterator method (linear or power-law available). For more details confer with the documentation of `Damysos.jl`. The procedure is stopped if specified relative and absolute errors are satisfied, if a timer runs out, or if a maximum number of iterations is used. The latter two criteria can also be disabled.

The errors are calculated via Richardson extrapolation [173]. We note that usually these errors are quite pessimistic, especially when checking the time step. Automated plotting of time traces and HHG spectra is also provided, so one can easily confirm the accuracy by inspection.

D

On numerical noise

Here we briefly explain the term "noise level" and its importance for HHG spectra calculated numerically from the SBE. In every numerical calculation carried out with floating-point arithmetic (IEEE 754) errors play a role [174]. The fixed number of decimals are only an approximation which can catastrophically fail especially for addition and subtraction like it is required when approximating integrals. A crucial role is played by the specific implementation of sums: naive sum, pairwise reduction, or even Kahan summation [175]. Our software uses pairwise reduction as it is done in several scientific computing libraries (default for Julia and `NumPy`), which is slightly worse than Kahan in precision but much faster as it be easily parallelized (divide-and-conquer).

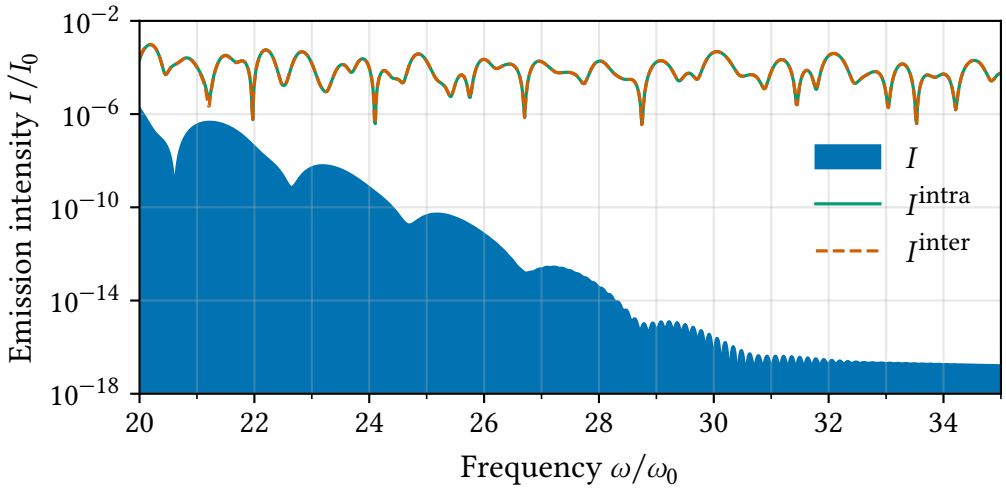


Figure D.1: Total frequency-resolved emission intensity $I(\omega)$ (Equation 2.54), shaded blue) compared to intraband (solid green line) and interband (dashed orange line) contributions according to Equation 3.13 for the massive Dirac model (Equation 3.6) with $\zeta = 10$ and $M = 0.56$.Here, no dephasing ($\tau_2 \to \infty$) and the driving field given in Equation 3.4 with $\sigma = 1.5\,\tau_0$ are used. We show how the numerical noise level for I is reached somewhere between the 16th and 27th harmonic.

The consequence of rounding errors due to floating-point arithmetic is especially visible in HHG spectra*, because the intensity varies over many

* The noise level of HHG spectra is also discussed in [70].

orders of magnitude. At some point the numbers are too small to be accurately resolved by double precision. This failure is clearly visible in Figure D.1, where an exemplary spectrum is shown to break down between the 16th and 27th harmonic (total intensity $I(\omega)$). The precise location varies with system parameters and implementation and is very hard to predict. An authoritative statement about the exact accuracy can only be made by using a higher precision e.g. with quadruple-precision floating-point numbers or with arbitrary precision (`BigFloat` in Julia) arithmetic. Any high-accuracy method comes with enormous runtime cost. Withing this work, the precision provided by regular floating-point arithmetic is more than enough, since many orders of magnitude can be resolved.

In the context of the suppression ratio R (Equation 3.17) studied in Chapter 3 we adopted the following pragmatic strategy: when calculating R we only include those frequencies where the largest and smallest intensities differ only by a certain threshold factor. This threshold is tuned such that for no spectrum included visible noise (like in Figure D.1) enters the average by inspecting the spectrum for all data points shown in Figure 3.6.

Data Availability

The data that support the findings of this article are openly available [170, 176].

Bibliography

Here are the references in citation order.

[1] Ludwig Wittgenstein. *Tractatus logico-philosophicus*. The German text of Ludwig Wittgenstein's Logisch-philosophische Abhandlung translated by D.F. Pears & B.F. McGuinness and with an introduction by Bertrand Russell. London, England: Routledge & Kegan Paul, 1961 [1921] (cited on page iii).

[2] Wolfgang Hogger et al. "Coherent suppression and dephasing-induced reentrance of high harmonics in gapped Dirac materials." In: *Phys. Rev. B* 113.4 (Jan. 2026), p. 045418. DOI: 10.1103/4gwm-9lpy (cited on pages vii, 5, 40, 47, 48, 50, 53, 65, 66, 95).

[3] Yuriko Baba et al. "Radiation-induced dynamical formation of Floquet-Bloch bands in Dirac Hamiltonians." In: *New J. Phys.* 27.4 (Apr. 2025), p. 043015. DOI: 10.1088/1367-2630/ADC594 (cited on pages vii, 6, 34–37, 71, 74, 75, 77, 81).

[4] Pierre Agostini and Louis F. DiMauro. "The physics of attosecond light pulses." In: *Rep. Prog. Phys.* 67.8 (Aug. 2004), p. 1563. DOI: 10.1088/0034-4885/67/8/C01 (cited on page 1).

[5] *The Nobel Prize in Physics 2023 - Scientific background - NobelPrize.org*. URL: https://www.nobelprize.org/prizes/physics/2023/advanced-information/ (cited on page 1).

[6] Ferenc Krausz and Misha Ivanov. "Attosecond physics." In: *Rev. Mod. Phys.* 81.1 (Feb. 2009), p. 163. DOI: 10.1103/RevModPhys.81.163 (cited on pages 1, 25).

[7] P. B. Corkum and Ferenc Krausz. "Attosecond science." In: *Nat. Phys.* 3.6 (2007), pp. 381–387. DOI: 10.1038/nphys620 (cited on page 1).

[8] M. Ferray et al. "Multiple-harmonic conversion of 1064 nm radiation in rare gases." In: *J. Phys. B* 21.3 (Feb. 1988), p. L31. DOI: 10.1088/0953-4075/21/3/001 (cited on page 1).

[9] T. W. Hänsch. "A proposed sub-femtosecond pulse synthesizer using separate phase-locked laser oscillators." In: *Opt. Commun.* 80.1 (Dec. 1990), pp. 71–75. DOI: 10.1016/0030-4018(90)90509-R (cited on page 1).

[10] Gy Farkas and Cs Tóth. "Proposal for attosecond light pulse generation using laser induced multiple-harmonic conversion processes in rare gases." In: *Phys. Lett. A* 168.5-6 (Sept. 1992), pp. 447–450. DOI: 10.1016/0375-9601(92)90534-S (cited on page 1).

[11] S. E. Harris, J. J. Macklin, and T. W. Hänsch. "Atomic scale temporal structure inherent to high-order harmonic generation." In: *Opt. Commun.* 100.5-6 (July 1993), pp. 487–490. DOI: 10.1016/0030-4018(93)90250-9 (cited on page 1).

[12] Anne L. Huillier, Kenneth J. Schafer, and Kenneth C. Kulander. "Theoretical aspects of intense field harmonic generation." In: *J. Phys. B* 24.15 (Aug. 1991), p. 3315. DOI: 10.1088/0953-4075/24/15/004 (cited on page 1).

[13] P B Corkum. "Plasma perspective on strong field multiphoton ionization." In: *Phys. Rev. Lett.* 71.13 (Sept. 1993), pp. 1994–1997. DOI: 10.1103/PhysRevLett.71.1994 (cited on page 1).

[14] M Lewenstein et al. "Theory of high-harmonic generation by low-frequency laser fields." In: *Phys. Rev. A* 49.3 (Feb. 1994), p. 2117. DOI: 10.1103/PhysRevA.49.2117 (cited on pages 2, 8, 25, 28, 67).

[15] M. Hentschel et al. "Attosecond metrology." In: *Nature* 414.6863 (Nov. 2001), pp. 509–513. DOI: 10.1038/35107000 (cited on pages 2, 25).

[16] E. Goulielmakis et al. "Single-cycle nonlinear optics." In: *Science* 320.5883 (June 2008), pp. 1614–1617. DOI: 10.1126/SCIENCE.1157846 (cited on page 2).

[17] J. Itatani et al. "Attosecond Streak Camera." In: *Phys. Rev. Lett.* 88.17 (Apr. 2002), p. 173903. DOI: 10.1103/PhysRevLett.88.173903 (cited on pages 2, 25).

[18] P. M. Paul et al. "Observation of a Train of Attosecond Pulses from High Harmonic Generation." In: *Science* 292.5522 (June 2001), pp. 1689–1692. DOI: 10.1126/SCIENCE.1059413 (cited on pages 2, 25).

[19] S Ghimire et al. "Observation of high-order harmonic generation in a bulk crystal." In: *Nat. Phys.* 7 (Feb. 2011), pp. 138–141. DOI: https://doi.org/10.1038/nphys1847 (cited on page 2).

[20] Shambhu Ghimire et al. "Strong-field and attosecond physics in solids." In: *J. Phys. B* 47.20 (Oct. 2014), p. 204030. DOI: 10.1088/0953-4075/47/20/204030 (cited on page 2).

[21] O. Schubert et al. “Sub-cycle control of terahertz high-harmonic generation by dynamical Bloch oscillations.” In: *Nat. Photonics* 8.2 (Jan. 2014), pp. 119–123. DOI: 10.1038/nphoton.2013.349 (cited on pages 2, 17, 20).

[22] Shambhu Ghimire and David A. Reis. “High-harmonic generation from solids.” In: *Nat. Phys.* 15.1 (Nov. 2018), pp. 10–16. DOI: 10.1038/s41567-018-0315-5 (cited on page 2).

[23] J Reimann et al. “Subcycle observation of lightwave-driven Dirac currents in a topological surface band.” In: *Nature* 562.7727 (Sept. 2018), p. 396. DOI: 10.1038/s41586-018-0544-x (cited on page 2).

[24] F. Langer et al. “Lightwave-driven quasiparticle collisions on a subcycle timescale.” In: *Nature* 533.7602 (May 2016), pp. 225–229. DOI: 10.1038/nature17958 (cited on pages 2, 17).

[25] Ayelet Julie Uzan et al. “Attosecond spectral singularities in solid-state high-harmonic generation.” In: *Nat. Photonics* 14.3 (Jan. 2020), pp. 183–187. DOI: 10.1038/s41566-019-0574-4 (cited on page 2).

[26] Tran Trung Luu and Hans Jakob Wörner. “Measurement of the Berry curvature of solids using high-harmonic spectroscopy.” In: *Nat. Commun.* 9.1 (Mar. 2018), pp. 916–. DOI: 10.1038/s41467-018-03397-4 (cited on page 2).

[27] F. Langer et al. “Symmetry-controlled temporal structure of high-harmonic carrier fields from a bulk crystal.” In: *Nat. Photonics* 11.4 (Mar. 2017), pp. 227–231. DOI: 10.1038/nphoton.2017.29 (cited on page 2).

[28] F. Langer et al. “Lightwave valleytronics in a monolayer of tungsten diselenide.” In: *Nature* 557.7703 (May 2018), pp. 76–80. DOI: 10.1038/s41586-018-0013-6 (cited on page 2).

[29] Ofer Neufeld, Daniel Podolsky, and Oren Cohen. “Floquet group theory and its application to selection rules in harmonic generation.” In: *Nat. Commun.* 10.1 (Jan. 2019), pp. 405–. DOI: 10.1038/s41467-018-07935-y (cited on page 2).

[30] Hanzhe Liu et al. “High-harmonic generation from an atomically thin semiconductor.” In: *Nat. Phys.* 13.3 (Feb. 2016), pp. 262–265. DOI: 10.1038/nphys3946 (cited on page 2).

[31] R. E.F. Silva et al. “High-harmonic spectroscopy of ultrafast many-body dynamics in strongly correlated systems.” In: *Nat. Photonics* 12.5 (Mar. 2018), pp. 266–270. DOI: 10.1038/s41566-018-0129-0 (cited on page 2).

[32] Nicolas Tancogne-Dejean, Michael A. Sentef, and Angel Rubio. "Ultrafast Modification of Hubbard U in a Strongly Correlated Material: Ab initio High-Harmonic Generation in NiO." In: *Phys. Rev. Lett.* 121.9 (Aug. 2018), p. 097402. DOI: 10.1103/PhysRevLett.121.097402 (cited on page 2).

[33] Ofer Neufeld et al. "Are There Universal Signatures of Topological Phases in High-Harmonic Generation Probably Not." In: *Phys. Rev. X* 13.3 (July 2023), p. 031011. DOI: 10.1103/PHYSREVX.13.031011 (cited on page 2).

[34] Denitsa Baykusheva et al. "Strong-field physics in three-dimensional topological insulators." In: *Phys. Rev. A* 103.2 (Feb. 2021), p. 23101. DOI: 10.1103/PhysRevA.103.023101 (cited on pages 2, 7, 17).

[35] Denitsa Baykusheva et al. "All-Optical Probe of Three-Dimensional Topological Insulators Based on High-Harmonic Generation by Circularly Polarized Laser Fields." In: *Nano Lett.* 21.21 (Nov. 2021), pp. 8970–8978. DOI: 10.1021/ACS.NANOLETT.1C02145 (cited on page 2).

[36] Christian Heide et al. "Probing topological phase transitions using high-harmonic generation." In: *Nat. Photonics* 16.9 (Aug. 2022), pp. 620–624. DOI: 10.1038/s41566-022-01050-7 (cited on pages 2, 42, 69).

[37] G Vampa et al. "Theoretical analysis of high-harmonic generation in solids." In: *Phys. Rev. Lett.* 113.7 (Feb. 2014), p. 73901. DOI: 10.1103/PhysRevLett.113.073901 (cited on pages 3, 7, 8, 17, 19, 20, 25–30, 67, 89).

[38] G. Vampa et al. "Linking high harmonics from gases and solids." In: *Nature* 522.7557 (June 2015), pp. 462–464. DOI: 10.1038/nature14517 (cited on page 3).

[39] G Vampa et al. "Semiclassical analysis of high harmonic generation in bulk crystals." In: *Phys. Rev. B* 91.6 (Feb. 2015), p. 64302. DOI: 10.1103/PhysRevB.91.064302 (cited on pages 3, 7, 8, 17, 20, 25, 26, 28–31, 42, 89).

[40] Giulio Vampa. "Role of Electron-Hole Recollisions in High Harmonic Generation from Bulk Crystals." PhD thesis. University of Ottawa, 2016. DOI: 10.20381/ruor-6145 (cited on pages 3, 29, 31, 89).

[41] Lun Yue and Mette B Gaarde. "Imperfect Recollisions in High-Harmonic Generation in Solids." In: *Phys. Rev. Lett.* 124.15 (2020), pp. 1–7. DOI: 10.1103/PhysRevLett.124.153204 (cited on pages 3, 7, 8, 17, 20, 24–26, 30, 31, 42).

[42] Lun Yue and Mette B Gaarde. "Expanded view of electron-hole recollisions in solid-state high-order harmonic generation: Full-Brillouin-zone tunneling and imperfect recollisions." In: *Phys. Rev. A* 103.6 (Feb. 2021), p. 63105. DOI: 10.1103/PhysRevA.103.063105 (cited on pages 3, 7, 8, 17, 20, 25, 26, 30, 31, 42).

[43] A. M. Parks et al. "Wannier quasi-classical approach to high harmonic generation in semiconductors." In: *Optica* 7.12 (Dec. 2020), pp. 1764–1772. DOI: 10.1364/OPTICA.402393 (cited on pages 3, 8, 25).

[44] Liang Li et al. "Huygens-Fresnel Picture for High Harmonic Generation in Solids." In: *Phys. Rev. Lett.* 127.22 (Nov. 2021), p. 223201. DOI: 10.1103/PHYSREVLETT.127.223201 (cited on page 3).

[45] Jan Wilhelm et al. "Semiconductor Bloch-equations formalism: Derivation and application to high-harmonic generation from Dirac fermions." In: *Phys. Rev. B* 103.12 (Feb. 2021), p. 125419. DOI: 10.1103/PHYSREVB.103.125419 (cited on pages 3, 5, 7, 15–20, 45, 68, 98).

[46] Yuta Murakami and Michael Schüler. "Doping and gap size dependence of high-harmonic generation in graphene: Importance of consistent formulation of light-matter coupling." In: *Phys. Rev. B* 106.3 (Feb. 2022), p. 35204. DOI: 10.1103/PhysRevB.106.035204 (cited on pages 3, 5, 20, 45, 68).

[47] Jonathan A. Sobota, Yu He, and Zhi Xun Shen. "Angle-resolved photoemission studies of quantum materials." In: *Rev. Mod. Phys.* 93.2 (May 2021), p. 025006. DOI: 10.1103/RevModPhys.93.025006 (cited on page 3).

[48] Andrea Damascelli, Zahid Hussain, and Zhi Xun Shen. "Angle-resolved photoemission studies of the cuprate superconductors." In: *Rev. Mod. Phys.* 75.2 (Apr. 2003), p. 473. DOI: 10.1103/RevModPhys.75.473 (cited on page 3).

[49] Stefan Hüfner, Stefan Schmidt, and Friedrich Reinert. "Photoelectron spectroscopy—An overview." In: *Nucl. Instrum. Methods Phys. Res. A* 547.1 (July 2005), pp. 8–23. DOI: 10.1016/J.NIMA.2005.05.008 (cited on page 3).

[50] Stefan. Hüfner. *Photoelectron spectroscopy : principles and applications*. Springer, 2011 (cited on page 3).

[51] Fabio Boschini, Marta Zonno, and Andrea Damascelli. "Time-resolved ARPES studies of quantum materials." In: *Rev. Mod. Phys.* 96.1 (Jan. 2024), p. 015003. DOI: 10.1103/REVMODPHYS.96.015003 (cited on page 3).

[52] L. Perfetti et al. "Ultrafast Electron Relaxation in Superconducting $Bi_2Sr_2CaCu_2O_{8+\delta}$ by Time-Resolved Photoelectron Spectroscopy." In: *Phys. Rev. Lett.* 99.19 (Nov. 2007), p. 197001. DOI: 10.1103/PhysRevLett.99.197001 (cited on page 4).

[53] Christopher L. Smallwood et al. "Tracking Cooper pairs in a cuprate superconductor by ultrafast angle-resolved photoemission." In: *Science* 336.6085 (June 2012), pp. 1137–1139. DOI: 10.1126/SCIENCE.1217423 (cited on page 4).

[54] A. L. Cavalieri et al. "Attosecond spectroscopy in condensed matter." In: *Nature* 449.7165 (Oct. 2007), pp. 1029–1032. DOI: 10.1038/nature06229 (cited on page 4).

[55] Y H Wang et al. "Observation of Floquet-Bloch States on the Surface of a Topological Insulator." In: *Science* 342.6157 (Oct. 2013), p. 453. DOI: 10.1126/science.1239834 (cited on pages 4, 34).

[56] Fahad Mahmood et al. "Selective scattering between FloquetBloch and Volkov states in a topological insulator." In: *Nat. Phys.* 12.4 (Jan. 2016), p. 306. DOI: 10.1038/nphys3609 (cited on pages 4, 6, 35, 75, 81).

[57] M Lindberg and S W Koch. "Effective Bloch equations for semiconductors." In: *Phys. Rev. B* 38.5 (Feb. 1988), p. 3342. DOI: 10.1103/PhysRevB.38.3342 (cited on pages 5, 7, 15).

[58] S. Schmitt-Rink, D. S. Chemla, and H. Haug. "Nonequilibrium theory of the optical Stark effect and spectral hole burning in semiconductors." In: *Phys. Rev. B* 37.2 (Jan. 1988), p. 941. DOI: 10.1103/PhysRevB.37.941 (cited on pages 5, 7).

[59] Wilfried Schäfer and Martin Wegener. *Semiconductor Optics and Transport Phenomena*. 1st ed. Springer Berlin, 2002 (cited on pages 5, 7, 15–17, 19).

[60] Hartmut Haug and Stephan W Koch. *Quantum Theory of the Optical and Electronic Properties of Semiconductors*. WORLD SCIENTIFIC, Feb. 2004 (cited on pages 5, 7, 15).

[61] Mackillo Kira and Stephan W. Koch. *Semiconductor Quantum Optics*. Cambridge: Cambridge University Press, Nov. 2011 (cited on pages 5, 7, 15, 17).

[62] S Ito et al. "Build-up and dephasing of FloquetBloch bands on subcycle timescales." In: *Nature* 616.7958 (Apr. 2023), p. 696. DOI: 10.1038/s41586-023-05850-x (cited on pages 6, 35, 81).

[63] M. Hohenleutner et al. "Real-time observation of interfering crystal electrons in high-harmonic generation." In: *Nature* 523.7562 (July 2015), pp. 572–575. DOI: 10.1038/nature14652 (cited on pages 7, 17, 20).

[64] C P Schmid et al. "Tunable non-integer high-harmonic generation in a topological insulator." In: *Nature* 593.7859 (2021), pp. 385–390. DOI: 10.1038/s41586-021-03466-7 (cited on pages 7, 17, 42).

[65] Isabella Floss et al. "Ab initio multiscale simulation of high-order harmonic generation in solids." In: *Phys. Rev. A* 97.1 (Jan. 2018), p. 011401. DOI: 10.1103/PHYSREVA.97.011401 (cited on pages 7, 15, 16, 18).

[66] Isabella Floss et al. "Incorporating decoherence into solid-state time-dependent density functional theory." In: *Phys. Rev. B* 99.22 (June 2019), p. 224301. DOI: 10.1103/PHYSREVB.99.224301 (cited on pages 7, 18).

[67] D. Golde, T. Meier, and S. W. Koch. "High harmonics generated in semiconductor nanostructures by the coupled dynamics of optical inter- and intraband excitations." In: *Phys. Rev. B* 77.7 (Feb. 2008), p. 075330. DOI: 10.1103/PHYSREVB.77.075330 (cited on pages 7, 19).

[68] Maximilian Graml et al. "Influence of chirp and carrier-envelope phase on noninteger high-harmonic generation." In: *Phys. Rev. B* 107.5 (Feb. 2023), p. 54305. DOI: 10.1103/physrevb.107.054305 (cited on page 7).

[69] Adrian Seith, Ferdinand Evers, and Jan Wilhelm. "Giant DC-like residual current generated by subcycle laser pulses." In: *Phys. Rev. Res.* 6.4 (Oct. 2024), p. 043149. DOI: 10.1103/PhysRevResearch.6.043149 (cited on pages 7, 25, 75, 98).

[70] Adrian Seith. "Understanding ultrafast lightwave driven electron dynamics - a joint analytical and computational approach." PhD thesis. Regensburg, 2025 (cited on pages 7, 15, 17–19, 23, 25, 75, 98, 99).

[71] Lun Yue and Mette B. Gaarde. "Introduction to theory of high-harmonic generation in solids: tutorial." In: *J. Opt. Soc. Am. B* 39.2 (Feb. 2022), pp. 535–555. DOI: 10.1364/JOSAB.448602 (cited on pages 7, 8, 16, 20, 25, 26).

[72] MacIej Lewenstein, Pascal Salières, and Anne Lhuillier. "Phase of the atomic polarization in high-order harmonic generation." In: *Phys. Rev. A* 52.6 (Dec. 1995), p. 4747. DOI: 10.1103/PhysRevA.52.4747 (cited on pages 8, 25).

[73] G. Floquet. "Sur les équations différentielles linéaires à coefficients périodiques." In: *Ann. Sci. Éc. Norm. Sup.* 12 (1883), pp. 47–88. DOI: 10.24033/ASENS.220 (cited on pages 8, 33).

[74] Jon H Shirley. "Solution of the Schrödinger Equation with a Hamiltonian Periodic in Time." In: *Phys. Rev.* 138.4B (May 1965), B979. DOI: 10.1103/physrev.138.b979 (cited on pages 8, 33).

[75] Hideo Sambe. "Steady States and Quasienergies of a Quantum-Mechanical System in an Oscillating Field." In: *Phys. Rev. A* 7.6 (June 1973), p. 2203. DOI: 10.1103/PhysRevA.7.2203 (cited on pages 8, 35).

[76] Uri Peskin and Nimrod Moiseyev. "The solution of the time-dependent Schrödinger equation by the (t, t′) method: Theory, computational algorithm and applications." In: *J. Chem. Phys.* 99.6 (1993), p. 4590 (cited on pages 8, 35).

[77] Milena Grifoni and Peter Hänggi. "Driven quantum tunneling." In: *Phys. Rep.* 304.5 (1998), p. 229. DOI: https://doi.org/10.1016/S0370-1573(98)00022-2 (cited on pages 8, 35).

[78] K Drese and M Holthaus. "Floquet theory for short laser pulses." In: *Eur. Phys. J. D* 5.1 (Jan. 1999), p. 119. DOI: 10.1007/s100530050236 (cited on pages 8, 35).

[79] Martin Holthaus. "Floquet engineering with quasienergy bands of periodically driven optical lattices." In: *Eur. Phys. J. B* 49.1 (Nov. 2015), p. 13001. DOI: 10.1088/0953-4075/49/1/013001 (cited on pages 8, 35).

[80] Tatsuhiko N. Ikeda, Satoshi Tanaka, and Yosuke Kayanuma. "Floquet-Landau-Zener interferometry: Usefulness of the Floquet theory in pulse-laser-driven systems." In: *Phys. Rev. Res.* 4.3 (July 2022), p. 033075. DOI: 10.1103/PhysRevResearch.4.033075 (cited on pages 8, 35, 37).

[81] M. Born and R. Oppenheimer. "Zur Quantentheorie der Molekeln." In: *Ann. Phys.* 389.20 (Jan. 1927), pp. 457–484. DOI: 10.1002/ANDP.19273892002 (cited on page 8).

[82] A Messiah. *Quantum Mechanics*. Quantum Mechanics Bd. 2. Elsevier Science, 1981 (cited on pages 8, 9, 25).

[83] M. Born and V. Fock. "Beweis des Adiabatensatzes." In: *Z. Phys.* 51.3-4 (Mar. 1928), pp. 165–180 (cited on page 9).

[84] M V Berry and Proc R Soc Lond A. "Quantal phase factors accompanying adiabatic changes." In: *Proc. R. Soc. A* 392.1802 (1984), pp. 45–57. DOI: 10.1098/rspa.1984.0023 (cited on pages 9, 26, 37).

[85] D J Thouless et al. "Quantized Hall Conductance in a Two-Dimensional Periodic Potential." In: *Phys. Rev. Lett.* 49.6 (Aug. 1982), pp. 405–408. DOI: 10.1103/physrevlett.49.405 (cited on page 10).

[86] Robert Karplus and J. M. Luttinger. "Hall Effect in Ferromagnetics." In: *Phys. Rev.* 95.5 (Sept. 1954), p. 1154. DOI: 10.1103/PhysRev.95.1154 (cited on page 10).

[87] T Jungwirth, Qian Niu, and A H MacDonald. "Anomalous Hall Effect in Ferromagnetic Semiconductors." In: *Phys. Rev. Lett.* 88.20 (May 2002), p. 207208. DOI: 10.1103/physrevlett.88.207208 (cited on page 10).

[88] Naoto Nagaosa et al. "Anomalous Hall effect." In: *Rev. Mod. Phys.* 82.2 (May 2010), p. 1539. DOI: 10.1103/RevModPhys.82.1539 (cited on page 10).

[89] Di Xiao, Ming Che Chang, and Qian Niu. "Berry phase effects on electronic properties." In: *Rev. Mod. Phys.* 82.3 (2010), pp. 1959–2007. DOI: 10.1103/RevModPhys.82.1959 (cited on pages 10, 37).

[90] R. D. King-Smith and David Vanderbilt. "Theory of polarization of crystalline solids." In: *Phys. Rev. B* 47.3 (Jan. 1993), p. 1651. DOI: 10.1103/PhysRevB.47.1651 (cited on page 10).

[91] Raffaele Resta. "Macroscopic polarization in crystalline dielectrics: the geometric phase approach." In: *Rev. Mod. Phys.* 66.3 (July 1994), p. 899. DOI: 10.1103/RevModPhys.66.899 (cited on page 10).

[92] Mark H.. Holmes. *Introduction to perturbation methods*. Springer, 2013 (cited on page 10).

[93] Carl M.. Bender and Steven A.. Orszag. *Advanced Mathematical Methods for Scientists and Engineers I.* 2013 (cited on pages 10, 27, 58).

[94] Robert B.. Dingle. *Asymptotic expansions: their derivation and interpretation [by] R.B. Dingle.* Academic Press, 1973, p. 521 (cited on page 10).

[95] David Vanderbilt. *Berry Phases in Electronic Structure Theory.* Cambridge University Press, Oct. 2018 (cited on page 10).

[96] Roderick. Wong. *Asymptotic approximations of integrals.* Society for Industrial and Applied Mathematics, 2001, p. 543 (cited on pages 10, 27).

[97] Christian Heide et al. "Adiabaticity parameters for the categorization of light-matter interaction: From weak to strong driving." In: *Phys. Rev. A* 104.2 (Feb. 2021), p. 23103. DOI: 10.1103/PHYSREVA.104.023103 (cited on pages 12, 42, 51).

[98] Vanessa Junk. "Dynamics of electrons in strongly driven Dirac systems." PhD thesis. Regensburg, Apr. 2024. DOI: 10.5283/epub.55413 (cited on pages 12, 42, 51).

[99] H. Pu, S. Raghavan, and N. P. Bigelow. "Manipulating spinor condensates with magnetic fields: Stochastization, metastability, and dynamical spin localization." In: *Phys. Rev. A* 61.2 (Jan. 2000), p. 023602. DOI: 10.1103/PhysRevA.61.023602 (cited on page 12).

[100] S. Ashhab et al. "Two-level systems driven by large-amplitude fields." In: *Phys. Rev. A* 75.6 (2007), pp. 1–9. DOI: 10.1103/PhysRevA.75.063414 (cited on page 12).

[101] Oleh V. Ivakhnenko, Sergey N. Shevchenko, and Franco Nori. "Nonadiabatic Landau–Zener–Stückelberg–Majorana transitions, dynamics, and interference." In: *Phys. Rep.* 995 (Jan. 2023), pp. 1–89. DOI: 10.1016/J.PHYSREP.2022.10.002 (cited on pages 12, 13).

[102] Hiroki. Nakamura. *Nonadiabatic transition : concepts, basic theories and applications.* World Scientific, 2002, p. 376 (cited on page 13).

[103] L. Landau. "Zur Theorie der Energieubertragung. II." In: *Phys. Z. Sowjetunion* 2 (1932), pp. 46–51 (cited on page 13).

[104] Clarence Zener. "Non-adiabatic crossing of energy levels." In: *Proc. R. Soc. A* 137.833 (Sept. 1932), pp. 696–702. DOI: 10.1098/RSPA.1932.0165 (cited on page 13).

[105] Ettore Majorana. "Atomi orientati in campo magnetico variabile." In: *Il Nuovo Cimento* 9.2 (Feb. 1932), pp. 43–50. DOI: 10.1007/BF02960953 (cited on page 13).

[106] E. C. G. Stueckelberg. "Theorie der unelastischen Stösse zwischen Atomen." In: *Helv. Phys. Acta* 5 (1932), p. 369. DOI: 10.5169/seals-110177 (cited on page 13).

[107] Sergey N. Shevchenko, S. Ashhab, and Franco Nori. "Landau-Zener-Stückelberg interferometry." In: *Phys. Rep.* 492.1 (2010), pp. 1–30. DOI: 10.1016/j.physrep.2010.03.002 (cited on page 13).

[108] M. Kira and S. W. Koch. "Cluster-expansion representation in quantum optics." In: *Phys. Rev. A* 78.2 (Aug. 2008), p. 022102. DOI: 10.1103/PHYSREVA.78.022102 (cited on page 15).

[109] Jens Fricke. "Transport Equations Including Many-Particle Correlations for an Arbitrary Quantum System: A General Formalism." In: *Ann. Phys.* 252.2 (Dec. 1996), pp. 479–498. DOI: 10.1006/APHY.1996.0142 (cited on page 15).

[110] N W Ashcroft and N D Mermin. *Solid State Physics*. Cengage Learning, 2011 (cited on page 15).

[111] W. V. Houston. "Acceleration of Electrons in a Crystal Lattice." In: *Phys. Rev.* 57.3 (Feb. 1940), p. 184. DOI: 10.1103/PhysRev.57.184 (cited on page 16).

[112] J B Krieger and G J Iafrate. "Quantum transport for Bloch electrons in a spatially homogeneous electric field." In: *Phys. Rev. B* 35.18 (Feb. 1987), p. 9644. DOI: 10.1103/PhysRevB.35.9644 (cited on page 16).

[113] E I Blount. "Formalisms of Band Theory." In: *Solid State Phys.* 13.C (Feb. 1962), pp. 305–373. DOI: 10.1016/S0081-1947(08)60459-2 (cited on page 17).

[114] Tran Trung Luu and Hans Jakob Wörner. "High-order harmonic generation in solids: A unifying approach." In: *Phys. Rev. B* 94.11 (Sept. 2016), p. 115164. DOI: 10.1103/PHYSREVB.94.115164 (cited on page 17).

[115] Chao Yu et al. "Dependence of high-order-harmonic generation on dipole moment in Si O2 crystals." In: *Phys. Rev. A* 94.1 (July 2016), p. 013846. DOI: 10.1103/PhysRevA.94.013846 (cited on page 17).

[116] Shicheng Jiang et al. “Role of the Transition Dipole Amplitude and Phase on the Generation of Odd and even High-Order Harmonics in Crystals.” In: *Phys. Rev. Lett.* 120.25 (June 2018), p. 253201. DOI: 10.1103/PHYSREVLETT.120.253201 (cited on page 17).

[117] Isak Kilen et al. “Propagation Induced Dephasing in Semiconductor High-Harmonic Generation.” In: *Phys. Rev. Lett.* 125.8 (Aug. 2020), p. 083901. DOI: 10.1103/PhysRevLett.125.083901 (cited on page 18).

[118] Viacheslav Korolev et al. “Unveiling the Role of Electron-Phonon Scattering in Dephasing High-Order Harmonics in Solids.” In: (Jan. 2024) (cited on page 18).

[119] Graham G. Brown et al. “A Real-Space Perspective on Dephasing in Solid-State High Harmonic Generation.” In: *Phys. Rev. Res.* 6.4 (Oct. 2022). DOI: 10.1103/PhysRevResearch.6.043005 (cited on page 18).

[120] Graham G. Brown et al. “Ultrafast dephasing in solid state high harmonic generation: macroscopic origin revealed by real-space dynamics.” In: *J. Opt. Am. B* 41.6 (Oct. 2023), B40. DOI: 10.1364/josab.513543 (cited on page 18).

[121] Claudio Aversa and J. E. Sipe. “Nonlinear optical susceptibilities of semiconductors: Results with a length-gauge analysis.” In: *Phys. Rev. B* 52.20 (Nov. 1995), p. 14636. DOI: 10.1103/PhysRevB.52.14636 (cited on pages 20, 25).

[122] Yong Sing You et al. “High-harmonic generation in amorphous solids.” In: *Nat. Commun.* 8.1 (Sept. 2017), pp. 1–5. DOI: 10.1038/s41467-017-00989-4 (cited on page 20).

[123] Naotaka Yoshikawa et al. “Interband resonant high-harmonic generation by valley polarized electron–hole pairs.” In: *Nat. Commun.* 10.1 (Aug. 2019), pp. 1–7. DOI: 10.1038/s41467-019-11697-6 (cited on page 20).

[124] John David Jackson. *Classical Electrodynamics*. 2nd ed. Wiley, 1975 (cited on page 20).

[125] Mark H. Holmes. *Introduction to the Foundations of Applied Mathematics*. Vol. 56. Texts in Applied Mathematics. Springer Cham, 2019 (cited on pages 21, 58).

[126] A H Castro Neto et al. “The electronic properties of graphene.” In: *Rev. Mod. Phys.* 81.1 (Jan. 2009), pp. 109–162. DOI: 10.1103/revmodphys.81.109 (cited on page 23).

[127] Chao Xing Liu et al. “Model Hamiltonian for topological insulators.” In: *Phys. Rev. B* 82.4 (July 2010), p. 045122. DOI: 10.1103/PHYSREVB.82.045122 (cited on pages 23, 42, 72).

[128] J. E. Sipe and Ed Ghahramani. “Nonlinear optical response of semiconductors in the independent-particle approximation.” In: *Phys. Rev. B* 48.16 (Oct. 1993), p. 11705. DOI: 10.1103/PhysRevB.48.11705 (cited on page 25).

[129] Claudio Aversa et al. “Third-order optical nonlinearities in semiconductors: The two-band model.” In: *Phys. Rev. B* 50.24 (Dec. 1994), p. 18073. DOI: 10.1103/PhysRevB.50.18073 (cited on page 25).

[130] J. Sipe and A. Shkrebtii. “Second-order optical response in semiconductors.” In: *Phys. Rev. B* 61.8 (Feb. 2000), p. 5337. DOI: 10.1103/PhysRevB.61.5337 (cited on page 25).

[131] W. R. Hannes and T. Meier. “Higher-order contributions and nonperturbative effects in the nondegenerate nonlinear optical absorption of semiconductors using a two-band model.” In: *Phys. Rev. B* 99.12 (Mar. 2019), p. 125301. DOI: 10.1103/PHYSREVB.99.125301/DELIVERABLE/C78660B5-8113-453F-BB82-427618A44968 (cited on page 25).

[132] Paul Herrmann et al. “Nonlinear valley selection rules and all-optical probe of broken time-reversal symmetry in monolayer WSe2.” In: *Nat. Photonics* 19.3 (Jan. 2025), pp. 300–306. DOI: 10.1038/s41566-024-01591-z (cited on page 25).

[133] Florentine Friedrich et al. “Measurement of optically induced broken time-reversal symmetry in atomically thin crystals.” In: *Nat. Photonics* (Nov. 2025), pp. 1–8. DOI: 10.1038/s41566-025-01801-2 (cited on page 25).

[134] J. Itatani et al. “Tomographic imaging of molecular orbitals.” In: *Nature* 432.7019 (Dec. 2004), pp. 867–871. DOI: 10.1038/nature03183 (cited on page 25).

[135] Michele Goano et al. “Electronic structure of wurtzite ZnO: Nonlocal pseudopotential and ab initio calculations.” In: *J. Appl. Phys.* 102.8 (Oct. 2007). DOI: 10.1063/1.2794380/375497 (cited on pages 29, 89).

[136] Jiahao You et al. “Quantum-trajectory-based analysis of far-field spatial profiles in high-order harmonic generation from single-layer ZnO.” In: *Opt. Express* 33.18 (Sept. 2025), pp. 38841–38856. DOI: 10.1364/OE.573658 (cited on pages 29, 89).

[137] G. Vampa and T. Brabec. "Merge of high harmonic generation from gases and solids and its implications for attosecond science." In: *J. Phys. B* 50.8 (Mar. 2017), p. 083001. DOI: 10.1088/1361-6455/AA528D (cited on pages 29, 89).

[138] Xiao Zhang et al. "Ellipticity dependence transition induced by dynamical Bloch oscillations." In: *Phys. Rev. B* 99.1 (Feb. 2019), p. 14304. DOI: 10.1103/PhysRevB.99.014304 (cited on pages 29, 89).

[139] Jon P. Davis and Philip Pechukas. "Nonadiabatic transitions induced by a time-dependent Hamiltonian in the semiclassical/adiabatic limit: The two-state case." In: *J. Chem. Phys.* 64.8 (Apr. 1976), pp. 3129–3137. DOI: 10.1063/1.432648 (cited on page 31).

[140] Hidetoshi Taya, Masaru Hongo, and Tatsuhiko N. Ikeda. "Analytical WKB theory for high-harmonic generation and its application to massive Dirac electrons." In: *Phys. Rev. B* 104.14 (Oct. 2021), p. L140305. DOI: 10.1103/PHYSREVB.104.L140305 (cited on pages 31, 42).

[141] M. V. Berry and K. E. Mount. "Semiclassical approximations in wave mechanics." In: *Rep. Prog. Phys.* 35.1 (Jan. 1972), p. 315. DOI: 10.1088/0034-4885/35/1/306 (cited on page 32).

[142] M. V. Berry. "Waves and Thom's theorem." In: *Adv. Phys.* 25.1 (1976), pp. 1–26. DOI: 10.1080/00018737600101342 (cited on page 32).

[143] J. N.L. Connor. "Catastrophes and molecular collisions." In: *Mol. Phys.* 31.1 (1976), pp. 33–55. DOI: 10.1080/00268977600100041 (cited on page 32).

[144] M. S.. Child. *Semiclassical mechanics with molecular applications.* Clarendon Press, 2023, p. 417 (cited on page 32).

[145] Umberto De Giovannini and Hannes Hübener. "Floquet analysis of excitations in materials." In: *J. Phys. Mater.* 3.1 (Oct. 2019), p. 12001. DOI: 10.1088/2515-7639/ab387b (cited on pages 34, 35, 81).

[146] J K Freericks, H R Krishnamurthy, and Th. Pruschke. "Theoretical Description of Time-Resolved Photoemission Spectroscopy: Application to Pump-Probe Experiments." In: *Phys. Rev. Lett.* 102.13 (Mar. 2009), p. 136401. DOI: 10.1103/physrevlett.102.136401 (cited on pages 35, 81).

[147] Michael Sentef et al. “Examining Electron-Boson Coupling Using Time-Resolved Spectroscopy.” In: *Phys. Rev. X* 3.4 (Dec. 2013), p. 41033. DOI: 10.1103/physrevx.3.041033 (cited on page 35).

[148] Michael Schüler and Michael A Sentef. “Theory of subcycle time-resolved photoemission: Application to terahertz photodressing in graphene.” In: *J. Electron Spectros. Relat. Phenomena* 253 (Dec. 2021), p. 147121. DOI: 10.1016/j.elspec.2021.147121 (cited on page 35).

[149] B. Moritz, T. P. Devereaux, and J. K. Freericks. “Time-resolved photoemission of correlated electrons driven out of equilibrium.” In: *Phys. Rev. B* 81.16 (Apr. 2010), p. 165112. DOI: 10.1103/PhysRevB.81.165112 (cited on page 35).

[150] R. Bertoni et al. “Generation and Evolution of Spin-, Valley-, and Layer-Polarized Excited Carriers in Inversion-Symmetric WSe_2.” In: *Phys. Rev. Lett.* 117.27 (Dec. 2016), p. 277201. DOI: 10.1103/PhysRevLett.117.277201 (cited on page 35).

[151] Hannes Hübener et al. “Creating stable Floquet–Weyl semimetals by laser-driving of 3D Dirac materials.” In: *Nat. Commun.* 8.1 (Jan. 2017), pp. 13940–. DOI: 10.1038/ncomms13940 (cited on page 35).

[152] H P Breuer and M Holthaus. “Adiabatic processes in the ionization of highly excited hydrogen atoms.” In: *Z. Phys. D* 11.1 (Mar. 1989), pp. 1–14. DOI: 10.1007/bf01436579 (cited on page 35).

[153] H P Breuer and M Holthaus. “Quantum phases and Landau-Zener transitions in oscillating fields.” In: *Phys. Lett. A* 140.9 (Oct. 1989), pp. 507–512. DOI: 10.1016/0375-9601(89)90132-1 (cited on page 35).

[154] Stéphane Guérin. “Complete dissociation by chirped laser pulses designed by adiabatic Floquet analysis.” In: *Phys. Rev. A* 56.2 (Aug. 1997), p. 1458. DOI: 10.1103/PhysRevA.56.1458 (cited on page 35).

[155] Kento Uchida et al. “Diabatic and adiabatic transitions between Floquet states imprinted in coherent exciton emission in monolayer WSe2.” In: *Sci. Adv.* 8.51 (Dec. 2022). DOI: 10.1126/sciadv.abq728 (cited on page 35).

[156] R. Lefebvre et al. “Resonance Coalescence in Molecular Photodissociation.” In: *Phys. Rev. Lett.* 103.12 (Sept. 2009), p. 123003. DOI: 10.1103/PhysRevLett.103.123003 (cited on page 35).

[157] Arnaud Leclerc et al. "Controlling vibrational cooling with zero-width resonances: An adiabatic Floquet approach." In: *Phys. Rev. A* 94.4 (Oct. 2016), p. 043409. DOI: 10.1103/PhysRevA.94.043409 (cited on page 35).

[158] Arnaud Leclerc et al. "Exotic states in the strong-field control of H_2^+ dissociation dynamics: from exceptional points to zero-width resonances." In: *J. Phys. B* 50.23 (Nov. 2017), p. 234002. DOI: 10.1088/1361-6455/AA8CA1 (cited on page 35).

[159] Alexander Altland and Ben D Simons. *Condensed Matter Field Theory*. Cambridge University Press (cited on page 42).

[160] Ya Bai et al. "High-harmonic generation from topological surface states." In: *Nat. Phys.* 17.3 (Nov. 2020), pp. 311–315. DOI: 10.1038/s41567-020-01052-8 (cited on page 42).

[161] Stanislav Yu Kruchinin, Ferenc Krausz, and Vladislav S Yakovlev. "Colloquium: Strong-field phenomena in periodic systems." In: *Rev. Mod. Phys.* 90.2 (Feb. 2018), p. 21002. DOI: 10.1103/REVMODPHYS.90.021002 (cited on page 42).

[162] L V Keldysh. "Ionization in the Field of a Strong Electromagnetic Wave." In: *J. Exp. Theor. Phys.* 20.5 (1965), pp. 1307–1314 (cited on page 42).

[163] Edward McCann and Mikito Koshino. "The electronic properties of bilayer graphene." In: *Rep. Prog. Phys.* 76.5 (Feb. 2013), p. 56503. DOI: 10.1088/0034-4885/76/5/056503 (cited on page 43).

[164] Edward McCann and Vladimir I. Fal'ko. "Landau-level degeneracy and quantum hall effect in a graphite bilayer." In: *Phys. Rev. Lett.* 96.8 (Mar. 2006), p. 086805. DOI: 10.1103/PHYSREVLETT.96.086805 (cited on page 43).

[165] Liang Fu. "Hexagonal Warping Effects in the Surface States of the Topological Insulator Bi_2Te_3." In: *Phys. Rev. Lett.* 103.26 (Dec. 2009), p. 266801. DOI: 10.1103/physrevlett.103.266801 (cited on page 72).

[166] Wen-Yu Shan, Hai-Zhou Lu, and Shun-Qing Shen. "Effective continuous model for surface states and thin films of three-dimensional topological insulators." In: *New J. Phys.* 12.4 (Apr. 2010), p. 43048. DOI: 10.1088/1367-2630/12/4/043048 (cited on page 72).

[167] Thomas J. Whitcher et al. “Correlated plasmons in the topological insulator Bi2Se3 induced by long-range electron correlations.” In: *NPG Asia Materials* 12.1 (May 2020), pp. 37–. DOI: 10.1038/s41427-020-0218-7 (cited on pages 72, 75, 81).

[168] Jerryman A. Gyamfi. “Fundamentals of quantum mechanics in Liouville space.” In: *Eur. J. Phys.* 41.6 (Oct. 2020), p. 063002. DOI: 10.1088/1361-6404/AB9FDD (cited on page 75).

[169] Sang Tae Park. “Interference in Floquet-Volkov transitions.” In: *Phys. Rev. A* 90.1 (July 2014), p. 13420. DOI: 10.1103/physreva.90.013420 (cited on page 81).

[170] Wolfgang Hogger. *howbgl/Damysos.jl: v1.1.0*. Version v1.1.0. Jan. 2026. DOI: 10.5281/zenodo.18414810 (cited on pages 95, 97, 101).

[171] Christopher Rackauckas and Qing Nie. “DifferentialEquations.jl – A Performant and Feature-Rich Ecosystem for Solving Differential Equations in Julia.” In: *Journal of Open Research Software* 5.1 (Feb. 2017), p. 15. DOI: 10.5334/JORS.151 (cited on page 96).

[172] Utkarsh Utkarsh et al. “Automated translation and accelerated solving of differential equations on multiple GPU platforms.” In: *Computer Methods in Applied Mechanics and Engineering* 419 (Feb. 2024), p. 116591. DOI: 10.1016/J.CMA.2023.116591 (cited on page 96).

[173] Lewis Fry Richardson. “IX. The approximate arithmetical solution by finite differences of physical problems involving differential equations, with an application to the stresses in a masonry dam.” In: *Philosophical Transactions of the Royal Society of London, Series A: Containing Papers of a Mathematical or Physical Character* 210.459-470 (Jan. 1911), pp. 307–357. DOI: 10.1098/RSTA.1911.0009 (cited on page 98).

[174] David Goldberg. “What every computer scientist should know about floating-point arithmetic.” In: *ACM Computing Surveys* 23.1 (Mar. 1991), pp. 5–48. DOI: 10.1145/103162.103163 (cited on page 99).

[175] W. Kahan. “Pracniques: further remarks on reducing truncation errors.” In: *Communications of the ACM* 8.1 (Jan. 1965), p. 40. DOI: 10.1145/363707.363723 (cited on page 99).

[176] Wolfgang Hogger. *Data and code for: Coherent suppression of high harmonics and Floquet-Bloch sidebands in lightwave-driven Dirac systems*. Zenodo, 2026. DOI: 10.5281/zenodo.21065565 (cited on page 101).

Acknowledgments

The work was funded by the Deutsche Forschungsgemeinschaft (DFG, German Research Foundation) within Project-ID 314695032–SFB 1277 and Project-ID 502572516-GRK 2905. I acknowledge further support from the Regensburg Center for Ultrafast Nanoscopy (RUN). The author gratefully acknowledges the scientific support and HPC resources provided by the Erlangen National High Performance Computing Center (NHR@FAU) of the Friedrich-Alexander-Universität Erlangen-Nürnberg (FAU) under the NHR project b228da. NHR funding is provided by federal and Bavarian state authorities. NHR@FAU hardware is partially funded by the German Research Founddation (DFG)–440719683.

My deepest gratitude goes to Juan-Diego Urbina for guiding me through the journey starting with a Master's thesis all the way through my PhD as an advisor and as a friend. I cannot imagine finishing this work without his contagious, unshakable enthusiasm and his continued support and guidance. The free coffee also helped.

I also want to thank Andrea Donarini for taking the time to carefully examine this PhD thesis.

My sincerest gratitude goes to Tilo Wettig and Jascha Repp for assessing this work as members of the PhD committee.

I want to thank Klaus Richter for his guidance and for giving me the opportunity to work in his research group. It is through his experience, his diverse expertise, his vast network, his excellent leadership, and his ability to generate an open atmosphere of scientific exchange that I could grow as much as I did in the last years—scientifically and personally.

I am very grateful for the excellent collaboration with Yuriko Baba. Her mere presence during her stay in Regensburg managed to lift up the spirits of our whole group, myself included. She also introduced me to the wonderful concept of Friday tasks—together with banana bread.

I also would like to thank Angelika Knothe for our collaboration, for her wonderful scientific guidance, her help in writing, for proof-reading large parts of this thesis, for her meticulous critique of colormaps, and for her inspiring motivation scientific and otherwise.

I also want to extend my gratitude towards Alexander Riedel for his essential contributions to our work, for proof-reading of this thesis, and for our great discussions about physics and all other things in life.

My deepest thanks go to Mathias Steinhuber for his personal support since our shared undergraduate studies, for his various ingenious projects for and at the expense of the Richter chair, and for building nice snowmen.

I would like to thank Torsten Weber for his excellent company in our shared office and for his motivated explanations of various obtuse mathematical concepts—despite my complete lack of understanding. Also for his wonderful trumpets, caps and pants.

I am very grateful to Doris Meier for her personal support also and especially in difficult times, for her invaluable work at the Richter chair, and for her incredible management of the SFB 1277.

I thank Adrian Seith and Jan Wilhelm for their expert insights into numerics of the SBE and for our inspiring discussions.

I thank Vanessa Junk for guiding me in the early stages of my research, for our collaboration, and for introducing me to many technical day-to-day aspects of condensed matter research.

I am also grateful to Cosimo Gorini for our collaboration, scientific discussions, and referee bashing.

I also want to extend my gratitude towards all of my colleagues and fellow group members for providing the best environment possible to conduct this research, Georg Maier, Fabian Haneder, Jakob Fuchs, Camilo Moreno-Jaimes, Michael Barth, Benjamin Geier, Quirin Hummel, Maximilian Graml, Johannes Dieplinger, Mario Ebner, Martin Steinau, Florian Schöppl, Lukas Behringer, Toni Siegmund, Romy Fischer, Maximilian Fürst, Jordi Picó-Cortés, Andreas Bereczuk, Sebastian Hörhold, Ming-Hao Liu, Gerrit Caspari and Raphael Kozlovsky.

I extend my deepest gratitude to Michael Hartung for somehow holding together the Linux support at the RZ.

This work would not have been possible without the support of my family. I want to thank my parents, Franziska and Rupert, and my siblings, Heidrun and Reinhardt, for their continued support throughout all of my studies and scientific endeavors.

Most importantly, I thank my girlfriend, Alexandra, for her unwavering patience, understanding and constant encouragement. Her support, humor, and ability to bring balance into my life were invaluable—especially during the more intense phases of this thesis.

Changes in the Published Version

This chapter documents the differences between the version of this thesis submitted for examination and the present published version. Throughout, text added in the published version is shown in blue and ~~text removed from the examined version is shown in red with strikethrough~~. Page and section references are given with respect to the published version. Purely typographical and minor grammatical corrections are not listed.

Page format and figures The published version uses A5 page format, whereas the examined version used A4. To preserve legibility at the smaller page size, every figure was regenerated with enlarged legend text and reduced gridline density; with the exception of the two figures discussed individually below, the underlying data and plotted content are unchanged. As this adjustment is uniform throughout the document, it is noted here once and not listed individually for each figure.

Chapter 2, section 2.2

Two passages of this section were reworked; the remainder of the section is unchanged in content (see the closing remark below). Because both passages were recast almost symbol-by-symbol, they are reproduced here in full as examined/published pairs rather than marked up inline. Text that is genuinely *new* in the published version (with no counterpart in the examined version) is shown in blue.

Eigenvalue problem for the lattice-periodic functions, p. 15 The eigenvalue equation for the periodic parts $u_{n\boldsymbol{k}}(\boldsymbol{r})$ was rewritten from abstract Dirac form into an explicit real-space differential operator, and the periodic boundary conditions and the underlying Hilbert-space (orthonormality) convention were added.

Examined version:

$$\hat{h}_0(\boldsymbol{k})\,|n\boldsymbol{k}\rangle = \varepsilon_n(\boldsymbol{k})\,|n\boldsymbol{k}\rangle \ , \tag{2.22}$$

with $\hat{h}_0(\boldsymbol{k}) = \mathrm{e}^{-\mathrm{i}\boldsymbol{k}\hat{\boldsymbol{r}}}\hat{\mathscr{H}}_0\mathrm{e}^{\mathrm{i}\boldsymbol{k}\hat{\boldsymbol{r}}}$.

Published version:

$$\hat{h}_0(\boldsymbol{k})\, u_{n\boldsymbol{k}}(\boldsymbol{r}) = \left[\frac{1}{2m}\left(-\mathrm{i}\nabla + \boldsymbol{k}\right)^2 + V(\boldsymbol{r})\right] u_{n\boldsymbol{k}}(\boldsymbol{r}) = \varepsilon_n(\boldsymbol{k})\, u_{n\boldsymbol{k}}(\boldsymbol{r}) \tag{2.22}$$

with boundary conditions $u_{n\boldsymbol{k}}(\boldsymbol{r}) = u_{n\boldsymbol{k}}(\boldsymbol{r} + \boldsymbol{R})$ and $\boldsymbol{k}$ being any wavevector in the first Brillouin zone. The kets $|n\boldsymbol{k}\rangle$ thus denote the periodic parts as elements of L^2 over the unit cell, with inner product $\langle m\boldsymbol{k}|n\boldsymbol{k}\rangle = \int_{\mathrm{u.c.}} \mathrm{d}^3r\; u^*_{m\boldsymbol{k}}(\boldsymbol{r})\, u_{n\boldsymbol{k}}(\boldsymbol{r}) = \delta_{mn}$.

Definition of the Houston basis, p. 16 The co-moving (Houston) states were recast in real space as $u^H_{n\boldsymbol{k}}(\boldsymbol{r}) = \langle \boldsymbol{r}|n\boldsymbol{k}_t\rangle$, the defining eigenvalue equation rewritten accordingly, and the kinematic crystal momentum $\boldsymbol{k}_t = \boldsymbol{k} - \boldsymbol{A}(t)$ moved from a standalone equation into the prose. As this removed a numbered display equation, every subsequent equation in the chapter is numbered one lower than in the examined version.

Examined version: A possible basis for representing the equations of motion are the co-moving (or Houston) states $|n\boldsymbol{k}_t\rangle$, which are the instantaneous eigenstates of $\hat{h}_0(\boldsymbol{k}_t)$,

$$\hat{h}_0(\boldsymbol{k}_t)\, |n\boldsymbol{k}_t\rangle = \varepsilon_n(\boldsymbol{k}_t)\, |n\boldsymbol{k}_t\rangle \tag{2.26}$$

with eigenenergies ε_n in terms of the kinematical momentum,

$$\boldsymbol{k}_t = \boldsymbol{k} - \boldsymbol{A}(t)\,. \tag{2.27}$$

Published version: A possible basis for representing the equations of motion are the co-moving (or Houston) states $u^H_{n\boldsymbol{k}}(\boldsymbol{r}) = \langle \boldsymbol{r}|n\boldsymbol{k}_t\rangle$, which are the Bloch states evaluated at the shifted (kinetic) crystal momentum $\boldsymbol{k}_t = \boldsymbol{k} - \boldsymbol{A}(t)$. The Houston states are therefore the instantaneous eigenstates of $\hat{h}_0(\boldsymbol{k}_t)$

$$\hat{h}_0(\boldsymbol{k}_t)\, u^H_{n\boldsymbol{k}}(\boldsymbol{r}) = \varepsilon_n(\boldsymbol{k}_t)\, u^H_{n\boldsymbol{k}}(\boldsymbol{r})\,. \tag{2.26}$$

Remainder of the section The intervening material (dipole approximation, choice of velocity gauge, minimal-coupling Hamiltonian, Liouville–von Neumann equation, the Houston-basis equations of motion, and the dipole matrix elements) is unchanged.

Chapter 4, section 4.2

Figure 4.1, p. 73. The contour map of the energy difference ϵ_{cv}/Ω_0 over the (κ_x, κ_y) plane was shown with incorrect orientation in the examined version. The figure has been regenerated with the correct orientation. No statement in the surrounding text relies on the orientation of the map; the discussion is unchanged.

Figure 4.1b, p. 73. The vertical axis of the band-energy slices ϵ_{cv}/Ω_0 was scaled incorrectly in the examined version, displaying a range of approximately 0 to 0.75 instead of the correct range of -1 to 5. The figure has been regenerated with the correct vertical scale; the underlying data are unchanged. The qualitative behaviour of the curves is unaffected, and no quantitative statement in the surrounding text draws on values read from this figure; the discussion is unchanged.

Definition of Liouvillian, p. 75 Another definition of $\hat{\mathscr{L}}(\boldsymbol{k}, t)$ was used in Equation 4.11 to facilitate easier understanding.

$$\frac{\partial}{\partial t}\varrho(\boldsymbol{k},t) = \hat{\mathscr{L}}(\boldsymbol{k},t)\,\varrho(\boldsymbol{k},t) = -\mathrm{i}[\![\hat{\mathscr{H}}(t), \hat{\mathbb{1}}]\!]\,\varrho(\boldsymbol{k},t)\,, \tag{4.11a}$$

$$[\![\hat{A}, \hat{B}]\!] = \hat{A}\otimes\hat{B} - \hat{B}\otimes\hat{A} \tag{4.11b, examined}$$

$$\hat{\mathscr{L}}(\boldsymbol{k},t) = -\mathrm{i}\big[\hat{\mathscr{H}}(\boldsymbol{k},t),\ \cdot\ \big] \tag{4.11b, published}$$

Acknowledgements

Added official funding statement The official funding statement was inserted at the beginning of the section.

The work was funded by the Deutsche Forschungsgemeinschaft (DFG, German Research Foundation) within Project-ID 314695032–SFB 1277 and Project-ID 502572516-GRK 2905. I acknowledge further support from the Regensburg Center for Ultrafast Nanoscopy (RUN). The author gratefully acknowledges the scientific support and HPC resources provided by the Erlangen National High Performance Computing Center (NHR@FAU) of the Friedrich-Alexander-Universität Erlangen-Nürnberg (FAU) under the

NHR project b228da. NHR funding is provided by federal and Bavarian state authorities. NHR@FAU hardware is partially funded by the German Research Founddation (DFG)–440719683.

My deepest gratitude goes to Juan-Diego Urbina for guiding me through the journey starting with a Master's thesis all the way through my PhD as an advisor and as a friend.

Removed unofficial funding statement The short sentence acknowledging financial support is omitted in the published version.

I extend my deepest gratitude to Michael Hartung for somehow holding together the Linux support at the RZ.

~~I thank the SFB 1277 for financial support and the NHR in Erlangen for compute power, especially the excellent support team.~~